ADDRESSING THE FUNDAMENTAL OBSTACLES OF P-TYPE DOPING, SUBSTRATES, AND DEFECT DENSITIES IN GROUP III-NITRIDES GROWN BY MOLECULAR BEAM EPITAXY: TOWARDS A III-NITRIDE ON SILICON SOLAR CELL

A Dissertation
Presented to
The Academic Faculty

by

Brendan P. Gunning

In Partial Fulfillment
Of the Requirements for the Degree
Doctor of Philosophy in Electrical and Computer Engineering

Georgia Institute of Technology
May 2016

ADDRESSING THE FUNDAMENTAL OBSTACLES OF P-TYPE DOPING, SUBSTRATES, AND DEFECT DENSITIES IN GROUP III-NITRIDES GROWN BY MOLECULAR BEAM EPITAXY: TOWARDS A III-NITRIDE ON SILICON SOLAR CELL

Approved by:

Dr. W. Alan Doolittle, Advisor
School of Electrical and Computer Engineering
Georgia Institute of Technology

Dr. P. Douglas Yoder
School of Electrical and Computer Engineering
Georgia Institute of Technology

Dr. Shyh-Chiang Shen
School of Electrical and Computer Engineering
Georgia Institute of Technology

Dr. A. Bruno Frazier
School of Electrical and Computer Engineering
Georgia Institute of Technology

Dr. Samuel Graham
School of Mechanical Engineering
Georgia Institute of Technology

Date Approved: 12/7/2015

ACKNOWLEDGEMENTS

First and foremost, I would like to thank all of my family for their unwavering support throughout my many years working towards this final achievement. My mother and father have challenged and pushed me from a young age, instilling in me a competitive nature which has helped motivate me throughout my academic career. They have been there for me through difficult times and victories. They are always eager to hear about my work, willing to listen to me vent my frustrations and ready to provide the kick I sometimes needed to keep focused. Without the love and support of my family, I would not have succeeded in my graduate studies, and for that I can never truly repay them.

My aunts, uncles, cousins, and grandparents, both at home in Baltimore and around Atlanta, have provided me with a refuge to keep myself grounded and recharged. Whether a home-cooked meal, or a place to stay for a holiday weekend, they have been a constant source of love and support over the years and I cannot thank them enough.

I owe my advisor, Prof. W. Alan Doolittle, more gratitude than I can possibly convey. He has provided me with this amazing opportunity while showing seemingly endless patience and understanding in order to help me reach this point. He is an incredible teacher and mentor, and I am truly lucky to have him as my advisor and friend.

I would also like to thank many current and former members of Prof. Doolittle's research group: Dr. Michael Moseley, Chloe Fabien, Joseph Merola, Evan Clinton, Joshua Shank, Brooks Tellekamp, Jonathan Lowder, Dr. Jordan Greenlee, Dr. Daniel Billingsley, and Laws Calley.

I would like to thank my thesis committee: Dr. Douglas Yoder, Dr. Shyh-Chiang Shen, Dr. Bruno Frazier, and Dr. Samuel Graham for their advice and consideration throughout this process. Finally, I would like to thank the IEN staff for all their help with cleanroom equipment, training, and maintenance: Walter Henderson, Dean Sutter, Charlie Suh, Eric Woods, Scott Fowler, and Gary Spinner.

TABLE OF CONTENTS

LIST OF TABLES

LIST OF FIGURES

LIST OF NOMENCLATURE

Å	Angstrom (10^{-10} meter)
λ	wavelength
λ_{mfp}	mean-free path
ρ	resistivity
σ	conductivity
Ω	Ohm
μ	carrier mobility
μm	micron (10^{-6} meter)
2DEG	two-dimensional electron gas
2DHG	two-dimensional hole gas
a	a lattice constant
AFM	atomic-force microscopy
Al	aluminum
AlGaN	aluminum gallium nitride
AlN	aluminum nitride
B	b lattice constant
C-V	capacitance-voltage
c	c lattice constant
C_{xy}	elastic coefficient
DI	deionized
E_g	bandgap energy
eV	electron volt
EDX	energy dispersive x-ray spectroscopy
FWHM	full width at half maximum
Ga	gallium
GaAs	gallium arsenide
GaN	gallium nitride
Ge	germanium
H_2SO_4	sulfuric acid
H_2O_2	hydrogen peroxide

HCl	hydrochloric acid
HEMT	high electron mobility transistor
HF	hydrofluoric acid
I_{SC}	short-circuit current
I-V	current-voltage
In	indium
InGaN	indium gallium nitride
InN	indium nitride
J_{SC}	short-circuit current density
K	Kelvin
KOH	potassium hydroxide
LD	laser diode
LED	light-emitting diode
MBE	molecular-beam epitaxy
Mg	magnesium
MOCVD	metal-organic chemical vapor deposition
MOMBE	metal-organic molecular beam epitaxy
MOVPE	metal-organic vapor phase epitaxy
N_2	nitrogen
NH_3	ammonia
NH_4OH	ammonium hydroxide
PL	photoluminescence
$Q_{x,y}$	x-ray diffraction scattering vectors
RC	x-ray diffraction rocking curve
RF	radio frequency
RGA	residual-gas analyzer
RHEED	reflection high-energy electron diffraction
RMS	root-mean-square
RSM	reciprocal space map
sccm	standard cubic centimeters per minute
SEM	scanning electron microscope
Si	silicon
SiC	silicon carbide
SIMS	secondary-ion mass spectrometry
T_{sub}	substrate (growth) temperature

UHV	ultra-high vacuum
UV	ultraviolet
V_{OC}	open-circuit voltage
W	Watts
XRD	x-ray diffraction

SUMMARY

In an era of ever-increasing demand for cheap energy, solar photovoltaics (PV) remains one of the strongest candidates for long-term renewable energy production. While solar currently represents a small percentage of global energy generation, the drive for sustainable energy predicts large short- and long-term growth in PV capacity. In order to meet this demand for inexpensive solar energy, advances must be made in cell cost and/or efficiency. III-nitride semiconductors provide a number of properties ideal for PV applications, but several major issues remain in this material system such that high efficiency solar cells have not yet been realized. This thesis examines the viability of a hybrid III-nitride-on-silicon solar cell by addressing some of the fundamental hurdles present in III-nitride growth and epitaxy.

In this work, p-type doping of III-nitrides is explored in order to better understand the shortcomings of existing p-type material and achieve higher hole concentrations. Using a modified form of molecular beam epitaxy (MBE) called metal-modulated epitaxy (MME), hole concentrations as high as 7.9×10^{19} cm^{-3} are achieved, nearly 20-40x the previous state of the art. Distinctions are drawn between traditional lighter-doped material and these heavily-doped MME-grown p-type films. Activation energies as low as 43 meV (compared to ~160 meV for conventional films) and acceptor activation efficiencies as high as 52% (compared to ~1-5% for conventional films) are reported, for which carrier freeze-out is dramatically reduced compared to lighter-doped films. Impurity band conduction, resulting from proper incorporation of Mg at concentrations

$>10^{20}$ cm^{-3} by careful selection and monitoring of growth conditions, is suggested as the source of these unique properties and more than 10x improvement in hole concentrations over previous state-of-the-art. Electrical properties and Mg incorporation were found to be sensitive to growth conditions and an optimal growth window is elucidated. Photoluminescence in highly p-type GaN and AlGaN further supports the presence of an acceptor band, and structural characterization demonstrates favorable Mg incorporation resulting in no Mg precipitation or inversion domains, confirming the optimal growth conditions. Diode devices using these highly p-type layers were found to be properly rectifying with turn-on voltages near 3 V, exhibiting room-temperature and cryogenic luminescence, and unambiguously confirming the p-type nature of the films.

High MBE growth rates in GaN are demonstrated using a modified high-conductance nitrogen plasma source. Growth rates from 1.6 μm/hour up to 8.4 μm/hour are achieved for pure nitrogen gas. A mixed argon/nitrogen plasma chemistry expands the range of achievable growth rates from ~1 μm/hour up to 9.8 μm/hour due to reduced ion content and more efficient generation of reactive atomic nitrogen species compared to a pure nitrogen plasma. Repeatable background electron concentrations of 1-2x10^{15} cm^{-3} are reported, and germanium is demonstrated as an alternative n-type dopant for high growth rate applications with electron concentrations from 2x10^{16} cm^{-3} up to 4x10^{19} cm^{-3}.

GaN growth on Si is explored using several unique nucleation methods in order to achieve a fully vertical device structure. *In situ* characterization during growth using a Ga droplet-based nucleation demonstrates rough surfaces with some polycrystalline character. Preliminary photovoltaic response with J_{SC} up to 58 mA/cm^2 and V_{OC} of 0.3 V are demonstrated, in spite of the poor crystal quality of the GaN films. Further study of

various diode configurations exhibit either conductive or rectifying junctions, and one device GaN/Si heterostructure shows a reverse bias breakdown voltage of ~170 V for a 4x4 mm^2 device. Alternative nucleation techniques exploiting the Al-Si eutectic demonstrate improved crystal quality and surface roughness, providing a path forward for improved PV devices.

Finally, an exotic substrate called alexandrite ($BeAl_2O_4$) is examined for GaN growth to attempt to exploit a unique relaxation mechanism and reduce dislocation densities. Growth on alexandrite demonstrates very smooth surfaces with root mean square roughness below 1 nm. Several nucleation and buffer layers demonstrate some improvements in crystal quality, but on the whole crystal quality remains poor in all cases compared to existing GaN growth on sapphire. Nonetheless, a diode structure is grown in spite of the defective films, which demonstrates proper rectifying behavior with ~3 V turn-on.

CHAPTER 1: INTRODUCTION

Group III-nitride semiconductors possess a number of properties which make them viable for a broad range of electronic and optoelectronic devices. These properties include a tunable, direct bandgap of 0.7 to 6.1 eV, high drift velocity, high mobility, and strong light absorption.[1-3] Together these attributes make III-nitrides well-suited for light-emitting diodes (LEDs), high electron mobility transistors (HEMTs), and potentially solar cells and heterojunction bipolar transistors (HBTs).[4, 5] For these reasons, III-nitrides have seen enormous growth over the past decade, primarily in the lighting industry where nitride-based blue LEDs combined with a yellow phosphor result in the now-ubiquitous white LED.[6, 7]

1.1 III-Nitride Properties

The III-nitride compound semiconductor material system can present both the cubic zinc-blende and the hexagonal wurtzite crystal structures. Of these, the wurtzite phase, shown in Figure 1.1, is the most thermodynamically stable and the most commonly reported.[8]

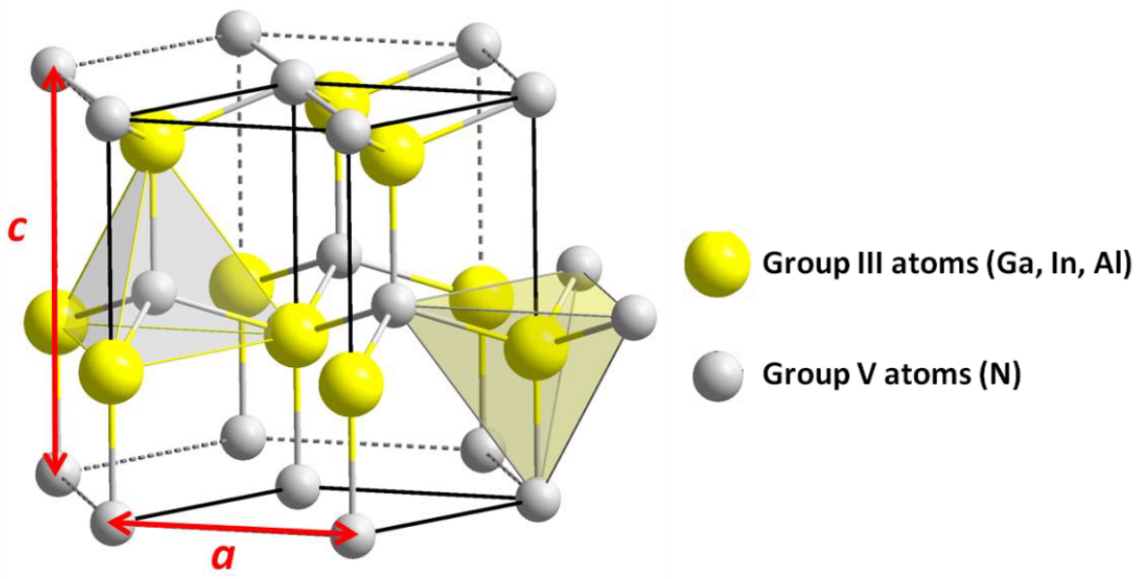

Figure 1.1: Group III-nitride wurtzite unit cell. [9]

The corresponding *a* and *c* lattice parameters are shown below in Table 1.1 for all three binary wurtzite III-nitride compounds.[10] AlN exhibits the smallest lattice spacing of the wurtzite III-nitrides, and has correspondingly high bandgap energy of 6.2 eV due to the high bond strength. For InN, the opposite is true with its large lattice spacing and small bandgap energy of 0.65 eV, while GaN falls in the middle at 3.4 eV. This trend is shown in the plot of bandgap energy and corresponding wavelength vs. *a* lattice parameter for the wurtzite III-nitride system in Figure 1.2.

Table 1.1: *a* and *c* lattice parameters for binary wurtzite III-nitride compounds.[10]

Material	*a* lattice constant (Å)	*c* lattice constant (Å)
AlN	3.112	4.978
GaN	3.189	5.185
InN	3.537	5.703

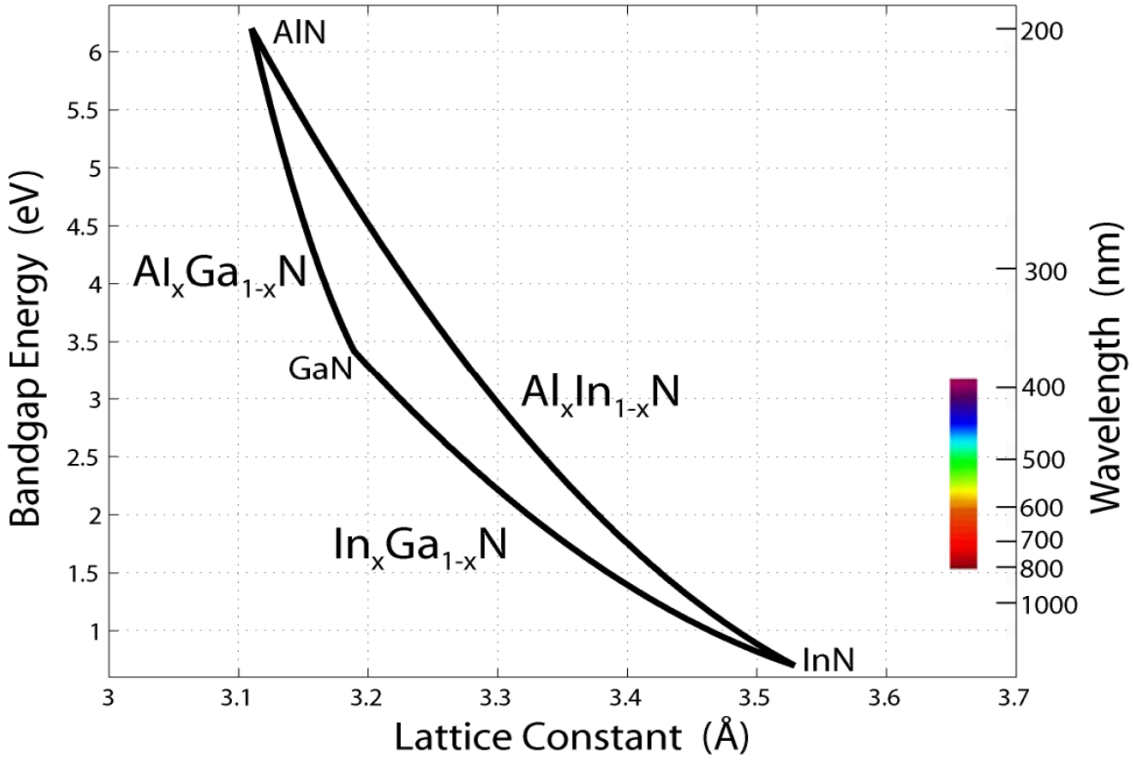

Figure 1.2: Energy bandgap vs. *a* lattice constant for the entire binary and ternary wurtzite III-nitride system. [11]

The broad range of possible energy bandgaps in the III-nitride system spans the entire visible spectrum and extends into both the ultraviolet and infrared wavelengths. This range of bandgaps can be achieved by alloying among the III-nitride binaries to form a ternary material (InGaN, AlGaN, InAlN) or even a quaternary material (InAlGaN). The bandgap energy of a ternary alloy can be calculated from Vegard's law:

$$E_g(A_{1-x}B_x) = (1-x)E_g(A) + (x)E_g(B) - (x)(1-x)C \tag{1.1}$$

where $E_g(A_{1-x}B_x)$ refers to the calculated bandgap of the ternary alloy, $E_g(A)$ is the

bandgap of one binary, $E_g(B)$ is the bandgap of the second binary, x is the mole fraction of the second alloy, and C is the bowing parameter for that particular ternary alloy system. The bowing parameter C is an experimentally determined value describing the nonlinearity of the composition-dependent bandgap energy.

The lack of inversion symmetry in the III-nitride wurtzite crystal structure, combined with the highly ionic metal-nitrogen bond, results in a spontaneous polarization in the material.[12] This can result in so-called Ga-polar or N-polar material depending on the direction of the spontaneous polarization field relative to the surface. The III-nitride system is also strongly piezoelectric, wherein strain energy induces polarization. [12] This is particularly critical since strain due to lattice-mismatched epitaxy is common in III-nitride heterostructures, which can result in drastic changes to band structures. Together, these polarization fields can have profound effects on device performance in either positive ways, such as for HEMTs, or negative ways where the polarization can induce an undesired potential barrier as is the case for solar cells.[13] In the specific case of the III-nitride LED, the polarization induces an enormous electric field inside the strained InGaN quantum well. As shown in Figure 1.3, this electric field causes injected electrons to accumulate at one side of the well while injected holes accumulate at the other. The separation of charge and band bending causes a shift of the emission wavelength, known as the quantum-confined Stark effect, and reduces the overlap of the two carriers' wave functions, hindering radiative recombination.[14, 15] This is just one example of the effects of polarization which clearly illustrates why polarization must be considered carefully during device design.

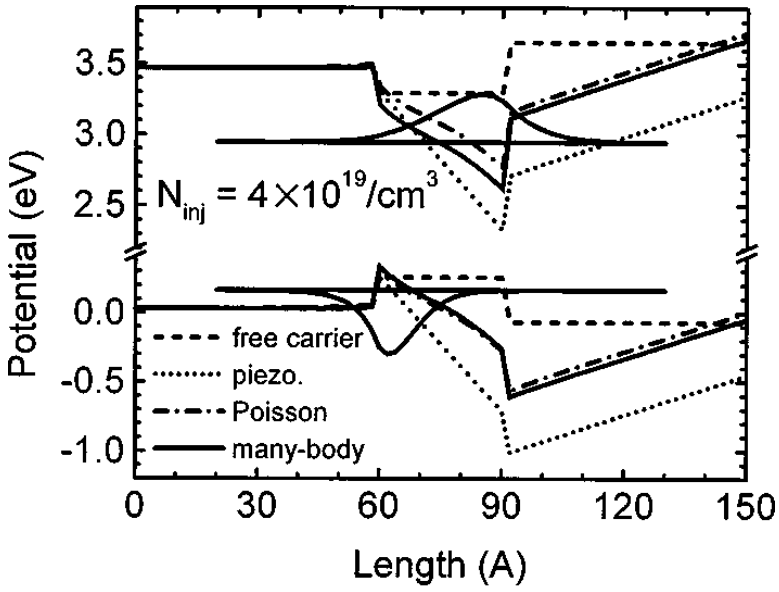

Figure 1.3: Energy band diagram for a InGaN/GaN single quantum well illustrating the quantum-confined Stark effect resulting in a separation of the electron and hole wave functions.

1.2 Molecular Beam Epitaxy

Molecular beam epitaxy (MBE) is a technique for the epitaxial growth of various crystalline materials, from semiconductors to metals to insulators. Epitaxy refers to the layer-by-layer growth of a crystalline material on a crystalline substrate. The "molecular beam" in this case refers to the transport of source material along a straight line to the substrate where several sources can react to form the crystalline film. The sources travel in a straight line due to the ultra-high vacuum (UHV) nature of MBE growth with operating pressures from 10^{-11} Torr up to 10^{-5} Torr depending on the specific application. The high vacuum environment results in a long mean-free path for the sources, as shown by the equation

$$\lambda_{mfp} = \frac{k_B T}{\pi d^2 P} \tag{1.2}$$

where λ_{mfp} is the mean-free path of a particle traveling in the system, k_B is Boltzmann's constant, T is temperature, d is the molecular diameter, and P is pressure. For a clean system with a pressure of 10^{-10} Torr at room temperature, the resulting mean-free path is on the order of >700 kilometers. For a pressure of 10^{-5} Torr which is typical during III-nitride MBE growth, the mean-free path falls to around 0.75 meters which is still ~5x larger than the distance between the crucible and the substrate. That means that an atom coming out of a crucible during growth will, on average, reach the substrate itself before coming into contact with any other atoms in the chamber. Thus, the source materials travel in a straight line, or "beam", until they hit the substrate. A basic illustration of an MBE system is shown in Figure 1.4.[16]

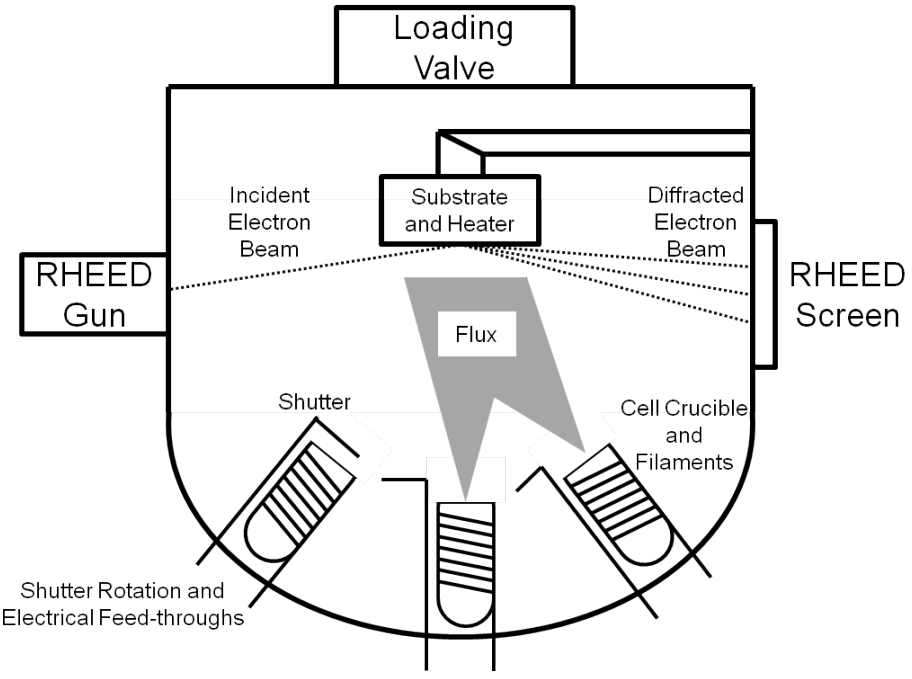

Figure 1.4: Top-down view of a simple MBE system.[16]

In Figure 1.4, the key components of a traditional MBE system can be seen. Solid

source materials (e.g. Ga, In, Al, etc.) are evaporated from effusion cells, where a crucible is surrounded by a heater filament and then by a refractory metal heat shield. The crucible materials vary, but typically are made of ceramic materials (i.e. pyrolytic boron nitride, graphite, aluminum oxide, beryllium oxide, etc.) or refractory metals (tungsten, tantalum, etc.) in order to withstand the high temperatures required to evaporate the source materials. Current is run through the filament, causing resistive heating of the crucible and the source material inside, which in turns increases the vapor pressure of the source material. This vapor pressure creates a flux of material exiting the end of the crucible towards the substrate, which can be controlled by changing the amount of heat applied by the filament. A thermocouple in the hot zone measures the temperature and can be used in a closed loop system to control temperature and, therefore, flux. Physical shutters, typically refractory metal disks at the end of the effusion cell, are often used to rapidly modulate the flux allowed to the substrate. The substrate itself is also heated using a resistive filament, with substrate temperatures ranging from less than 200°C for some epitaxial metals, up to more than 1000°C for some high temperature aluminum nitride growth. A thermocouple again measures the temperature of the substrate for feedback.

In the case of some specific source materials (i.e. P, As, Sb, NH_3, N_2, etc.) specialized equipment is required. For certain group V elements like phosphorus, arsenic, and antimony where significant overpressures are used and material depletion concerns arise, a valved effusion cell called a cracker is often employed. In a cracker, two independent filaments are operated at different temperatures. The large reservoir at the base, also called the bulk zone, is held at a moderate temperature to evaporate the

source material. However, the source material may be less reactive due to the formation of molecules like As_4 and P_4. Thus, a second heated zone called the cracking zone is held at significantly higher temperature to thermally "crack" the molecules into their constituent parts like As_2 or P_2. The cracker uses a large crucible to increase volume and accommodate more material for increased campaign time. The cracker source also uses a complex multi-piece design which operates like a needle valve, physically moving a plunger into the conductance tube to control the flux, or stop the flux altogether. For NH_3, thermal cracking is also required in order to break the NH_3 into its nitrogen and hydrogen constituents. This is generally accomplished by flowing ammonia gas through a conductance tube which is then supplied to the substrate through an aperture plate to spread out the flux uniformly. The ammonia itself is thermally cracked on the hot substrate at temperatures above 700°C, while the conductance tube is only heated slightly to prevent ammonia condensation.

N_2 supply is more complicated still, since N_2 is extremely inert. In order to make it reactive, a remote radio frequency (RF) plasma source is often employed. In the plasma source, the N_2 passes into a "bulb", typically made of pyrolytic boron nitride, with a conductance-limiting aperture plate on the end. The aperture plate allows the nitrogen pressure in the bulb to build up in the 10^{-3} Torr range where plasma can be sustained, while limiting the excess pressure in the main growth chamber. The plasma is generated using an inductive coil through which RF power is flowing at a typical frequency of 13.56 MHz. Some early ECR plasma designs for III-nitride MBE used microwave plasmas operating at frequencies of ~2.45 GHz, but they have generally been supplanted by the RF plasmas. The RF plasma generates several different nitrogen

species including ions, excited neutral atoms, and excited neutral molecules. While ions with high energy can damage the surface of the growing film, excited neutral atoms and molecules are reactive and will readily form the III-nitride compound on the substrate. Various reports in the literature point to both excited neutral species contributing to growth, but no clear consensus exists as to which species dominates.

Owing to the high vacuum conditions during III-nitride MBE growth with pressures on the order of 10^{-5} Torr, one or more powerful *in situ* characterization techniques can be employed. The primary example is reflection high energy electron diffraction (RHEED) wherein a high energy electron beam is incident on the crystalline surface at a glancing angle. Based on the crystal structure of the sample, the beam will diffract and appear as a pattern on a phosphor screen from constructive and destructive interference. Due to the small angle of incidence resulting in minimal penetration depth, RHEED is a highly surface sensitive technique which can be used real-time to characterize the growing surface. The pattern of the diffracted beam can give qualitative information as to the crystal structure and general surface morphology, and possibly quantitative feedback such as the lattice spacing of the film/substrate.

The primary alternative to MBE, and by far the most common technique for commercial growth of III-nitrides, is metalorganic chemical vapor deposition, or MOCVD. MOCVD operates at substantially higher pressures, typically around 100 Torr, for which the environment is dominated by fluid dynamics and viscous flow rather than the line-of-sight nature of MBE. MOCVD uses metalorganic precursors such as triethyl- or trimethylgallium for group III elements, which are typically diluted with N_2 or H_2 as a carrier gas. Nitrogen is supplied by the thermal decomposition of ammonia on the heated

substrate, and MOCVD substrate temperatures routinely exceed 1100°C. The thermal dissociation of the metalorganic precursors and the ammonia on the hot surface, and their subsequent reaction, forms the III-nitride film. Long migration lengths at high temperatures, as well as evaporation and re-condensation of growth constituents, allows MOCVD to grow very high quality films with smooth surfaces. Moreover, the gas flow mechanics and dramatically relaxed vacuum requirements mean MOCVD growth can be easily scaled to large areas and can also achieve high growth rates.

There are, however, several major drawbacks to MOCVD as well. Firstly, the metalorganic precursors are pyrophoric and ignite spontaneously if exposed to air, making them very dangerous to handle. The metalorganic precursors also contain carbon which can incorporate into the growing film if growth conditions are not carefully managed. The hydrogen-rich atmosphere in MOCVD is something of a two-edged sword. The hydrogen may help passivate dislocations and improve device electrical performance, but the hydrogen also passivates the Mg acceptor, resulting in an electrically inactive Mg-H complex.[17-19] This complex can be dissociated after growth by a thermal anneal in nitrogen, but complicates device fabrication and rarely results in hole concentrations $>10^{18}$ cm^{-3}. Another issue relating to MOCVD is the Mg memory effect, where the residual Mg in the chamber after p-type film growth can unintentionally incorporate into subsequent films due to the high vapor pressure of Mg. The complicated gas chemistry at higher temperatures and pressures can result in gas phase reactions which can degrade material quality, as well as cause macro defect formation and blurred interfaces in devices. Finally, the high temperatures required for the thermal cracking of ammonia result in extremely poor indium incorporation for

InGaN films. Thus, MOCVD is generally limited to indium fractions less than 20%, and even then the growth rates are dramatically reduced, often to below 100 nm/hour.

1.3 Challenges in the III-Nitride Material System

1.3.1 III-Nitride Substrates

One of the major challenges facing III-nitride devices is the lack of a suitable substrate which results in high dislocation densities. Typically, III-nitride device structures are grown on sapphire or SiC substrates with lattice mismatches vs. GaN of 14% and 3%, respectively.[20] Silicon has also garnered substantial interest as an alternative substrate due to the high thermal conductivity, large wafer sizes, and lower price, but it has an even worse lattice mismatch of 17%.[21, 22] Due to these highly lattice mismatched substrates, the epitaxially grown III-nitride films quickly reach the critical thickness for relaxation which generates large densities of misfit dislocations, as shown in the TEM cross-section image in Figure 1.5.[23] Even in device-quality structures for commercial LEDs, the threading dislocation density is often higher than 10^8 cm^{-2}, compared to a typical dislocation density of less than 10^5 cm^{-2} for traditional GaAs-based devices. These dislocations can act as current leakage paths which would be a major detriment to a solar cell.[24-26] Bulk GaN[27-30] and AlN[31, 32] substrates with dislocation densities less than 10^5 cm^{-2} are now commercially available with thicknesses exceeding 300 μm and diameters up to 2". However, the synthesis of these wafers is still relatively novel, and the wafers are prohibitively expensive for most research use and even for most commercial use except for the highest performance devices.

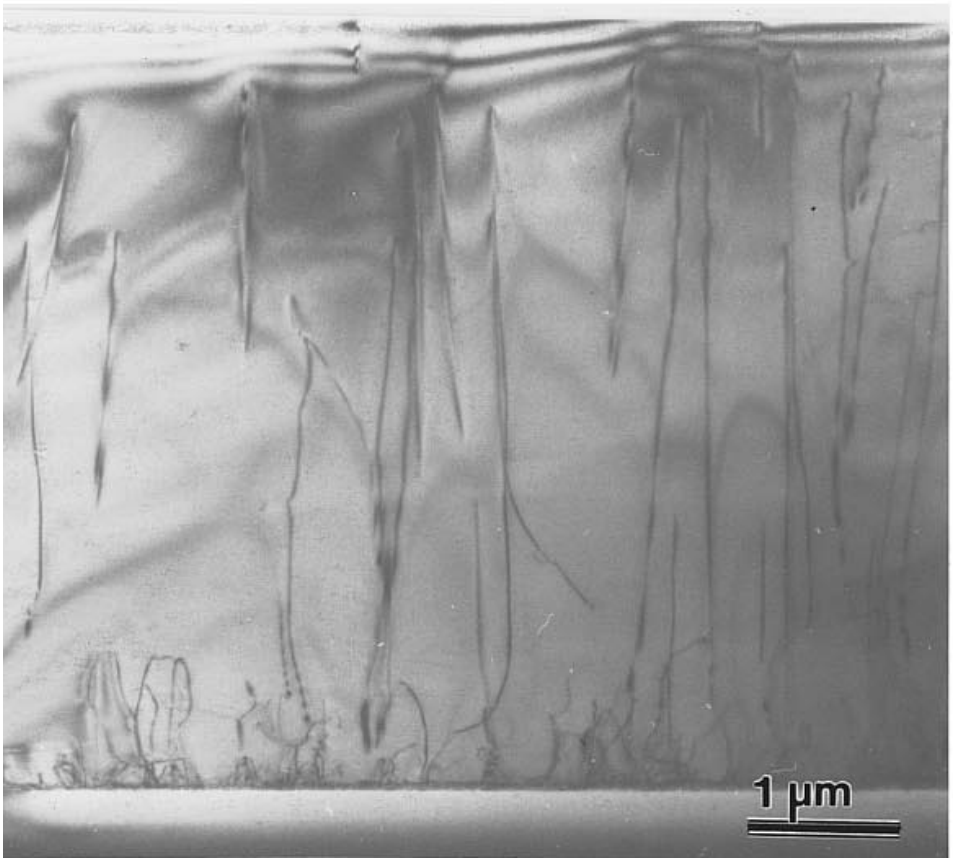

Figure 1.5: TEM cross-section for a typical GaN film with threading dislocations clearly visible on the order of 10^8-10^9 cm^{-2}. [23]

In the particular case of III-nitride growth on silicon substrates, which is typically performed using metalorganic chemical vapor deposition (MOCVD), complex buffer layers are almost always employed in order to mitigate several detrimental effects during and after growth. Prior to the initiation of III-nitride growth, a thin seed layer of aluminum is often deposited on the Si substrate.[22, 33, 34] This prevents, or at least minimizes, the formation of an amorphous SiN_x phase at the growth interface.[35] After this Al seed layer, a ~20 nm thick AlN layer is typically grown prior to the growth of a >1 µm thick GaN layer. The AlN serves as an insulating barrier to isolate the GaN from the

conductive Si substrate and also results in a change in the stress of the GaN film after the as-grown wafer cools. Due to the large thermal coefficient of expansion mismatch between GaN and Si, the cool-down from MOCVD growth temperatures near 1000°C often results in the GaN film cracking.[21, 36] The GaN lattice contracts during cool-down faster than the underlying Si wafer which induces an in-plane tensile stress on the GaN film causing it to crack, as shown in Figure 1.6.[37]

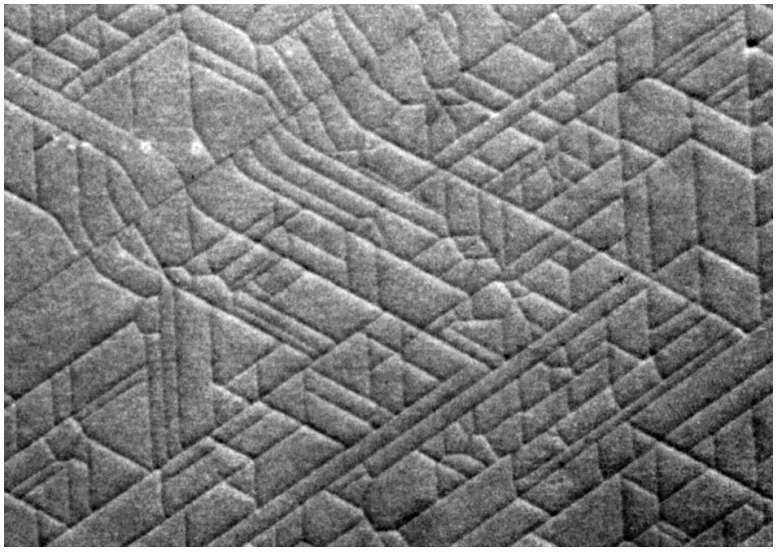

Figure 1.6: GaN film grown on Si by MOCVD exhibiting cracking from tensile stress during cool-down after growth. [37]

Thicker films are more susceptible to cracking due to the inherent increase in total tensile stress, but thicker films are more desirable since larger thickness causes dislocations to terminate which improves the final film quality. Thus, AlN buffer layers and interlayers, as well as complex AlGaN- and AlN-bearing superlattice (SL) structures are often employed to induce a compressive stress in the GaN film during cool-down.[38-42] This compressive stress opposes the tensile stress caused by the Si substrate, which in

turn results in a reduction in the final GaN film stress and effectively prevents cracking.[36, 43] Molecular beam epitaxy (MBE) does offer some advantages when growing on Si due to the lower growth temperatures of 600-900°C. However, thick GaN films grown by MBE at moderately high temperatures on Si can still exhibit cracking which must be prevented by other strain-compensating buffer layers.[44]

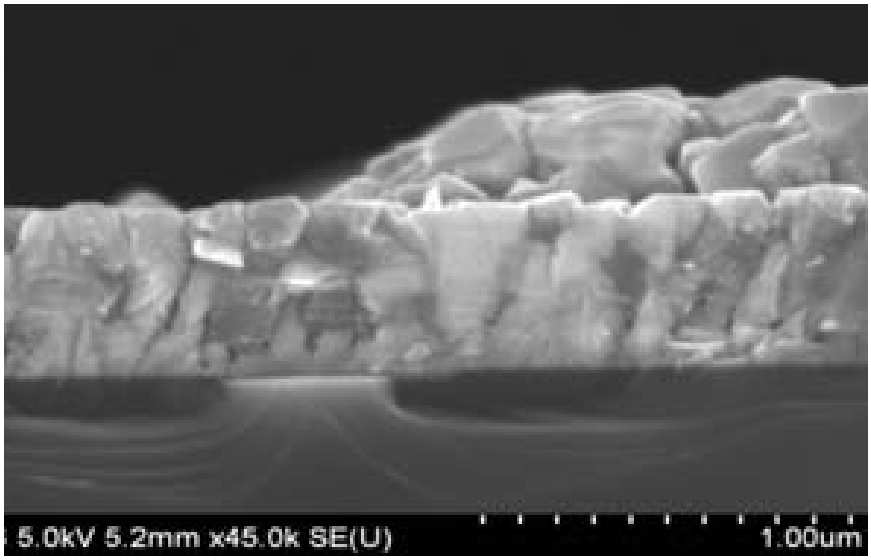

Figure 1.7: Cross-section SEM image of GaN on Si grown by MBE demonstration melt-back etching and subsequent polycrystalline film growth. [45]

Another major issue to consider when growing III-nitrides on Si substrates is the existence of Al-Si, Ga-Si, and In-Si eutectics. The eutectic, a low-melting point alloy phase of the metal-Si system, can cause "melt-back etching" whereby the Si substrate can partially dissolve into a metal cluster or droplet.[46] This melt-back results in large extended defects, interfacial voids, and substantially deteriorated crystal quality and surface morphology,[47] particularly when the growth occurs under metal-rich conditions, as shown in Figure 1.7.[45] In addition, the Si dissolution into the metal also results in

substantial migration of the Si into the films which can cause uncontrolled n-type doping. The aluminum seed layer, discussed above for tensile stress, can also help avoid this melt-back etching. By depositing a few monolayers of metallic Al at low temperature, followed by a thin AlN buffer layer, the Ga is never allowed to directly reach the Si substrate which prevents the intermixing of Ga/Si. This is even more important in the case of metal-rich MBE where an excess of liquid metal is supplied to the growth surface.

1.3.2 Indium-Bearing III-Nitride Alloys

For solar cells, III-nitrides appear to be an outstanding candidate for the reasons mentioned above as well as for possible space applications owing to their radiation tolerance.[48] However, the potential for high efficiency III-nitride solar cells has yet to be realized for several critical reasons. Perhaps the largest issue facing III-nitride photovoltaics is the inability to grow thick, low-defect density films with high indium fraction. While LEDs with low indium composition (< 20%) are typically grown by MOCVD, the growth of high indium content InGaN is extremely challenging. For a single junction solar cell, the ideal band gap for maximum efficiency is around 1.5 eV which corresponds to an indium composition on the order of 55%. At this indium composition, dramatically lower growth temperatures are required compared to GaN, and as the temperature decreases, so too does the cracking efficiency of ammonia.[49, 50] Thus, MOCVD growth of higher indium composition InGaN is extremely slow, which makes thick solar-relevant films impractical. Moreover, InGaN is sensitive to high temperatures which can result in diffusion to form higher-indium composition regions, a phenomenon referred to as phase separation.[51, 52]

The phase separation phenomenon comes about from the immiscibility of InN and GaN due to their large difference in interatomic spacing, causing the materials to separate into regions of different composition in order to minimize free energy.[53] Phase separation is a major problem even in MBE-grown InGaN which occurs at lower substrate temperatures than traditional MOCVD.[54, 55] Because of this immiscibility of InN and GaN, an effect which is most pronounced at the middle of the alloy composition range, solar-relevant InGaN films are notoriously difficult to grow. When grown by MOCVD, thick InGaN films tend to roughen dramatically, particularly at higher indium composition, due to the formation and propagation of V-pits as shown in Figure 1.8.[56]

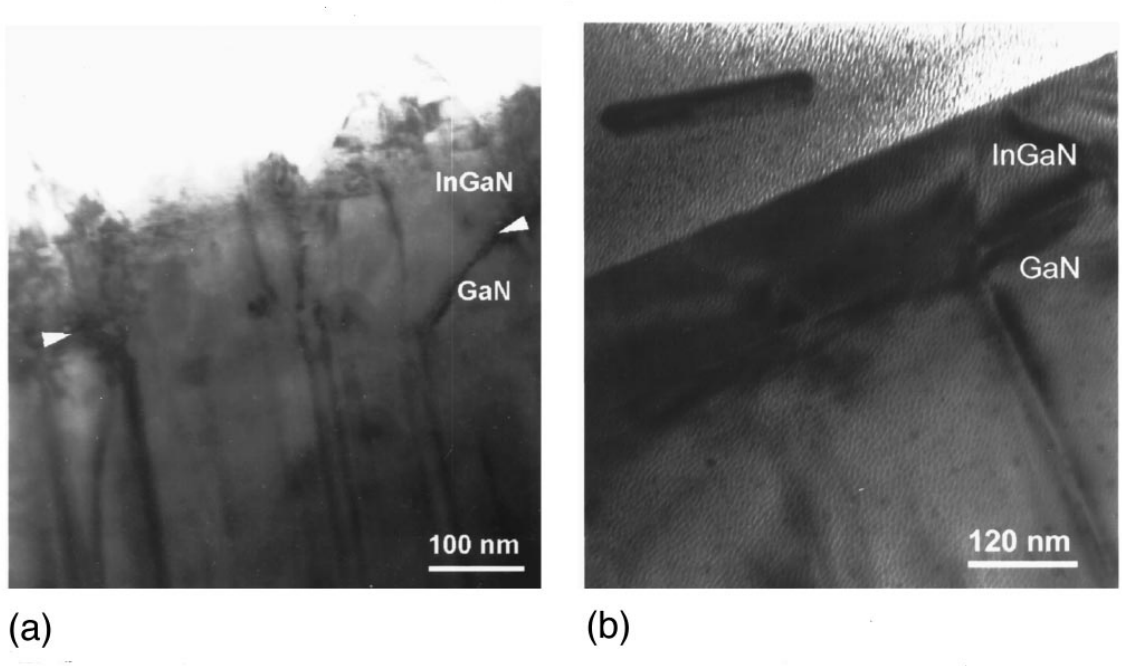

Figure 1.8: Cross-sectional TEM showing a highly defective thick InGaN film grown by MOCVD (left) and a smoother, higher quality InGaN film grown by MBE (right). [56]

Thus, the majority of InGaN solar cells are grown using a multi-quantum well structure in order to avoid V-pit propagation by inserting GaN interlayers to maintain a

smooth surface.[57, 58] In addition, these solar cells also use low indium compositions which are unusable for practical solar cells since they only absorb the short-wavelength portion of the solar spectrum where the incident power is weak. Moreover, the structure of a MQW with quantum confinement is inherently poor for solar cells where the goal is to extract carriers, not trap them. Thus, thick InGaN layers would provide a better alternative. Some promising results have been presented in recent years for InGaN/GaN heterostructure solar cells using thicker InGaN layers, but these have similarly been limited to low indium fractions under 15% which limits the practical applications due to the large bandgap energy.[59, 60]

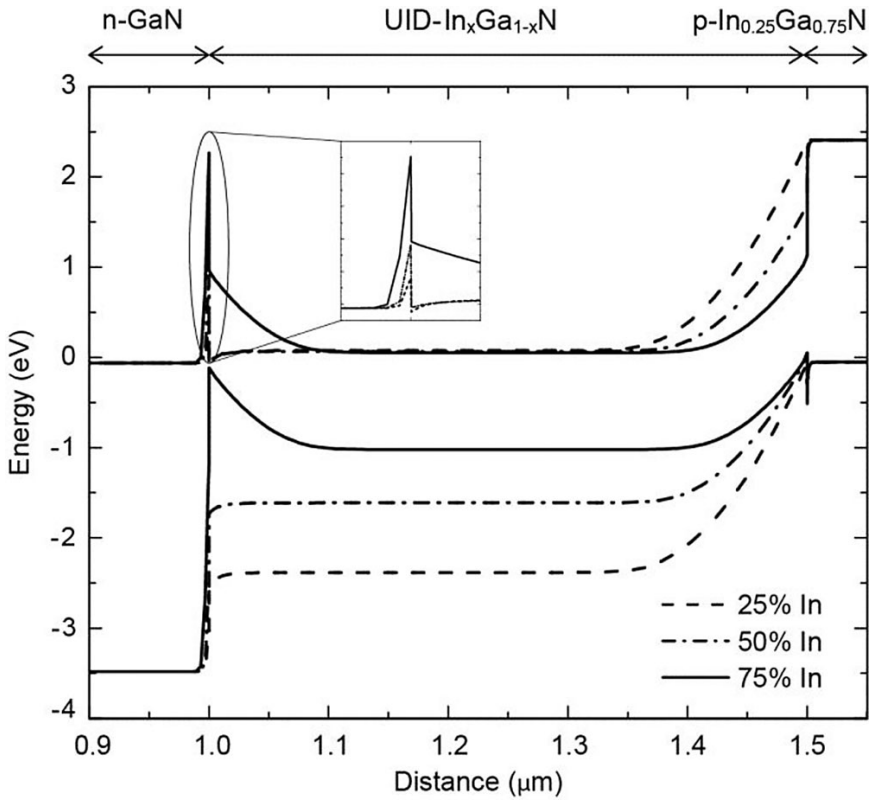

Figure 1.9: Energy band diagram for a InGaN/GaN heterojunction solar cell showing a massive potential barrier at the n-GaN to UID-InGaN interface due to spontaneous and piezoelectric polarization effects. [13]

In addition to the inherent challenges in the growth of InGaN, the spontaneous and piezoelectric polarizations present in the III-nitride system make simple structures ineffective. When dissimilar III-nitride layers are grown on one another, as is the case for an InGaN/GaN heterojunction, the mismatch in the polarization between the two layers causes substantial band-bending at the interface as shown in Figure 1.9. This band-bending can dramatically hinder carrier collection in a heterojunction solar cell and limits the alloy compositions during device design.[5, 13, 61-63] In the case of a more ideal InGaN homojunction solar cell, the structure is further complicated by p-type doping, particularly at high indium compositions.

1.3.3 P-type Doping of III-Nitrides

P-type doping is a major impediment to viable III-nitride solar cells, and even has significant detrimental effects on the performance of existing commercial devices like the white LED. In state-of-the-art device structures, the free hole concentration in the p-type layer is typically on the order of 10^{17} to low-10^{18} cm^{-3} with resistivity of 1-5 Ω-cm. The inability to achieve higher p-type doping has been ascribed to the high activation energy of the Mg acceptor which is typically reported to be in the range of 140 to 220 meV and, combined with low hole mobility of 1-20 $cm^2/V\text{-}s$, results in high resistivity compared to other p-type semiconductors.[64-67] In addition to the deep acceptor energy, several other issues arise when using high Mg concentrations with traditional growth techniques like MOCVD and MBE. As shown in Figure 1.10, Mg precipitation is often seen in p-GaN grown by MOCVD with high Mg concentrations which results in extended defects,

inversion domains, and cubic inclusions.[68, 69] In films grown by MBE, a complete polarity inversion from Ga-polar to N-polar has been seen when using excessive Mg concentrations.[70, 71] Some improvements have been made for p-type doping in MBE at high temperatures, but hole concentrations have still been limited to ~$3x10^{18}$ cm^{-3}.[72, 73] These low hole concentrations make a traditional tunnel junction impossible, which will directly limit the viability of III-nitrides as a high efficiency solar cell material.

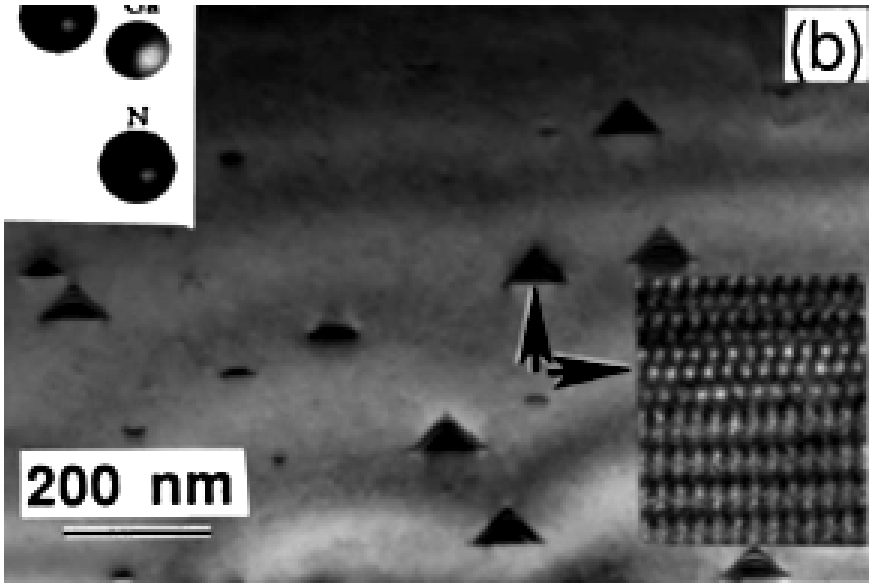

Figure 1.10: Cross-sectional TEM image of a MOCVD-grown highly Mg-doped GaN film with Mg concentration of ~$5x10^{19}$ cm^{-3} showing pyramidal defects leading to stacking faults, cubic inclusions, and polarity inversion. [68]

At the high growth temperatures of MOCVD, p-type doping is especially challenging because point defects such as nitrogen and gallium vacancies have lower formation energies at high temperatures, as shown in Figure 1.11.[18, 74, 75] This is particularly critical in the case Mg-doped GaN where it has been shown that Mg substituting on a Ga site (Mg_{Ga}) can form a complex with a nitrogen vacancy (V_N).[76]

The V_N formation energy is reduced in p-type GaN, and the nitrogen vacancy acts as a donor, compensating the Mg_{Ga}. This self-compensation is exacerbated by high growth temperatures where the formation energy of the Mg_{Ga}-V_N complex is favorable.[18] Thus, GaN with large concentrations of Mg grown at high temperature becomes heavily compensated which severely limits the hole concentrations achieved under typical growth conditions.

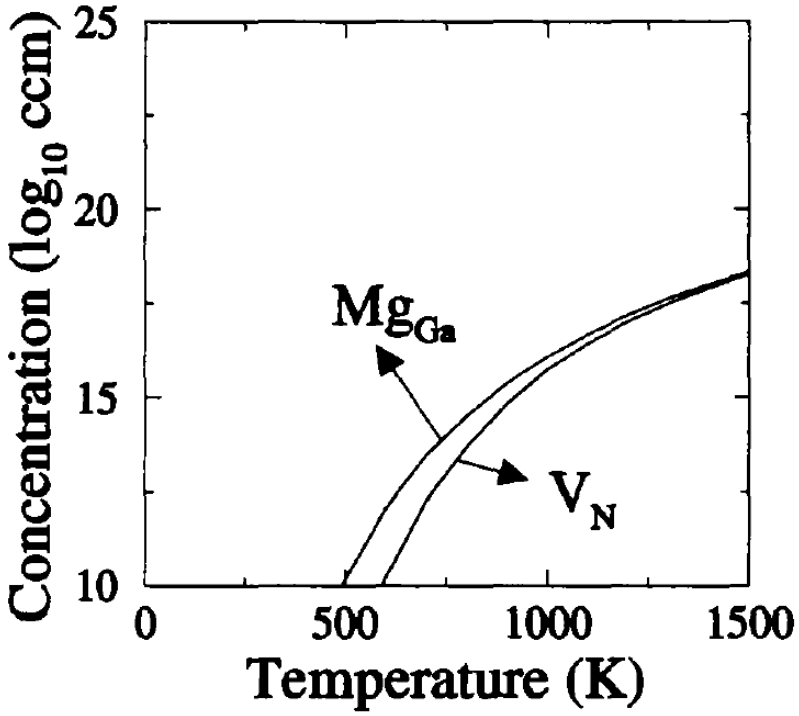

Figure 1.11: Semi-log plot of concentration vs. temperature for the Mg_{Ga} substitution and V_N which readily combine to form a self-compensating complex at typical MOCVD growth temperatures of >1100K.[18]

CHAPTER 2: NEGLIGIBLE CARRIER FREEZE-OUT FACILITATED BY IMPURITY BAND CONDUCTION IN HIGHLY P-TYPE GaN

1.1 Introduction

Group III-nitride semiconductors possess a number of excellent properties which make them viable for a broad range of electronic and optoelectronic devices. These properties include a tunable, direct bandgap of ~0.7 – 6.1eV, high drift velocity, high mobility, and strong light absorption.[1-3] Together these attributes make III-nitrides suited for light-emitting diodes (LEDs), high electron mobility transistors (HEMTs), and potentially solar cells and heterojunction bipolar transistors (HBTs).[4, 5] However, p-type doping of III-nitrides, a key component for many devices, remains extremely challenging. Typical hole concentrations for p-type GaN in literature are on the order of 10^{17}-10^{18} cm^{-3}, and some of the highest reported hole concentrations barely exceed 10^{18} cm^{-3} for GaN grown on c-plane sapphire.[72] The low hole concentrations are attributed to the large activation energy of the magnesium dopant atom, often reported to be 140 – 220 meV which lead to poor ionization efficiencies of 1-5% at the highest doping concentrations.[72, 73]

The inability to achieve higher p-type doping is one possible cause of the efficiency droop seen in nitride-based LEDs,[77, 78] and directly prevents the formation of a tunnel junction critical to multi-junction solar cells. In addition, high p-type contact and base access resistance has been cited as a primary cause of performance limitations in nitride HBTs.[79] These performance limitations might be alleviated by improved p-type

doping. In recent years, higher hole concentrations and reduced resistivities in p-type GaN have been reported using a modified form of molecular beam epitaxy (MBE) called Metal-Modulated Epitaxy (MME).[80, 81] The details of this shuttered technique have been explored in previous publications.[82] Growth of p-type GaN by MME has led to room temperature hole concentrations in excess of 10^{19} cm^{-3} and room temperature resistivities below 0.3 Ω-cm.[83, 84] This present study demonstrates improvements in p-type conductivity and insight into the temperature-dependent properties of p-type GaN films grown by MME, and suggests impurity band conduction as the physical mechanism responsible for these improvements in the p-type electrical properties.

2.1 Experimental Setup

All films in this paper were grown by Metal-Modulated Epitaxy in a Riber 32 MBE reactor with a base pressure of $1x10^{-10}$ Torr. The substrate used for all films was 1x1cm single-side polished c-plane sapphire with 2μm tantalum backside metal. Substrates were outgassed at 300°C for 30 minutes prior to growth. Low-temperature nitridation of the sapphire substrate was performed at 200°C for 60 minutes.[85-88] Compared to high-temperature nitridation, low-temperature nitridation has been shown to result in higher quality, homogeneous AlN layers leading to improved GaN films.[85-88] Reactive nitrogen species were supplied by a Veeco UNI-Bulb RF plasma source operating at 350W RF power and 1.3 sccm N_2 flow. Following low-temperature nitridation, a 100nm AlN buffer layer was grown via MME at 700°C to provide a Al-polar surface for subsequent growth.[87, 89-92] The aluminum flux during the buffer

layer growth was $6x10^{-7}$ Torr beam equivalent pressure (BEP), and the aluminum shutter cycle was 10s open/10s closed. After growth of the AlN buffer layer, the substrate temperature was reduced to 600°C for growth of p-type GaN:Mg films. Magnesium was delivered by a Veeco corrosive series valved cracker with a bulk temperature of 280 – 300°C and a valve opening of 120 mils.[93] No unintentionally doped or n-doped GaN layers were grown so as to ensure all electrical measurements resulted from only the p-type GaN. Gallium was supplied by either a standard effusion cell or a Veeco SUMO® cell at a metal-rich flux of $6.5x10^{-7}$ to $7.5x10^{-7}$ Torr BEP. Gallium and magnesium were shuttered simultaneously with a cycle of 5s open/10s closed. Reflection High Energy Electron Diffraction (RHEED) was performed in-situ to aid in determining the optimal III-V flux ratio for doping as described by Namkoong et al.[83] A summary of the varied growth conditions is shown in Table 2.1. It is important to note that, due to effusion cell design and flux gauge geometric considerations, the stoichiometric flux for Ga is different between the two types of effusion cells leading to different III/V ratios for a fixed N-plasma condition. As such, the approximate III-V ratios determined from the flux resultant in Ga droplet formation are also shown in Table I to clarify the two different metal-rich conditions.

Table 2.1: P-type GaN:Mg growth conditions.

	Effusion Cell Type	***Ga Flux (Torr)***	***III/V ratio***	***Mg Bulk Temp***	***Growth Time***
Sample A	standard	$7.5x10^{-7}$	~1.6	280ºC	40 mins
Sample B	SUMO®	$6.5x10^{-7}$	~1.1	300ºC	30 mins

Structural characterization was performed after growth by x-ray diffraction

(XRD) using a Philips X'Pert Pro MRD equipped with a high resolution goniometer. Surface morphology was determined by a Veeco Dimension 3100 atomic force microscope (AFM) operating in tapping mode. Electrical properties of the p-type GaN films were determined using a custom temperature-dependent Hall-effect system. The Hall system consisted of a MMR Joule-Thomson thermal stage operating from 77K to 400K under a Walker Scientific two Tesla electromagnet and high-precision Keithley electronics including a model 2128A nanovoltmeter, model 7001 switch matrix with Hall measurement card, and model 6221 current source operating in DC mode. The Hall effect measurement procedure follows ASTM Standard F76.[94] Given the unusually high hole concentrations reported herein, previous samples were verified externally to insure no systematic error in the Hall measurements. Measurements in our lab agreed to within 5% to that measured elsewhere and these results have been previously published.[84] Representative samples were also sent out to be analyzed using secondary ion mass spectrometry (SIMS) to determine Mg incorporation in MME grown p-type GaN films.

2.2 Crystal Quality and Surface Morphology of Highly P-Type GaN

The p-GaN thickness of Sample A found by contact profilometry was approximately 300 nm after subtracting out the thickness of the insulating AlN buffer. The p-GaN thickness of Sample B was 100 nm. For heavily Mg-doped films grown by MME the full width at half maximum (FWHM) of the (0002) omega rocking curve is typically on the order of 1000 to 1500 arcseconds.[84] Often attributed to the typically nitrogen-rich growth conditions, Mg doping of MBE-grown GaN films has been shown

to degrade the crystal quality detected by XRD.[95-97] In the case of these two MME-grown samples, a time-average nitrogen rich condition is maintained even though the instantaneous (shutter open for 1/3 duty cycle) condition is Ga-rich. As such, the relatively broad FWHM exhibited by these films, approximately 3-4 times normal for MME-grown undoped or Si-doped GaN films, are not unexpected given the time-average nitrogen rich growth conditions and unusually high doping levels in excess of 1-2x10^{20} cm^{-3} as determined by SIMS.[84]

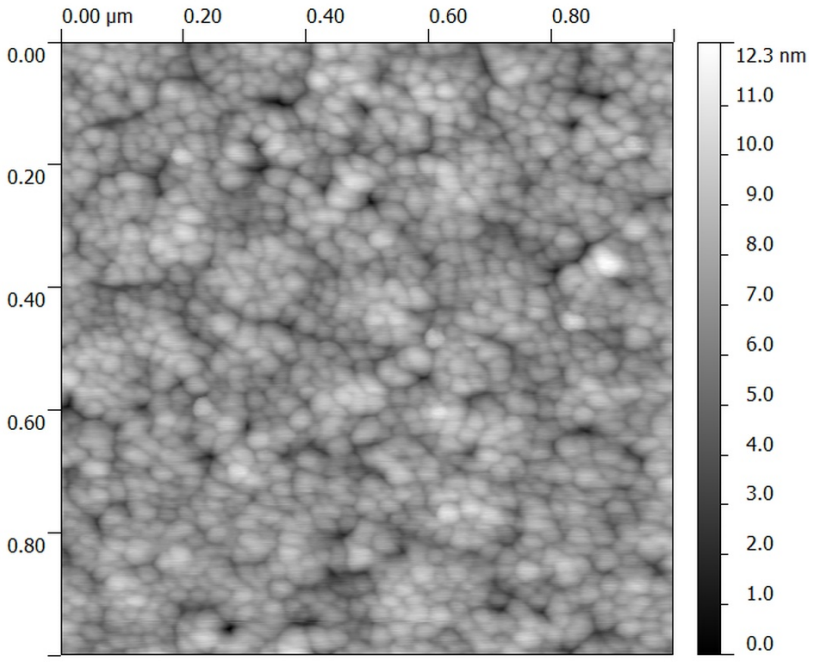

Figure 2.1: 1x1µm AFM of p-type GaN:Mg film (RMS roughness = 1.27 nm).

The AFM surface morphology of a p-type GaN:Mg grown by MME with room temperature hole concentration of 1.6x10^{19} is shown in Figure 2.1. The film exhibits a grainy morphology with RMS roughness of 1.3 nm. This rough surface is also attributed to the large concentration of Mg dopants in the film and the time-average nitrogen rich

growth conditions used for optimal p-type doping.[83] For comparison, an RMS roughness on the order of 0.5-2 nm is typical for lighter-doped GaN:Mg films grown by MOCVD and traditional MBE.[98, 99] Undoped and Si-doped MME films typically show lower than 0.5 nm RMS roughness comparable to other growth techniques but achievable at relatively lower substrate temperatures.

2.3 Electrical Properties: Traditional vs. Highly P-Type GaN

Shown in Figure 2.2i-iv respectively are the temperature-dependent resistivity, mobility, carrier concentration, and Hall coefficient for the two p-type GaN films grown by MME with slightly differing Ga and Mg flux. A full study showing the sensitivity of hole concentrations to these parameters will be presented in a later paper. These two representative samples grown under different conditions are presented to compare the electrical behavior of traditional low 10^{18} cm^{-3} hole concentration materials to those having hole concentrations in excess of 10^{19} cm^{-3}. Differences in electrical response are observed not only in hole concentration but also in the relative levels of compensation, an important mechanism needed to understand the limitations in traditional doping.

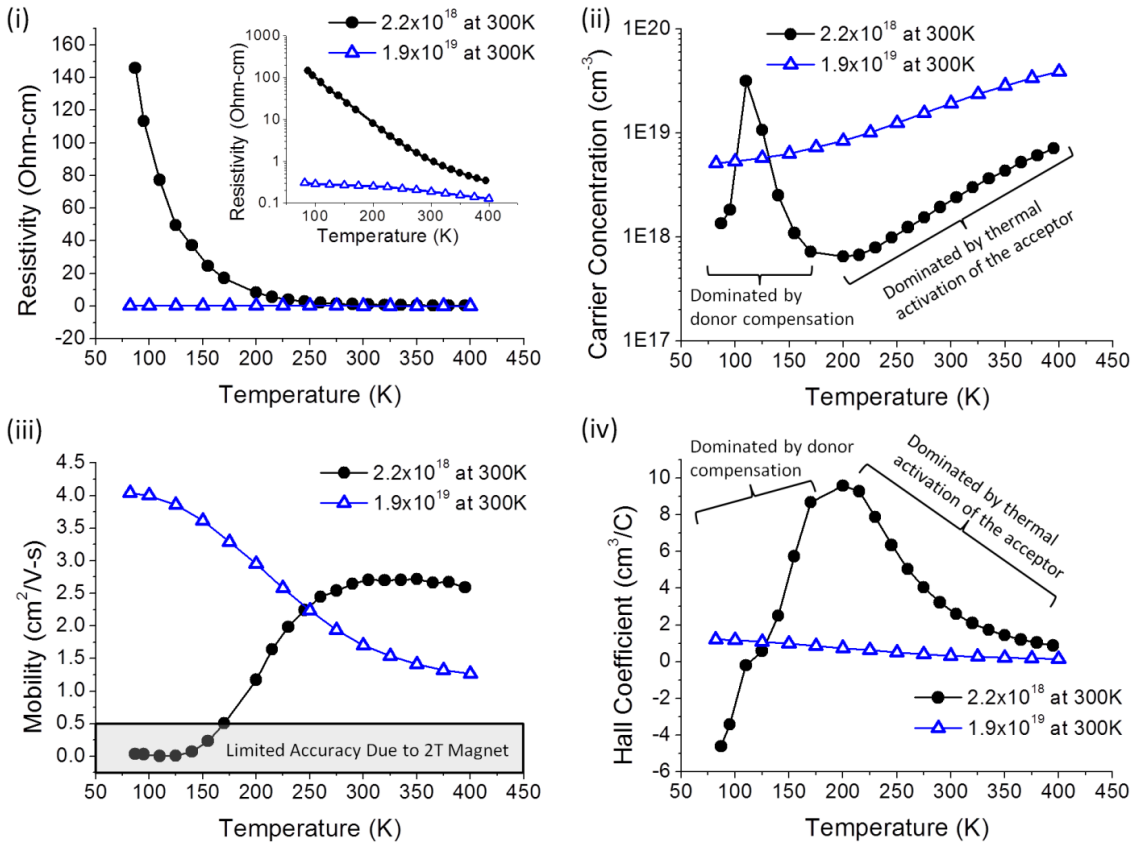

Figure 2.2: Temperature-dependent resistivity (top left, log plot inset), carrier concentration (top right), Hall mobility (bottom left), and Hall coefficient (bottom right) for comparitive p-GaN films.

It is clear from Figure 2.2i-iv that the different growth conditions lead to dramatically different electrical properties in the two films. In Figure 2.2i, Sample A exhibits classical carrier freeze-out, resulting in high resistivity. However, as the thermally activated acceptors freeze out with decreasing temperature, compensating donors begin to have more effect on the conduction. This is evident in Figure 2.2ii and Figure 2.2iv where, at approximately 200K, the slope of the Hall coefficient turns positive and the carrier concentration begins to rise. At approximately 125K the Hall coefficient approaches zero indicating complete compensation. In this temperature range

there is a corresponding asymptote in the carrier concentration due to the inverse relationship between hole concentration and Hall coefficient. The calculated carrier concentration in this temperature range should not be considered valid due to the dominance of compensation. Below 125K the Hall coefficient is negative, indicating n-type conductivity due to the holes having frozen out below the level of compensating donors, estimated to be in the upper 10^{17} cm^{-3} range. An additional measurement consideration is that at approximately 175K the Hall mobility in Figure 2.2iii drops below the detectable limit allowed by the two Tesla magnetic field (mobility μ must be greater than 1/B, where B is the magnetic field measured in Tesla).[100] As such, any mobility data points below 175K should be approached with caution due to this accuracy limitation set by the hardware.

In contrast, Sample B exhibits very different electrical properties versus the lighter doped sample A, and its resistivity shows very little temperature dependence at all. For reference, the resistivity of Sample B is 0.19 Ω-cm at 300K and only 0.30 Ω-cm at 82K. In addition, the mobility of Sample B increases from 1.7 cm^2/V-s at 300K to 4.0 cm^2/V-s at 82K. Finally, the hole concentration of Sample B only drops by a factor of 3.8, from $1.9x10^{19}$ at 300K to $5.1x10^{18}$ at 82K. This lack of carrier freeze out at cryogenic temperatures is not characteristic of even the most heavily doped p-type GaN:Mg films grown by traditional MBE or MOCVD which typically show a temperature dependence similar that of Sample A.[95, 99] The effective activation energy extracted from the temperature dependent hole concentration in the upper temperature regime for the highly doped Sample B was calculated to be just 70 meV, compared to the 140 – 220 meV commonly reported. It is important to note that, due to

the proposed mechanism of an acceptor band discussed below, rather than a single acceptor energy level, the traditional calculation of activation energy is not accurate for very heavily doped films and is presented here merely for the purposes of qualitative comparison.

2.4 Trends in Activation Energy vs. Hole Concentration

A separate set of growths with varied room temperature hole concentrations are shown in Figure 2.3. In this Arrhenius plot of natural log of resistivity vs. 1000/T, there is a clear trend in the temperature-dependent electrical properties as the hole concentration changes. The sample with 2.9×10^{18} cm^{-3} room temperature hole concentration has a resistivity of 155 Ω-cm at 86K, while the sample with 8.0×10^{18} cm^{-3} hole concentration only has a resistivity of 11.6 Ω-cm at 87K. This 2.75x increase in room-temperature hole concentration leads to a full order of magnitude improvement in the low-temperature resistivity. The third sample with 2.8×10^{19} cm^{-3} hole concentration takes this improvement further still with a resistivity of just 1.5 Ω-cm at 87K.

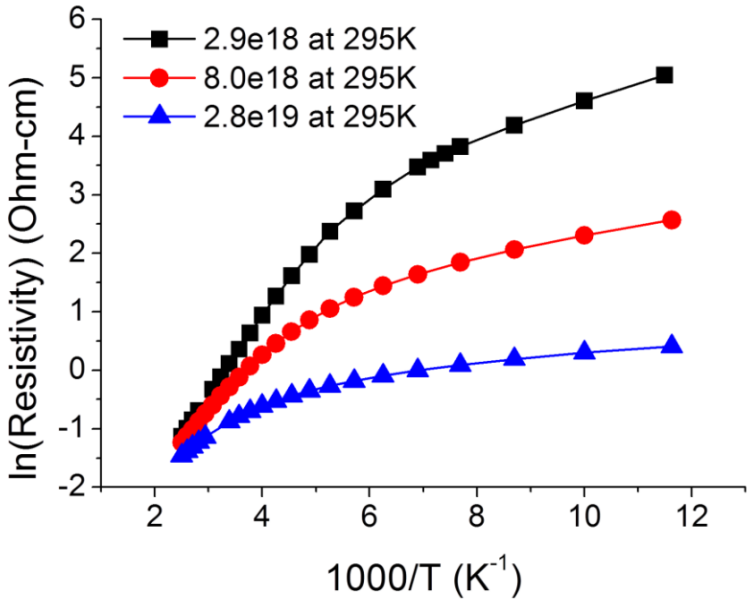

Figure 2.3: Trend of temperature-dependent resistivity for three samples with different room temperature hole concentrations.

In addition to the trend in low-temperature resistivity, there is also a similar trend in effective activation energy. As the hole concentration increases, the effective activation energy decreases. From the lowest to highest hole concentration (top to bottom in Figure 2.3), the effective activation energies, calculated from the high temperature regime of the temperature-dependent hole concentration, are 111 meV, 55 meV, and 43 meV respectively. While all of these values are lower than those typically reported in literature, the trend illustrates the important relationship between this effective activation energy and the hole concentration. This trend along with the lack of carrier freeze out shown in Figure 2.2 implies the formation of an acceptor band as opposed to the traditional isolated acceptor.

Representative samples were also sent for SIMS analysis. A previous publication[84] reported high Mg acceptor ionization efficiencies of 10% grown by

MME. Figure 2.4 shows a sample with Mg concentration of 1.3×10^{20} cm^{-3} and a room temperature hole concentration of 6.7×10^{19} cm^{-3} leading to a Mg acceptor ionization efficiency of approximately 52%.

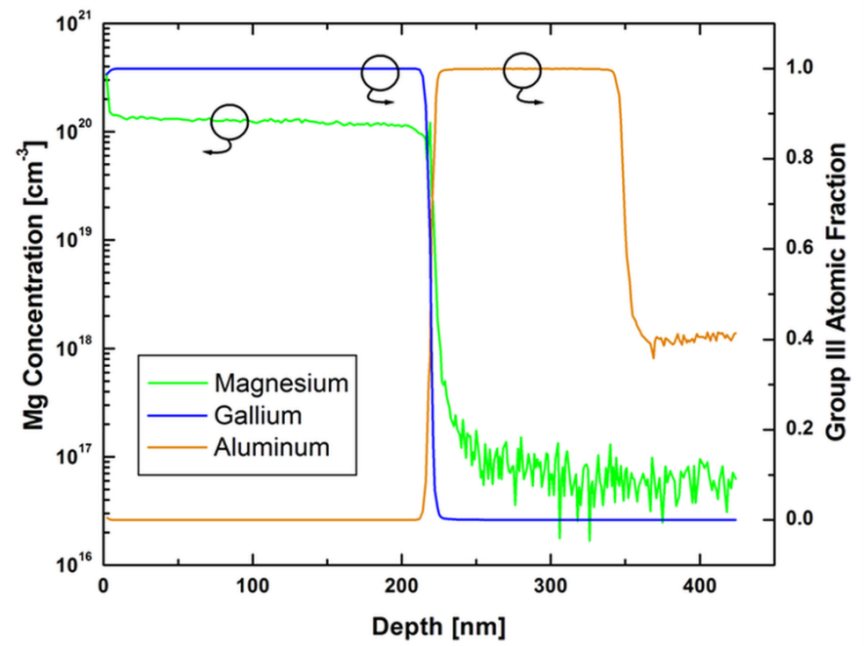

Figure 2.4: SIMS depth profile for MME-grown GaN:Mg film with 52% Mg activation.

Together, the temperature dependent behavior of Sample B, low activation energy, and unusually high Mg concentration in the film point to the onset of an impurity band. As the electrically active acceptor concentration increases, the isolated deep acceptor energies begin to interact and must, according to the Pauli Exclusion Principle, split into a band of states. This results in the Fermi-energy becoming pinned inside the acceptor band which leads to the lack of temperature dependence of the electrical properties as evident in the highly doped case in Figure 2.2. As the concentration of electrically active acceptors, ionized Mg located on the proper Ga-substitutional site,

increases the acceptor energy splitting pushes this acceptor band closer toward the valence band lowering the effective activation energy. Without the formation of an impurity band and the associated reduction in effective activation energy, this large activation efficiency of 52% is not possible at room temperature for a single isolated deep acceptor traditionally found in p-type GaN. This traditional impossibility results from the Fermi-level in p-type GaN being far below the acceptor energy resulting in significant emptying of the acceptor state. The 43 to 70 meV effective activation energy is in line with that reported in a previous publication,[84] but the low-temperature resistivity has been improved by over an order of magnitude due to more optimized growth conditions. Growth conditions optimized for higher hole concentration, which will be explored in detail in a future study, result in a best hole concentration of nearly 7.9×10^{19} cm^{-3} but a slightly inferior resistivity of 0.26 Ω-cm.

2.5 Conclusions

P-type GaN:Mg films have been grown using Metal-Modulated Epitaxy with varied Ga and Mg flux on c-plane sapphire substrates. A resistivity of 0.30 Ω-cm and hole concentration of 5.1×10^{18} cm^{-3} have been demonstrated at cryogenic temperatures and 1.9×10^{19} cm^{-3} and 0.19 Ω-cm at room temperature. In contrast, a lighter doped film exhibited resistivity of 146 Ω-cm and donor-compensated conductivity at cryogenic temperatures. Temperature dependent Hall effect analysis of the heavily doped MME-grown film indicates Mg effective activation energies as low as 43 meV which varied with hole concentration supporting the conclusion of the formation of an energy band

whose energy splitting is concentration dependent. Finally, a Mg acceptor ionization efficiency of 52% has been demonstrated by comparing the SIMS depth profile to carrier concentration. Overall, the electrical properties of the highly doped film and the lack of temperature dependent behavior point to impurity band conduction as the primary mechanism explaining these results.

CHAPTER 3: COMPREHENSIVE STUDY OF THE ELECTRONIC AND OPTICAL BEHAVIOR OF HIGHLY DEGENERATE P-TYPE Mg-DOPED GaN AND AlGaN

3.1 Introduction

While group III-nitride semiconductors possess many properties which make them desirable for a range of electronic and optoelectronic devices, p-type doping in III-nitrides remains a substantial challenge.[101, 102] In state-of-the-art device structures, the free hole concentration in the p-type layer is typically on the order of 10^{17} to low-10^{18} cm^{-3} with resistivity of 1-5 Ω-cm. The inability to achieve higher p-type doping has been ascribed to the high activation energy of the Mg acceptor which is typically reported to be in the range of 140 to 220 meV and, combined with low hole mobility of 1-20 cm^2/V-s, results in high resistivity compared to other p-type semiconductors.[64-67] In addition to the deep acceptor energy, several other issues arise when using high Mg concentrations with traditional growth techniques like MOCVD and MBE. Mg precipitation is often seen in p-GaN grown by MOCVD with high Mg concentrations which results in extended defects, inversion domains, and cubic inclusions.[68, 69] In films grown by MBE, a complete polarity inversion from Ga-polar to N-polar has been seen when using excessive Mg concentrations.[70, 71] Some improvements have been made for p-type doping in MBE at high temperatures, but hole concentrations have still been limited to ~$3x10^{18}$ cm^{-3}.[72, 73]

Low-temperature MBE, on the other hand, has shown the ability to grow GaN with very high Mg concentrations up to $3x10^{20}$ cm^{-3} free of inversion domains and Mg precipitation.[103] In more recent years, this low-temperature GaN MBE growth at

550°-600°C has been explored further using the Metal-Modulated Epitaxy (MME) growth technique, a variation of MBE where metal sources are periodically modulated while the impingent nitrogen flux remains constant.[81, 82, 104] In MME growth, metal-rich fluxes are used to build up excess metal into an adlayer, and then the excess metal is consumed by the continuous nitrogen flux after the metal shutters close. Using this technique, p-type GaN films have been achieved with hole concentrations as high as $7.9x10^{19}$ cm^{-3} with a resistivity as low 0.2 Ω-cm.[83, 84, 105] These films showed minimal carrier freeze-out and remained highly p-type even at cryogenic temperatures. Moreover, the films showed an effective activation energy which was strongly dependent on the hole concentration, ranging from 110 meV down to just 43 meV for films with a hole concentration of $3x10^{18}$ cm^{-3} and $3x10^{19}$ cm^{-3}, respectively. The mechanism for this reduction in effective activation energy was ascribed to impurity band conduction which also resulted in minimal temperature dependence of the electrical properties, in stark contrast to more traditional p-GaN films which show carrier freeze-out and high resistivity at low temperatures.[64, 106-108]

The low-temperature growth with MME is beneficial for several key reasons including reduced point defect formation, improved temperature and thickness uniformity, simplified alloy control due to minimal desorption, and more efficient Mg incorporation. When using lower growth temperatures, the temperature uniformity across the substrate is substantially improved resulting in more usable surface area and faster growth rates. In addition, point defects such as nitrogen and gallium vacancies have higher formation energies at low temperatures.[18, 74, 75] This is particularly critical in the case Mg-doped GaN where it has been shown that Mg substituting on a Ga site

(Mg_{Ga}) can form a complex with a nitrogen vacancy (V_N).[76] The V_N formation energy is reduced in p-type GaN, and the nitrogen vacancy acts as a donor, compensating the Mg_{Ga}. This self-compensation is exacerbated by high growth temperatures where the formation energy of the Mg_{Ga}-V_N complex is favorable.[18] By growing at low substrate temperatures using MME, this type of point defect and defect complex can be suppressed. Moreover, dramatic improvements in Mg incorporation are possible at low temperatures due to reduced Mg desorption from the growth surface.[103, 109] However, the major concern with growing at low temperature is extended defect formation, degraded crystal quality, and substantially rougher surface morphology resultant from limited adatom surface diffusion lengths.[110] Since atoms diffuse on metallic layers instead of semiconducting layers, MME mitigates the low diffusion length effects by building up a metal adlayer[111, 112] which results in dramatically higher adatom surface mobility and smoother surface morphology.[110, 113-115]

In this study, the 2-dimensional and bulk transport characteristics for p-type GaN films grown by MME on AlN buffer layers are investigated. Given that the electrical properties can be a composite of traditional valence band conduction, impurity band conduction, and 2-dimensional conduction, details on the electrical transport in these films are provided by: (a) modifying the III/V ratio to enhance bulk effects at the expense of 2D effects, and (b) varying the sample thickness to extract 2D sheet charge contribution resulting from polarization-induced effects at the hetero-interface. The optical properties of the highly Mg-doped p-GaN and p-AlGaN films grown by MME are characterized in order to investigate the effects of heavy Mg doping and correlations with the electrical properties. Finally, optoelectronic device structures are grown to explore

the viability of MME as a device-capable growth technique as well as the performance of these highly Mg-doped films in device structures.

3.2 Experimental Setup

All films in this study, unless otherwise noted, were grown by Metal-Modulated Epitaxy in a Riber 32 MBE system with a base pressure of approximately $8x10^{-11}$ Torr. Substrates were either 1×1 cm n-type or semi-insulating MOCVD-grown GaN on sapphire templates, or 1×1 cm MOCVD-grown AlN on sapphire templates. All substrates were single-side polished and a 2 μm-thick tantalum coating was sputtered on the backside for uniform heating during growth. The substrates were cleaned using a 4:1 solution of H_2SO_4:H_2O_2, then rinsed thoroughly with DI water. The beaker was etched for 1 minute in dilute HF, then the substrates were cleaned again using a second 4:1 solution of H_2SO_4:H_2O_2 before being loaded into an introductory vacuum chamber on an indium-free molybdenum block. The substrates were outgassed in the introductory chamber for 20 minutes at 150°C and then outgassed again for 10 minutes in the growth chamber at 600-800°C. For all film growths, nitrogen was supplied by a Veeco UNI-Bulb RF plasma source with 350W of RF power and 1.3 sccm N_2 flow, resulting in a chamber pressure of approximately $1.2x10^{-5}$ Torr. The nitrogen-limited growth rate for this plasma condition was approximately 700 nm/hr. Magnesium was delivered by a Veeco corrosive valved cracker. Prior to initial use, the Mg was vacuum re-melted to purify the source. With the valve closed, the bulk zone of the cracker was heated in stages to 670°C intermittently cracking the valve open to 10 mils for approximately 2

seconds to allow hydrogen gas dissolved in the Mg to escape. Given the 1 to 10 Torr vapor pressure of Mg at these temperatures, care was taken to prevent long valve openings which can quickly coat the entire chamber with Mg. This process was repeated ~20-40 times until a significant reduction in the hydrogen background level was observed by a residual gas analyzer. During growth, the Mg valved source was operated at a bulk temperature of 295°C, a tip temperature of 900°C, and a valve opening of 240 mils for all GaN:Mg films.[93, 116] Gallium was supplied by either a standard effusion cell or a Veeco SUMO® cell with metal-rich fluxes ranging from $3x10^{-7}$ Torr to $7x10^{-7}$ Torr, resulting in III/V ratios of approximately 1.2 to 2.8, respectively. Standard effusion cells were used for indium and silicon, while a cold-lip cell was used for aluminum. For the GaN template substrates, a 120 nm-thick AlN buffer layer was grown by MME with a shutter cycle of 10s open/10s closed at a III/V ratio of approximately 1.8 and a substrate temperature of 700°C.[80, 117] For the AlN template substrates, a 50 nm-thick AlN buffer was grown using the same conditions except the substrate temperature was 800°C. The p-type GaN:Mg films were grown at 600°C with varied III/V ratios and thicknesses, but the shuttering scheme was the same 5s open/10s closed with Ga and Mg shuttered simultaneously.

RHEED was used to characterize the films *in situ* and post-growth analysis was performed by x-ray diffraction (XRD) using a Philips X'Pert Pro MRD. A Veeco Dimension 3100 atomic force microscope (AFM) was used in tapping mode to determine surface morphology after growth. The electrical properties of the films were determined by Hall effect measurements using either a 0.3T fixed magnet at room temperature or a custom temperature-dependent Hall effect system.[105] Traditional indium-dot contacts

were used unless otherwise noted, and the ohmic nature of the contact was verified by the linearity of the current-voltage curve for each sample. The temperature-dependent Hall effect system included a MMR Joule-Thomson thermal stage from 90K to 410K and a Walker Scientific 1.5T electromagnet with high-precision Keithley electronics and an algorithm defined by ASTM standard F76[118]. Photoluminescence (PL) spectroscopy was performed at room temperature using a Spex 1702 spectrometer with excitation from a 325 nm HeCd laser.

3.3 Surface Kinetics and Growth of p-GaN by MME

In order to explore the effect of growth conditions on the surface and electrical properties of these highly Mg-doped GaN films, several samples were grown using varied Ga flux for a thickness of 100 nm. The chosen fluxes were $3x10^{-7}$, $3.4x10^{-7}$, $5x10^{-7}$, and $7x10^{-7}$ Torr which resulted in III/V ratios of approximately 1.2, 1.4, 2.0, and 2.8, respectively, hereafter called samples A, B, C, and D. Given the 1:2 open:closed duty cycle used throughout this work, all of these III/V ratios represent high metal rich instantaneous fluxes during the shutter open phase but overall N-rich time average flux when the shutter closed cycle is considered. Above a III/V flux ratio of 3.0, not all the metal would be consumed in a single cycle, resulting in cycle-to-cycle droplet accumulation. Contrarily, the shutter cycles were kept constant at 5s open followed by 10s closed which resulted in a dry, adlayer-free surface at the end of each shutter period for all four flux conditions as confirmed by transient RHEED analysis.[82] The

corresponding RHEED transients and final RHEED patterns for all samples are shown in Figure 3.1.

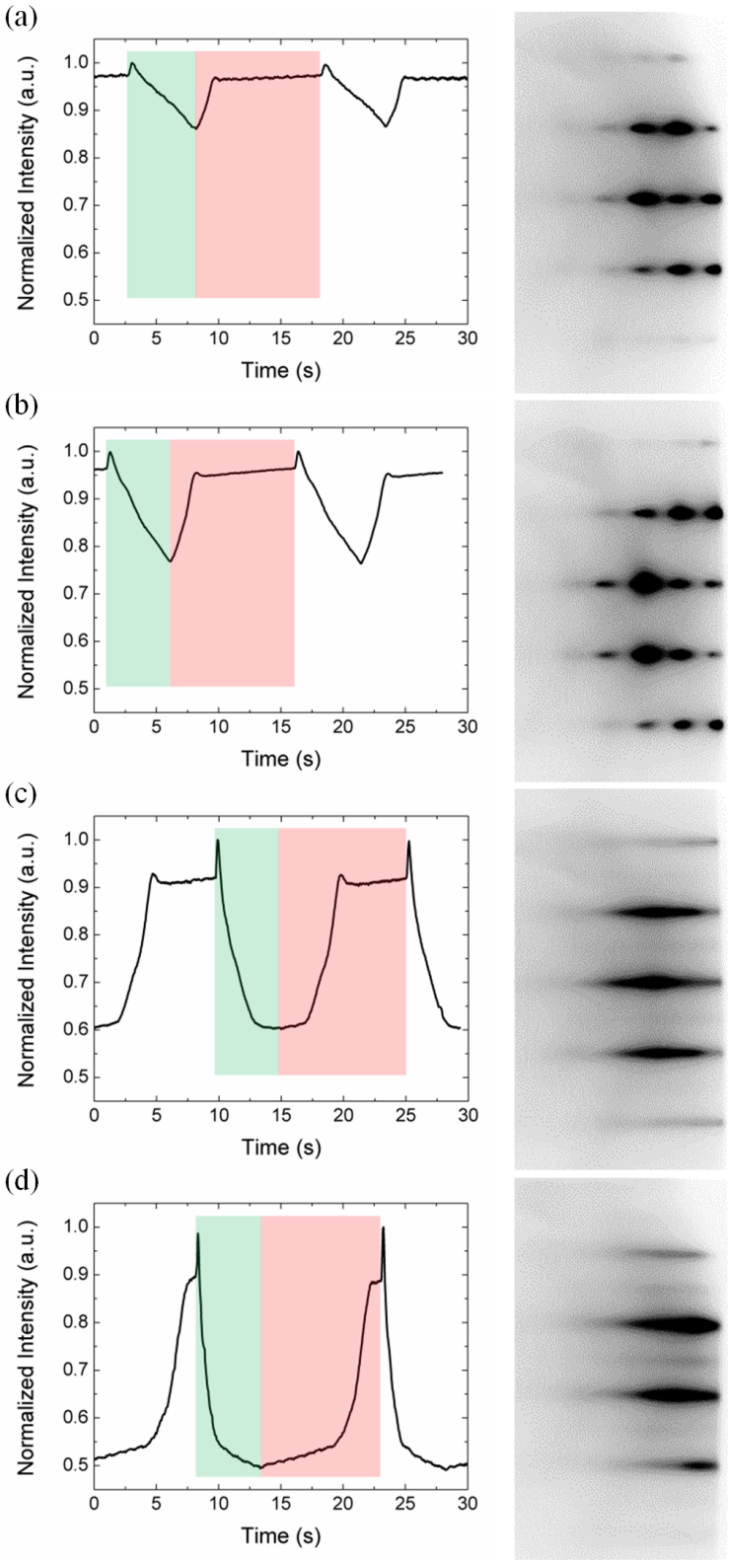

Figure 3.1: Transient RHEED intensities (left) and final RHEED patterns (right) for GaN:Mg with varied III/V ratio of (a) 1.2, (b) 1.4, (c) 2.0, and (d) 2.8. Shutter open is highlighted in green, shutter closed in red.

A clear trend in apparent roughness is visible as the pattern transitions from spotty to streaky with increasing III/V ratio. A mix of streaks and spots is present for sample A in Figure 3.1(a) with a III/V ratio of 1.2, as has been shown previously for similar growth conditions to be optimal for high hole concentration GaN.[83, 84] The RHEED transient shows a shallow downward slope upon shutter open which indicates slow accumulation of a Ga+Mg metal adlayer due to slightly metal-rich conditions. For sample B in Figure 3.1(b) with a III/V ratio of 1.4, the spots become more elongated indicating a transition to a streakier pattern associated with a somewhat smoother film. Compared to Figure 3.1(a), the RHEED transient for Figure 3.1(b) shows a sharper downward slope corresponding to faster build-up of the metal adlayer which reaches a lower relative intensity implying a more complete or thicker surface coverage of the final adlayer before closing the metal shutters. At a III/V ratio of 2.0 for sample C in Figure 3.1(c), the pattern is purely streaky with a weak 2×2 reconstruction indicating a smooth, Ga-polar surface.[119] The corresponding RHEED transient shows a rapid intensity drop upon shutter open which saturates indicating the onset of metal droplets, a signature that typically results in very smooth films using this growth technique.[82] The presence of metal droplets is also confirmed by the delay after shutter closing in the recovery of the RHEED transient intensity followed by a sharp increase to its initial value prior to shutter opening. Finally, for sample D in Figure 3.1(d) with a III/V ratio of 2.8 the final RHEED pattern is again purely streaky and a 2×2 reconstruction is clearly visible even at the growth temperature of 600°C. Similar to Figure 3.1(c), the RHEED intensity drops quickly after shutter open and reaches the droplet stage within 2-3 seconds, and when closing the metal shutters there is a long delay which indicates substantial droplet

accumulation before the intensity recovers to its starting value prior to shutter opening.

3.4 Temperature-Dependent Hall Effect with Varied III/V Ratio

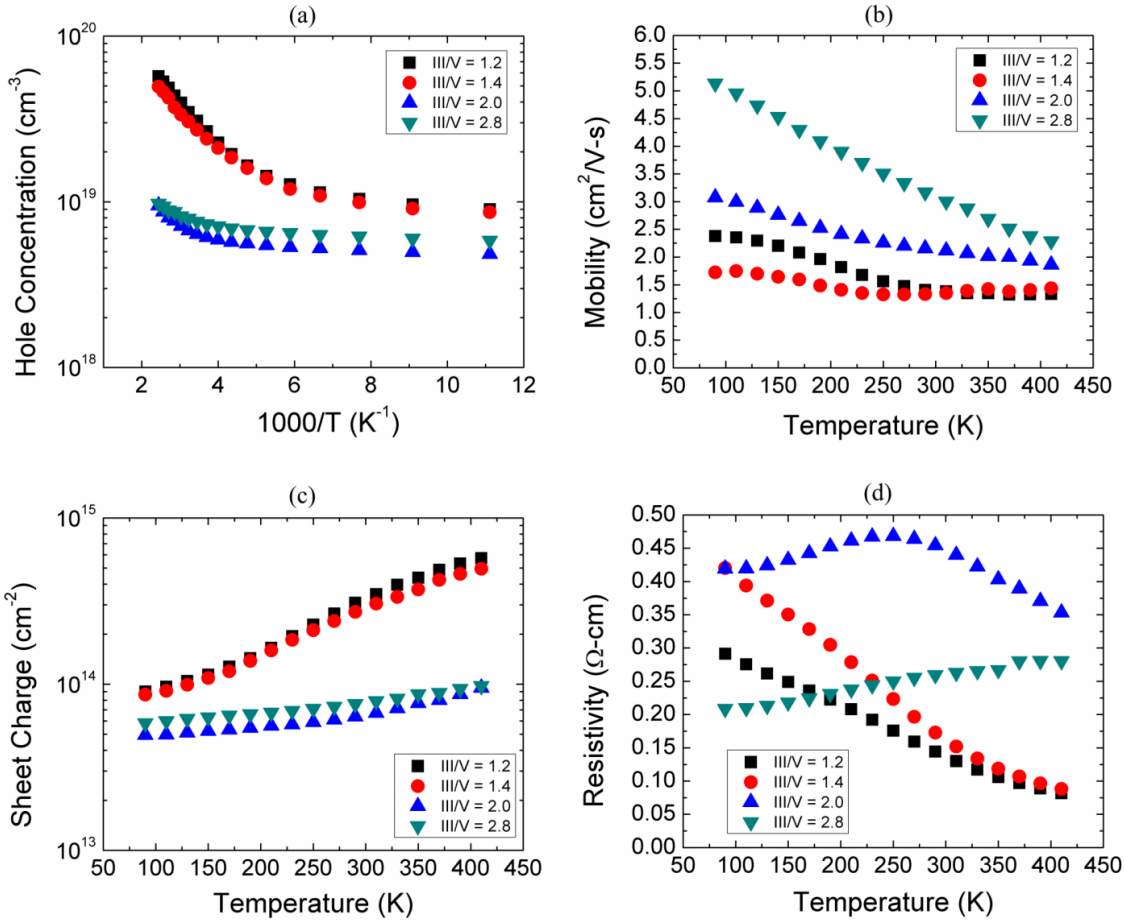

Figure 3.2: Temperature dependent (a) hole concentration (Arrhenius plot), (b) mobility, (c) sheet charge, and (d) resistivity for GaN:Mg films with varying III/V ratios.

After growth, the films were electrically characterized by temperature-dependent Hall effect, the results of which are shown in Figure 3.2. Unlike traditionally doped p-GaN which tends to freeze out the electrically active holes at cryogenic temperatures,[106-108] all four samples remained p-type throughout the measured temperature range.[54] As can be seen from Figure 3.2(a), the extraction of activation

energy from the high temperature linear region of the temperature-dependent hole concentration data results here in activation energies for samples A and B of 51 meV. Insufficiently high temperatures were available for extraction of the activation energies of samples C and D which showed minimal change in hole concentration across the measured temperature range.

As with the trends observed in the surface structure via RHEED, the samples show substantially different electrical characteristics for the different III/V ratios. While all four samples show increasing mobility at low temperatures in Figure 3.2(b), the samples with III/V ratio of 2.0 and 2.8 (samples C and D, respectively) have higher mobility at all temperatures. Moreover, the mobility of the lower flux samples with III/V ratio of 1.2 and 1.4 (samples A and B, respectively) appears to saturate near 100K at approximately 2.4 and 1.7 cm^2/V-s, respectively, while the mobilities for the higher flux samples continue to rise even at 90K. The temperature-dependent sheet charge in Figure 3.2(c) shows a similar pairing based on III/V ratio. Here, samples C and D show minimal temperature dependence of the sheet charge, decreasing by about 40% from 410K to 90K. However, samples A and B exhibit extremely high sheet charges, more than 4 times larger than samples C and D, on the order of $3x10^{14}$ cm^{-2} at room temperature. These lower III/V ratio films also have substantially different temperature-dependence compared to the high III/V ratio films, with sheet charges dropping by nearly 85% with decreasing temperature from 410K to 90K. Finally, the temperature-dependent resistivity in Figure 3.2(d) shows a flux-dependent transition that reflects the inverse product of the mobility and sheet charge data. In Figure 3.2(d), samples A and B have very low room-temperature resistivities of just 0.14 and 0.17 Ω-cm, respectively. However, both films A

and B show a monotonic increase in resistivity with decreasing temperature. Sample D, conversely, shows the opposite behavior with a monotonic decrease in resistivity with decreasing temperature. Finally, sample C shows a mixed behavior where the resistivity initially increases when the temperature drops from 350K to 250K, and then the resistivity decreases with lower temperature from 250K to 90K.

Together these trends give some insight into the electrical activity of the films for different III/V ratios. As has been shown previously, a lower III/V ratio balances crystalline defect formation with the proper conditions for optimal Mg incorporation and activation.[83, 84, 105] This results in a substantially higher total sheet charge as shown in Figure 3.2(c) for samples A and B, although the surface is rougher as demonstrated clearly by the RHEED in Figure 3.1(a-b). On the other hand, the high III/V ratio for samples C and D results in a much smoother surface due to the more metal-rich growth condition leading to improved adatom mobility. However, the resulting sheet charge is substantially reduced when the higher III/V ratio is used. This reduction in sheet charge can be a result of the diluted Mg arising from the higher Ga to Mg ratio and from a difference in sticking coefficients as expected from a change in metal coverage. For a fixed Mg flux, as is the case here, a higher Ga flux will result in a reduction in the net Mg concentration due to a higher Ga:Mg ratio. From sample A to sample D, the Ga:Mg ratio decreases by a maximum of approximately 2.3, while the overall room temperature sheet charge decreases by a factor of 4. As such, the reduction in sheet charge is not due solely to the changing Ga:Mg ratio, but must also come from other mechanisms. To further investigate the change in electrical properties, secondary ion mass spectrometry (SIMS) was performed externally on all four samples by Evans Analytical Group. Background

impurity concentrations were reasonably consistent with oxygen concentrations of 3-6x10^{17} cm^{-3}, carbon concentrations of 2-5x10^{17} cm^{-3}, and hydrogen concentrations of 1-3x10^{18} cm^{-3}. The Mg concentration for samples A and B were approximately similar at 1.3x10^{20} cm^{-3} and 1.2x10^{20} cm^{-3} respectively, while the Mg concentrations for samples C and D were nearly identical at 2.3x10^{19} cm^{-3}. The Mg concentration for samples A and B is in line with previous p-type films grown by MME under similar conditions. However, the more than 5x reduction in Mg for samples C and D is unexpected based solely on the III/V ratio changes which would point to a maximum 2.3x reduction in Mg concentration. It has been shown previously, at high temperatures under Ga-rich conditions and for a high fixed Mg flux, that an increase in Ga flux resulted in improved Mg incorporation.[72] Contrarily, this work at low temperature indicates that the Mg incorporation was inhibited by additional Ga flux. The explanation for this reduced Mg incorporation at high III/V rations could be due more to surface morphology and surface kinetics than simply III/V ratio. Specifically, for low III/V ratio the surface morphology quickly becomes roughened due to insufficient metal adlayer coverage. This roughening could enhance Mg incorporation due to additional surface area available for bonding and an increase in available step edges which enhance incorporation. Because the Mg-Nitrogen bond in the crystal is stronger than the Ga-Mg bond in the liquid adlayer, a faster consumption of the metal adlayer results in a lower probability of Mg desorption. A Ga-poor or moderately Ga-rich condition has been shown in theoretical calculations to result in the best Mg incorporation, which supports the results obtained in SIMS.[120] In samples C and D, with III/V ratios of 2.0 and 2.8, respectively, the very similar Mg concentrations point to some degree of saturation within the film independent of the

excess metal adlayer beyond some threshold coverage. The common feature of samples C and D during growth is the accumulation and consumption of metal droplets, while for samples A and B no such droplets are ever present due to the reduced III/V ratio. Thus, it is also possible that the change in Mg concentration could be related to the presence of metal droplets if the Mg incorporates more effectively in the metal bilayer and less efficiently in the excess droplets.

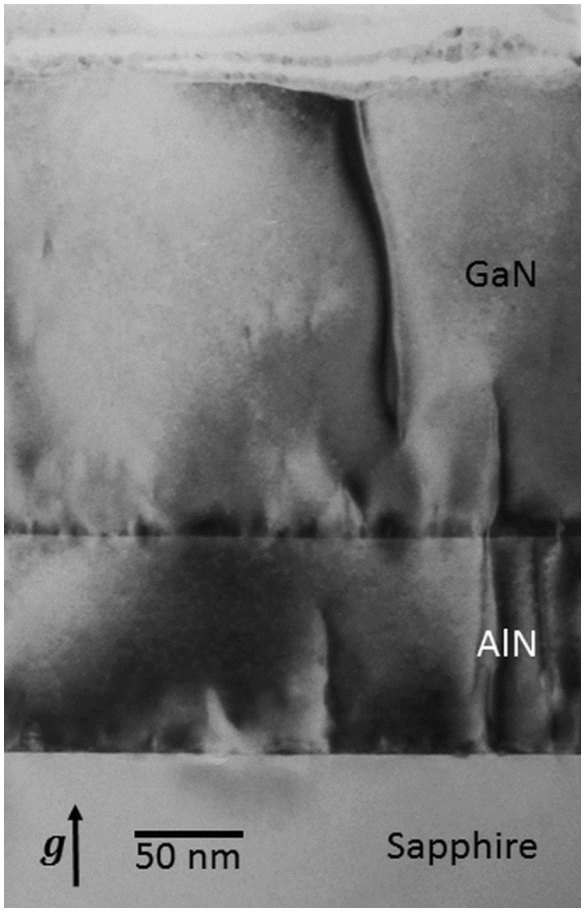

Figure 3.3: Cross-sectional TEM image for p-type GaN grown by MME with Mg concentration of 2.6×10^{20} cm^{-3} demonstrating no inversion domains or Mg precipitation. Diffraction contrast makes screw dislocations visible.

Shown in Figure 3.3 is a TEM cross-section taken on a separate film, grown under

similar conditions to sample A by MME, with a Mg concentration of approximately $2.6x10^{20}$ cm^{-3} determined by SIMS. Even with a Mg concentration approximately twice as large as that in samples A and B, the TEM for this film shows no Mg precipitation which has been seen previously and is a common problem for high Mg doping.[68, 69] In addition, there are no visible inversion domains which again points to the efficacy of MME as a growth technique for Mg-doped GaN with high Mg concentrations. This is dramatically different from higher temperature, steady state growth techniques which have been shown to precipitate Mg and subsequently form inversion domains for Mg concentrations above ~$5x10^{19}$ cm^{-3}.[68] There are several possible reasons why these features are not observed in MME including the rougher surfaces resulting from reduced III/V ratios which may provide ample additional surface sites for incorporation of the Mg. This increase in surface area can be estimated by the ratio of the surface area of an appropriately chosen hemi-ellipsoid compared to a plane of the same lateral area. This ratio is maximum at 2 for a hemisphere and is significantly smaller, 1.1 or less, for semi-ellipsoids with the average dimensions observed in our films, 1-2 nm root mean square (RMS) with average grain sizes of 50-100 nm. Thus, it is unlikely the increased incorporation of Mg in GaN as demonstrated by MME is due solely to geometry effects. More likely, it may be possible to exceed the solubility of Mg in GaN by kinetically "trapping" Mg into the lattice at low temperature and high growth rates, thus resulting in meta-stable super-saturation of acceptors. Evidence in support of this concept is found in meta-stability during annealing studies of MME p-GaN,[121] as well as low temperature rapidly-grown traditional plasma MBE without inversion domains.[75, 103, 109]

Typically, the reduction in total sheet charge at lower temperatures is

characteristic of carrier freeze-out in bulk films which can be seen in Figure 3.2 for samples A and B with lower III/V ratio. For samples C and D, such a drop in sheet charge is dramatically reduced, changing by a factor of approximately 1.5 from 350K to 90K, compared to a factor of approximately 4.5 for samples A and B. However, all four films do show an apparent saturation in the sheet charge at low temperature which is on the order of 8-9x10^{13} cm^{-2} for samples A and B, and 4-5x10^{13} cm^{-2} for samples C and D. A similar weak temperature-dependence of the sheet charge combined with saturation at low temperature has been demonstrated in III-nitride heterostructures which can result in a 2-dimensional hole gas (2DHG).[122, 123] This phenomenon comes about from field ionization due to spontaneous and piezoelectric polarization at hetero-interfaces leading to substantial band-bending and large electric fields which are relatively unchanged with varying temperature. Given that these p-type GaN films are grown on AlN which results in upward band bending and hole accumulation at the p-GaN/AlN interface, such a 2DHG effect is likely a contributing factor here. Simple simulations (SiLENSe, STR Group Inc.) of this polarization at the hetero-interface point to a narrow hole accumulation thickness of just 5-7 nm due to high acceptor concentrations which quickly compensate the electric field.

2DHG structures have been demonstrated and shown to exhibit limited carrier freeze-out characteristics and improved hole mobility.[124-134] Ambacher *et al.* described in detail the calculations of piezoelectric and spontaneous polarization for AlGaN/GaN interfaces.[135] Repeating the calculation for fully strained GaN on relaxed AlN, the total polarization-induced sheet charge would be approximately 5.3x10^{13} cm^{-2}. For the fully relaxed case, it is expected that a GaN/AlN interface should result in a sheet

charge density of approximately $3.25x10^{13}$ cm^{-2} which arises only from spontaneous polarization. Given that the critical thickness for GaN on AlN is about 3 nm,[136, 137] and the p-type films for samples A-D are all nominally 100 nm thick, the p-GaN films should all be almost fully relaxed with only small amounts of residual compressive strain. As such, the polarization sheet charge for all four samples is expected to be on the lower end of the $3.25\text{-}5.3x10^{13}$ cm^{-2} range. This 2DHG density accounts for a majority of the total sheet charge at low temperature for samples C and D, but 35-40% of the total low temperature sheet charge for samples A and B grown with lower III/V ratio. At room temperature, these 2DHG contributions shift to 10%, 12%, 50% and 42% for samples A, B, C and D, respectively. By subtracting out the approximate 2DHG contribution to the total sheet charge for samples A and B, the estimated sheet charge density at 90K is still $5.5x10^{13}$ cm^{-2} due to non-interfacial layers, which translates to a total bulk hole concentration of $5.5x10^{18}$ cm^{-3} at cryogenic temperatures for the 100 nm thick films. Clearly, the lack of carrier freeze-out of this "bulk" charge contribution suggests a relatively shallow acceptor as will be demonstrated from optical measurements.

At room temperature, where more carriers are thermally activated in the bulk, the 2DHG is a very minor contributor to the overall sheet charge, and the bulk hole concentration after subtracting the 2DHG is estimated at $2.5x10^{19}$ cm^{-3}. Typically, p-GaN films grown by traditional MBE or MOCVD exhibit hole concentrations on the order of 10^{16} cm^{-3} at low temperatures and mid-10^{17} cm^{-3} at room temperature for films with Mg concentrations of $1\text{-}5x10^{19}$ cm^{-3}. Samples A and B with low III/V ratio and high Mg doping concentrations of $\sim 1.2x10^{20}$ cm^{-3} show bulk hole concentrations 1 to 2 orders of magnitude higher than traditional p-type GaN films across the temperature range.

Moreover, the high sheet charge density at cryogenic temperatures cannot be explained solely by the presence of a 2DHG in samples A and B, supporting the previous theory that impurity band conduction, which also does not freeze out at low temperatures, plays a dominant role in the carrier transport.[105]

The temperature-dependent resistivity also reflects the presence of multiple transport mechanisms for each film. For samples A and B, the resistivity is extremely low at room temperature, less than 0.2 Ω-cm, but rises with lower temperature which follows thermal ionization typically seen in traditional p-type GaN films, but with substantially reduced activation energies of ~51 meV. Nonetheless, the resistivity remains low at less than 0.5 Ω-cm even at 90K. For sample D, the resistivity follows the opposite trend and decreases with decreasing temperature. This resistivity vs. temperature trend seen is commonly seen in HEMTs and it arises from a reduction in phonon scattering leading to higher mobility at low temperatures while the carrier concentration remains relatively unchanged. So while samples A and B have resistivities that are strongly affected by bulk transport, sample D has a resistivity that appears to be strongly influenced by 2-dimensional transport. Finally, sample C shows a clearly mixed behavior where the resistivity initially rises slightly when the temperature is reduced from 350K to 250K, then the resistivity falls below 250K which points to a small contribution from bulk transport and a weaker but still present influence from a 2DHG.[18, 74, 75, 103, 109]

3.5 Thickness-Dependent Trends

In order to further explore 2-dimensional transport in these highly Mg-doped GaN films on AlN, an additional sample set was grown with varying thickness from 28 nm to 440 nm using a III/V ratio of ~1.2. These samples with different thickness were

characterized by Hall effect measurements. Shown in Figure 3.4 is the thickness-dependent sheet charge at room temperature.

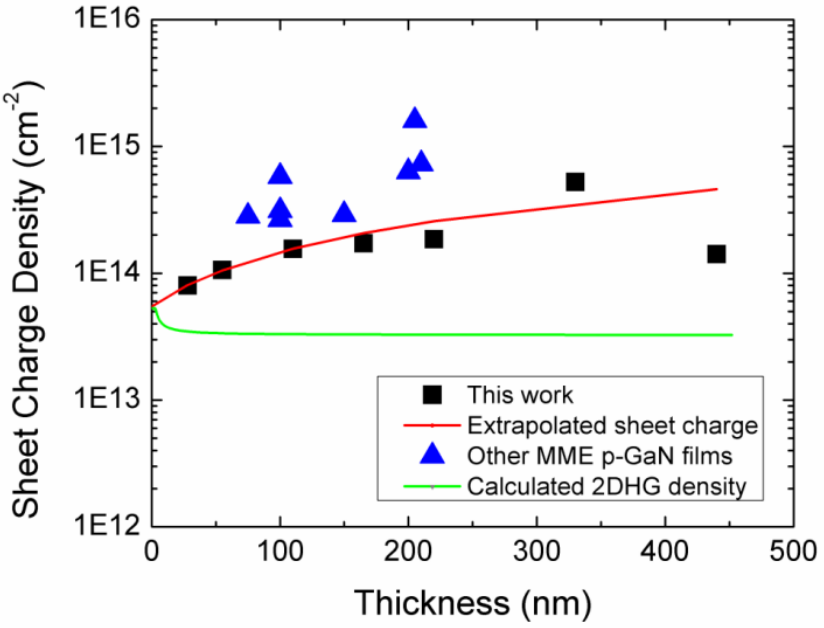

Figure 3.4: Sheet charge density for p-type GaN films grown in this study (black squares) with varied thickness from 28 nm to 440 nm, other hole-concentration-optimized films grown by MME (blue triangles), and a linear fit of the low-thickness data to estimate the 2DHG density when extrapolated to zero thickness (red line). The green line is the calculated 2DHG density as a function of a thickness to show the interfacial contribution.

From Figure 3.4 it is clear that at low thickness (110 nm and less) there is a linear increase in the total sheet charge with increasing thickness as expected, denoted by the red line. The low-thickness trend is useful as it allows for an experimental approximation of the 2DHG density and extrapolating the linear fit back to zero thickness results in a y-intercept of approximately 5.5×10^{13} cm^{-2}, which is very close to the 5.3×10^{13} cm^{-2} sheet charge calculated for fully strained GaN on relaxed AlN. As the p-type GaN film thickness on AlN increases, the film relaxes further and strain is reduced, thus the total polarization sheet charge decreases due to the reduction of the piezoelectric polarization

contribution. As shown in Figure 3.4, the calculated 2DHG density of ~3.25×10^{13} cm^{-3} represents only a minority contribution to the total sheet charge of 1-2×10^{14} cm^{-2} for the 55 and 110 nm films, thicknesses commonly used in III-Nitride devices. After subtracting out the estimated contribution from the 2DHG, the bulk hole concentrations in both the 55 and 110 nm thick films are approximately the same, 1.1×10^{19} cm^{-3} at room temperature. This hole concentration is 1 to 2 orders of magnitude higher than traditional p-GaN films. Moreover, the resistivity of the thinnest p-GaN film of 28 nm exhibited an extremely low room-temperature resistivity of just 0.054 Ω-cm with a mobility of 4 $cm^2/V\text{-}s$.

For low III/V flux ratio MME films the surface roughness increases with thickness. Thus, for thicker MME-grown p-GaN films (>150 nm), where defect density and surface roughness are higher, the results deviate from the trend line in Figure 3.4 and become less predictable. Shown in Figure 3.5 are the 1×1 μm AFM images from the 55 nm and 440 nm thick films which demonstrate the surface roughening as these highly Mg-doped are grown thicker. The 55 nm sample shows a grainy surface morphology which is typical for these MME growth conditions with lower III/V ratio, and has a smooth RMS roughness of just 0.67 nm. For the 440 nm film, the RMS roughness increases to 1.61 nm and the underlying pits become more pronounced due to insufficient lateral growth. From Figure 3.5 it is clear that the growth conditions which give the highest hole concentrations are not optimal for good crystal quality, as has been shown previously.[105] Nonetheless, the MME-grown highly Mg-doped films still demonstrate reasonable surface roughness from 0.5 to 2 nm RMS, especially when considering the Mg concentrations in excess of 10^{20} cm^{-3}.

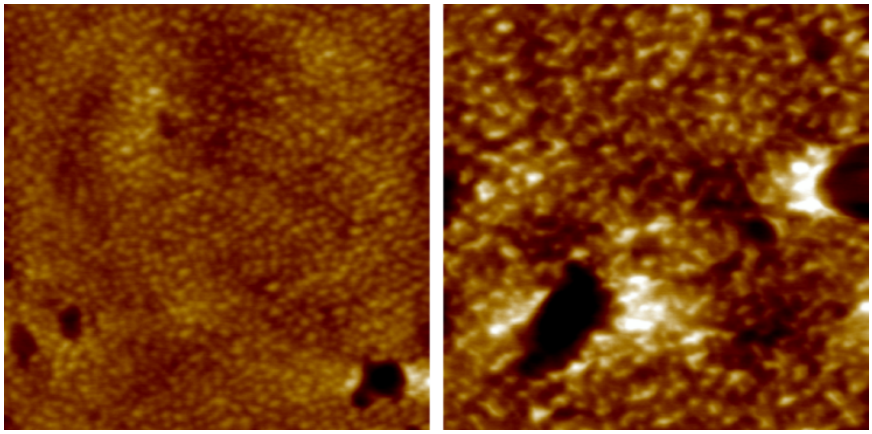

Figure 3.5: 1×1 μm AFM images for 50 nm thick (left) and 440 nm thick (right) highly Mg-doped p-GaN films grown on AlN buffers. RMS roughness is 0.67 nm for the 55 nm film and 1.61 nm for the 440 nm film. Height scale = 10 nm.

3.6 Optical and Electrical Characterization of P-Type AlGaN

With the demonstration of p-type GaN with electrical properties and surface roughness desirable for device applications, an additional sample set was grown in order to determine the feasibility of p-type AlGaN grown by MME. In this case, AlN templates grown by MOCVD on c-plane sapphire were used as the substrate, with a nominal AlN thickness of 775 nm. The substrates were cleaned and loaded in the manner described above, and then outgassed in the growth chamber at 800°C. A 50 nm AlN layer was grown by MME to bury surface oxidation and resulted in a streaky RHEED pattern with a 2×2 reconstruction (not shown) indicating smooth, Al-polar growth. The substrate temperature was then lowered to 600-650°C for the growth of p-type GaN and p-type AlGaN. All p-type films in this series were nominally 100 nm thick. A calibration growth of p-type GaN was initially performed as a baseline, which resulted in a room temperature sheet charge of 5.8×10^{14} cm^{-2}, hole concentration of 5.8×10^{19} cm^{-3},

mobility of 0.49 cm^2/V-s, and resistivity of 0.22 Ω-cm.

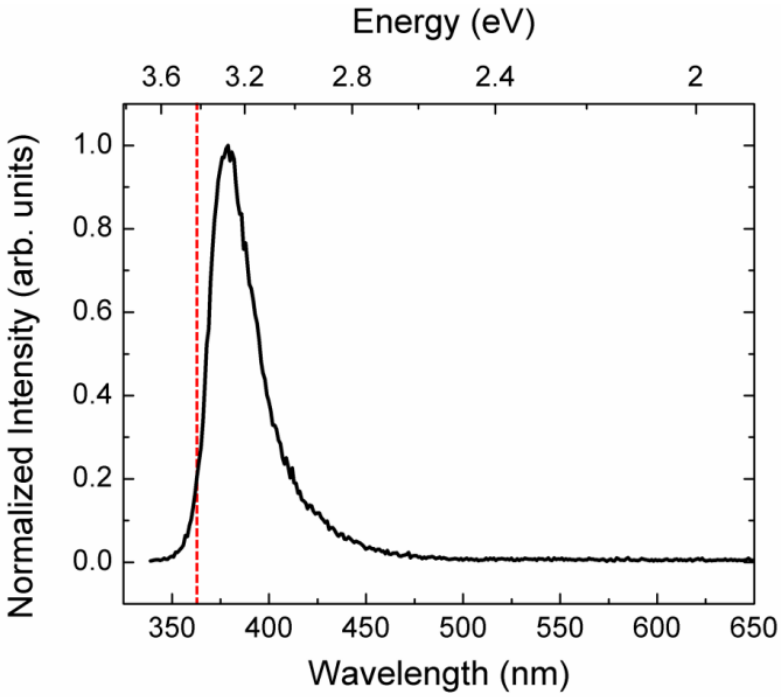

Figure 3.6: Room-temperature PL spectrum of 100 nm thick highly Mg-doped GaN on AlN template substrate with peak emission wavelength of 378 nm and FWHM of 240 meV with no detectable yellow luminescence.

Photoluminescence spectroscopy was also performed on the p-type GaN on AlN template and the resulting room-temperature spectrum is shown in Figure 3.6. In previous samples, photoluminescence was not performed due to the thick, underlying semi-insulating GaN template which would overwhelm the luminescence from the thinner p-type layer. In Figure 3.6, there is no observable yellow or other deep level luminescence and the PL peak energy occurs at approximately 378 nm which is in excellent agreement with PL data from MME-grown highly p-type GaN films and will be published later. The peak exhibits a broad full-width at half maximum (FWHM) of approximately 240 meV which supports the previously discussed acceptor band formation.[105] Finally, the high energy tail of the peak extends into the valence band

edge as marked by the dotted red line at the room temperature GaN bandgap of 3.42 eV. These observations support the existence of broad acceptor band rather than the traditional isolated acceptor energy as is seen for lighter-doped p-type GaN films. The splitting of the acceptor energy into a band results in a broader range of transition energies and thus a wider FWHM of the PL signal.

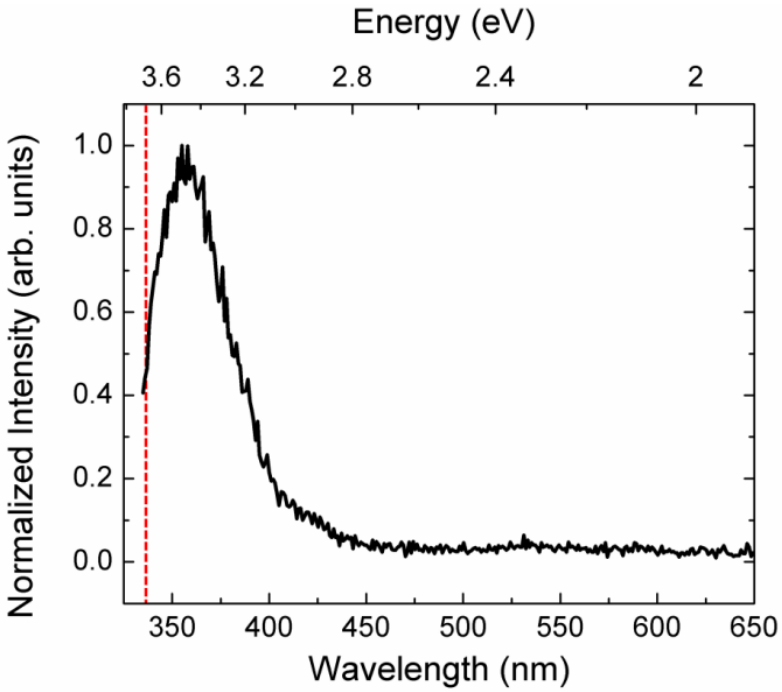

Figure 3.7: Room-temperature PL spectrum from p-type AlGaN with 11% Al fraction. Peak emission wavelength is 358 nm with a FWHM of 440 meV. High energy tail intercepts the valence band marked by the red dotted line.

A p-type AlGaN film with 11% Al fraction was grown at 620°C with nominally the same III/V ratio of 1.2, as measured by Z-number normalized fluxes, as for p-type GaN, but with the Al fraction selected by adjusting the Al and Ga fluxes. In order to extract the degree of relaxation as well as the lattice parameters, a reciprocal space map (RSM) was performed about the (105) reflection for the AlN and AlGaN peaks (not

shown). The Al content was determined to be 11% with a basal lattice spacing *a* of 0.3176 nm exhibiting 92.5% relaxation, while the FWHM of the (002) ω-scan for the p-type AlGaN peak was 316 arcsec. Hall effect measurements were also performed and the room-temperature sheet charge for the 100 nm thick film was $2.7x10^{14}$ cm^{-2}, with a mobility of 0.8 cm^2/V-s and resistivity of 0.3 Ω-cm. From the same polarization equations after Ambacher *et al,*[135] the resultant total sheet charge density from this p-$Al_{0.11}Ga_{0.89}N$ on AlN is expected to be approximately $3.0x10^{13}$ cm^{-2} which means that nearly 90% of the total measured sheet charge of $2.7x10^{14}$ cm^{-2} is in the bulk rather than accumulated in a 2DHG at the interface. In volumetric terms, the hole concentration attributed only to the bulk is still $2.4x10^{19}$ cm^{-3} after subtracting out the calculated 2DHG contribution. The photoluminescence spectrum shown in Figure 3.7 also shows the same character as seen for the p-GaN. In this case the peak wavelength is 358 nm and the FWHM broadens to 440 meV, while the high-energy tail has a clear crossing of the valence band edge which further supports the presence of an acceptor band even in this p-type AlGaN film. A second p-type AlGaN film was also grown, but with a higher substrate temperature of 640°C and Al fraction of 27%. The (105) RSM (not shown) revealed the Al content of 27% which exhibits 72.2% relaxation with lattice spacing *a* of 0.3155 nm, while the FWHM of the (002) ω-scan was slightly broader at 445 arcsec. Due to the limitations of the 325 nm HeCd laser used for excitation, no PL could be acquired for this film. This higher Al-fraction p-AlGaN film maintains a high sheet charge density of $2.6x10^{14}$ but exhibits a lower mobility of just 0.2 cm^2/V-s, resulting in an increased resistivity 1.2 Ω-cm. Nonetheless, 1.2 Ω-cm $Al_{0.27}Ga_{0.73}N$ is a substantial improvement over many traditional p-type AlGaN films which often exceed 10 Ω-cm

.[138-140] The polarization-related sheet charge contribution for this p-$Al_{0.27}Ga_{0.73}N$ film is calculated to be $2.76x10^{13}$ cm^{-2} which again confirms that the overwhelming majority of the measured sheet charge of $2.6x10^{14}$ cm^{-2} comes from the bulk film rather than a 2DHG, resulting in a bulk hole concentration of $2.3x10^{19}$ cm^{-3}.

3.7 Optoelectronic Devices with Highly P-Type Films Using MME

In a final pair of growths to explore the viability of MME for device applications, a p-i-n diode and a multi-quantum well (MQW) LED were grown. The MQW LED was grown on a 4 μm MOCVD-grown n-type Si-doped GaN template with electron concentration of approximately $3x10^{18}$ cm^{-3}. An initial regrowth of 200 nm of Si-doped n-type GaN was grown by MME at 600°C with a III/V ratio of approximately 1.8 and a shutter cycle of 10s open / 10s closed. Next, an unintentionally doped (UID) 3-period InGaN/GaN MQW active region was grown at a substrate temperature of 470°C. The quantum wells consisted of 2 nm InGaN with an indium fraction of 13%, while the barriers were 10 nm GaN. The wells were grown at a III/V ratio of 0.9 without shuttering, while the barriers were grown with a III/V ratio of 1.8 and shuttered 10s open / 10s closed to promote smooth interfaces. After the final barrier, the growth was halted and the substrate temperature was increased to 610°C, after which a 20 nm p-AlGaN electron-blocking layer (EBL) was grown with 10% Al fraction, followed by 100 nm p-GaN grown at 600°C. The III/V ratio during the EBL and p-GaN growths was maintained at 1.2 with a shutter cycle of 5s open / 10s closed. The vertical devices were then fabricated using traditional optical lithography and the mesa structure was formed via inductively coupled plasma (ICP) etching with a $Ar/Cl_2/BCl_3$ chemistry. Next, the n-

type contacts were deposited by electron beam evaporation and consisted of a Ti/Al/Ti/Au metal stack with thickness of 30/100/30/30 nm. Finally, the p-type contact of 30/30 nm of Ni/Au was then deposited. The as-deposited contacts showed ohmic behavior as measured on separate transfer length method (TLM) patterns for both n- and p-type contacts and no anneals were performed either before or after the fabrication process. The lack of need for thermal anneal for contacts is a unique feature of these devices. While previous studies have shown these highly p-type films to be more sensitive to annealing,[121] a more detailed study of contact resistance and contact annealing will be published separately. In addition, no further passivation or device optimization was performed. The fabricated device was tested using a Keithley 2410 SourceMeter^{TM}, and the I-V curve for the simple p-i-n diode is shown in Figure 3.8. The MQW LED demonstrates a series resistance of 10 Ω with a high shunt resistance of approximately 470 kΩ. A sharp turn-on is seen at approximately 3.3 V and the forward voltage is 3.95 V at 20 mA. The device exhibited violet-blue visible luminescence, confirmed by the electroluminescence (EL) spectrum (not shown) which shows a peak emission at approximately 425 nm. For a final test the device was then submerged in liquid nitrogen and still showed substantial luminescence even at just 77K (inset, Figure 3.8).

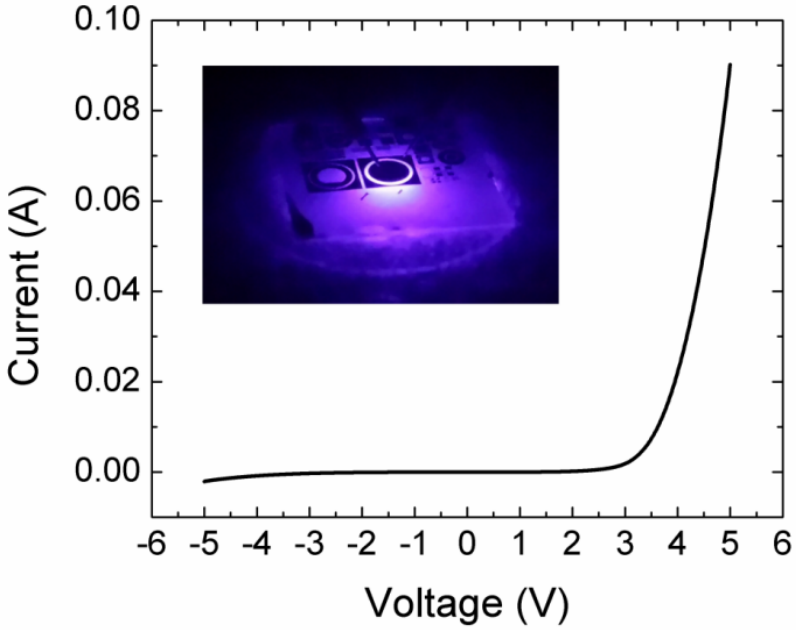

Figure 3.8: I-V curve of fabricated MQW LED showing a turn-on voltage of approximately 3.3 V and a forward voltage of 3.95 V at 20 mA. (Inset) Photograph of MQW LED luminescence while submerged in liquid nitrogen.

For the p-i-n diode all layers were grown at 600°C and the same n-type GaN template was used as the substrate. Following the same cleaning and loading procedure outlined previously, the film was further outgassed in the growth chamber at 600°C for 10 minutes. An initial regrowth of 200 nm of Si-doped GaN with an electron concentration of approximately $5x10^{18}$ cm^{-3} was first performed, followed by the i-region growth which consisted of a 20 nm thick unintentionally doped GaN layer. For both the n-type regrowth and i-region, the III/V ratio was 1.8 with a shutter cycle of 10s open / 10s closed. The p-type layer was grown with a III/V ratio of 1.2 and a shutter cycle of 5s open / 10s closed for a thickness of approximately 100 nm. The devices were fabricated using the same process as mentioned previously. Because this device was entirely GaN with no indium or aluminum bearing alloys, no polarization effects were present.

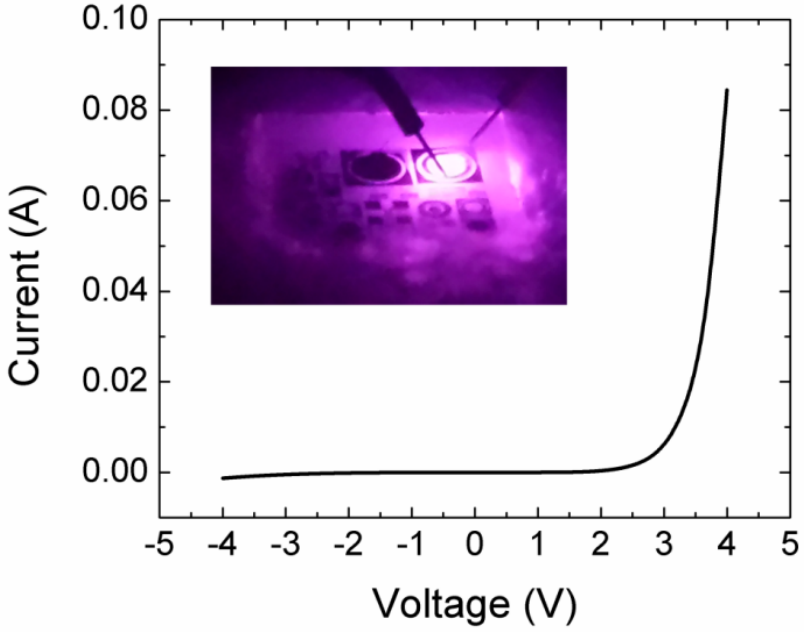

Figure 3.9: I-V curve of p-i-n diode grown by MME with turn-on voltage of approximately 3V and forward voltage of 3.45 V at 20 mA. (Inset) Photograph of p-i-n diode exhibiting luminescence while submerged in liquid nitrogen.

As shown in Figure 3.9, the diode exhibits a sharp turn-on at approximately 3 V and the forward voltage is 3.45 V at 20 mA. The series resistance extracted from the I-V curve is 6 Ω while the shunt resistance is approximately 350 kΩ. The diode at room temperature showed some weak visible luminescence so the electroluminescence (EL) spectrum was also measured and is shown in Figure 3.10. The EL spectrum shows UV-dominated emission centered at approximately 381 nm which is in agreement with the PL from MME-grown highly p-type GaN as shown previously in Figure 3.6. Thus, it is likely that the source of the UV luminescence is recombination within the p-type region. In the EL spectrum in Figure 3.10, a rise in the visible luminescence beginning at approximately 480 nm is seen. Also shown in Figure 3.10 is a comparison of the diode EL spectrum compared to the PL spectrum of the underlying MOCVD-grown GaN

template. Given that the rise in visible luminescence of the diode coincides with the onset of the yellow luminescence band of the GaN template, it is likely that the visible EL of the diode is due to hole injection and recombination in the n-type region. Although an additional 200 nm n-type layer was regrown on the underlying template, no yellow luminescence is typically seen in Si-doped or unintentionally-doped GaN films grown by MME.[92] Thus, the rise in visible luminescence is more specifically attributable to hole injection and diffusion more than 200 nm into the n-type region, penetrating through the regrown layer and into the template. Finally, the device was submerged in liquid nitrogen and showed strong luminescence even at 77K (inset, Figure 3.9).

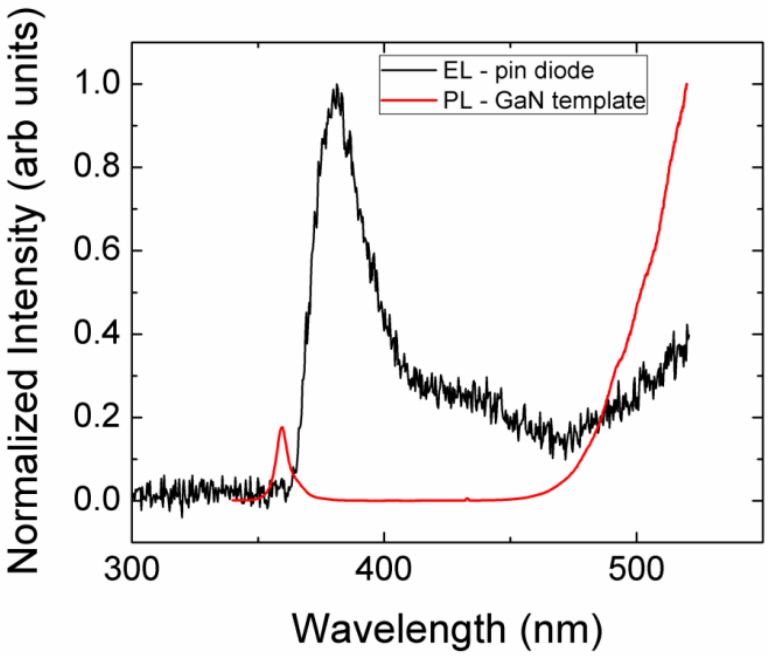

Figure 3.10: Electroluminescence spectrum of p-i-n diode grown by MME (black), with photoluminescence spectrum of the underlying n-type GaN template for comparison (red).

3.8 Conclusions

In this work, several transport mechanisms have been demonstrated in highly Mg-doped GaN grown by MME on AlN buffer layers using temperature-dependent Hall effect and photoluminescence. Films grown with high III/V ratio greater than 1.5 show significant contributions from 2D-transport which arises from a polarization-induced 2DHG formed at the p-GaN/AlN interface. However, for films grown with lower III/V ratio less than 1.5 the temperature-dependent data suggest transport dominated by bulk and impurity band conduction. These low III/V ratio films exhibit some traditional carrier freeze-out at cryogenic temperatures but still maintain a high charge density which cannot be attributed solely to a 2DHG, further supporting impurity band conduction as a major contributing transport mechanism. An impurity band is also evident from the PL spectra of p-GaN and p-$Al_{0.11}Ga_{0.89}N$ films which show broad FWHM and a high energy tail which clearly intercepts the valence band edge, both of which are consistent with the acceptor energy splitting into a band as doping is increased. For a thin 28 nm MME-grown p-GaN film a resistivity of 0.054 Ω-cm has been achieved by exploiting the combined transport mechanisms. P-type AlGaN has also been demonstrated with carrier concentrations greater than 10^{19} cm^{-3} for 100 nm thick films with Al fraction of 11% and 27% with resistivity of 0.3 and 1.2 Ω-cm, respectively. Finally, a MQW LED and p-i-n diode were fabricated using films grown by MME which exhibited clearly rectifying behavior with sharp turn-on at 3 V and 3.4 V with series resistances of 6 Ω and 10 Ω, respectively and did not require post metallization annealing. The LED exhibited room-temperature violet-blue EL centered at 425 nm while the p-i-n diode had ultraviolet dominated EL centered at 381 nm, and both devices demonstrated substantial EL even

while submerged in liquid nitrogen at 77K. The electrical characteristics of the devices confirm not only the strongly p-type nature of the MME-grown p-GaN but also the viability of MME as a technique for device growth.

CHAPTER 4: CONTROL OF ION CONTENT AND NITROGEN SPECIES USING A MIXED CHEMISTRY PLASMA FOR GaN GROWN AT EXTREMELY HIGH GROWTH RATES >9μm/HOUR BY PLASMA-ASSISTED MOLECULAR BEAM EPITAXY

4.1 Introduction

Group III-nitride semiconductors have seen enormous commercial growth in recent years for solid state lighting and power electronics. While the overwhelming majority of light emitting diodes (LEDs) are grown by metalorganic chemical vapor deposition (MOCVD), molecular beam epitaxy (MBE) has seen success in the power electronics market for the growth of high electron mobility transistors (HEMTs). Plasma-assisted MBE (PAMBE) typically uses a radio frequency (RF) plasma to generate reactive nitrogen species from inert nitrogen gas. PAMBE using an RF plasma has been shown to result in higher growth rates and improved surface morphology compared to other plasma techniques owing to lower ion content and reduced surface damage during growth.[141-143] Some PAMBE reports have shown growth rates for GaN higher than 1 μm/hour,[26, 144] and a very recent publication has reported growth rates as high as 2.65 μm/hour.[145]

Nonetheless, PAMBE is typically performed at growth rates on the order of 0.1 to 1 μm/hour,[110, 146] substantially lower than the growth rates typically used in MOCVD growth of GaN which commonly exceed 1-3 μm/hour.[147-150] These relatively low growth rates limit the applicability of PAMBE for many device structures which require thick buffer layers to reduce defect densities resulting from heteroepitaxy. Although the

ultra clean environment of MBE can be beneficial for the thick, undoped drift regions of p-i-n rectifiers, the slow growth rates still preclude the use of MBE for such devices. Finally, if III-nitrides, with their tunable band gap and strong light absorption,[5] are ever to become viable for solar applications, thick indium-bearing layers must be demonstrated in order to reduce defect densities. Such layers with high indium mole fractions are impractical in MOCVD due to the low temperature requirements for growing indium bearing alloys, while high temperatures are required for cracking ammonia. The result for most MOCVD growth of InGaN is very low growth rates and highly inefficient precursor usage.[151, 152] Contrarily, these high indium composition alloys are dramatically more suitable for PAMBE where substrate temperatures can be reduced in order to facilitate proper indium incorporation and no ammonia cracking is required. If rapid growth of indium-bearing layers can be achieved, then the potential of III-nitrides for photovoltaics improves dramatically.

In this study, we report on extremely high growth rates in PAMBE growth of GaN while maintaining a smooth surface microstructure. With added pumping capacity and a minor modification to the plasma source, a broad range of growth rates can be achieved, while a mixed chemistry plasma shows a further enhancement of the growth rate. Suppression of ion content is achieved by higher plasma pressure and through argon dilution. The maximum achieved growth rate of 9.8 μm/hour represents more than an order of magnitude increase compared to traditional growth rates in MBE, and even exceeds those commonly used in MOCVD. To overcome a challenge introduced by the higher growth rates, we explore the use of alternative n-type doping methods. The high growth rates, resulting low unintentional doping levels, and excellent uniformity over

large areas opens the door for the use of MBE for novel devices utilizing thick indium-bearing layers, as well as existing devices where the traditional slow growth in MBE was previously not viable.

4.2 Experimental Setup

All films in this study, unless otherwise specified, were grown in a Riber 32 MBE system with a base pressure of approximately $8x10^{-11}$ Torr. The substrates were single-side polished 1x1 cm sapphire, 1x1 cm GaN templates, or 2" sapphire wafers. All substrates were sputter coated with 2 μm of tantalum on the back side for heat absorption and spreading. After cleaning in a 4:1 solution of H_2SO_4:H_2O_2, the substrates were loaded into an introductory chamber on an indium-free molybdenum block, and then outgassed at 150°C for 20 minutes. The samples were then transferred to the growth chamber and were outgassed for an additional 10 minutes at 600°C for the GaN template substrates or 850°C for the sapphire substrates. Any substrate temperatures listed herein were those measured by thermocouple. For all film growths, nitrogen was supplied by a Veeco UNI-Bulb RF plasma source, with several modifications which will be described later. The gas flow and RF power were varied throughout the study to achieve the desired surface conditions, and also to explore their effects on growth rate. Aluminum was supplied by a cold-lip effusion cell, gallium was supplied by a standard effusion cell and/or a Veeco dual-filament SUMO cell, and germanium was supplied by a standard effusion cell for n-type doping. The total Ga fluxes used in this study varied from ~$8x10^{-7}$ Torr beam equivalent pressure (BEP) up to ~$3.6x10^{-6}$ Torr BEP.

The growth techniques employed herein were a combination of traditional MBE and a shuttered variation of MBE called Metal-Modulated Epitaxy (MME), the details of which can be found elsewhere.[80-82, 117] For the sapphire substrates, a low-temperature nitridation was performed for 1 hour at 200°C,[87, 92] followed by a 10 nm AlN nucleation layer under N-rich conditions (III/V ≈ 0.7) at 700°C. Then, a thicker AlN buffer layer was grown using MME at 850°C under Al-rich conditions (III/V ≈ 1.5), while the substrate temperatures during GaN growth were typically 600 to 650°C. This MME technique has been shown to achieve extremely high p-type doping,[54, 105] control phase separation in InGaN,[153, 154] and result in excellent uniformity and material utilization due to the temperatures substantially lower than traditional PAMBE.

The film growth was monitored *in situ* by reflection high energy electron diffraction (RHEED), and the plasma emission spectra were monitored through the rear window of the plasma source looking through the pyrolytic boron nitride (PBN) bulb using an Ocean Optics HR-2000+ES spectrometer in the wavelength range of 200-1100 nm. Post-growth structural analysis was performed by x-ray diffraction (XRD) using a Philips X'Pert Pro MRD, and the surface morphology of the films was characterized by a Veeco Dimension 3100 atomic force microscope (AFM) operated in tapping mode. Film thicknesses were verified by either contact profilometry or spectroscopic ellipsometry. Hall Effect was employed to determine the electrical properties of select films using a 0.3T fixed magnet or a custom Hall effect system with a 1.5T electro-magnet.

4.3 Plasma and Chamber Modifications

In order to facilitate the dramatically increased growth rate in this study, several important modifications were made to the plasma source and the growth chamber. Two additional cryo pumps (CTI-10) were added, each on a separate 10" outer diameter conflat flange. The overall pumping system for the growth chamber consisted of one CTI-8 cryo pump, two CTI-10 cryo pumps all used during growth, and one ion pump and a titanium sublimation pump used when not growing. With the added cryo pumps, the pumping capacity during growth was more than tripled compared to the previous single cryo pump configuration. This increased capacity resulted in a substantial reduction in the chamber pressure during growth, never exceeding 10^{-4} Torr even with more than 30 standard cubic centimeters per minute (sccm) of N_2 flow. The lower chamber pressure reduces wear on effusion cell filaments, and could serve to decrease scattering of the incident flux to improve growth rates.

In addition to the added pumping capacity, the plasma source itself was also slightly modified. The original plasma aperture was replaced with a custom 5.6X higher conductance aperture in order to allow for higher gas flow while maintaining the correct plasma mode. With the original aperture, the plasma switched to a dim mode resulting from excessive back pressure behind the aperture with a nitrogen flow of just 3.25 sccm, but remained lit in the bright mode with flow less than 1 sccm. Using the new high-conductance aperture, the plasma required substantially higher nitrogen flow of at least 3 sccm to remain ignited, but continued in the bright mode up to the maximum tested nitrogen flow of 34 sccm.

4.4 Growth Rates with Modified Plasma

In order to initially characterize the plasma source, the GaN growth rate was determined using post-growth thickness measurements combined with *in situ* estimation of III/V flux ratios by transient RHEED analysis. The RHEED and post growth methods matched to less than 5% accuracy in all cases. To avoid desorption of the Ga flux, the samples used for growth rate determination were grown at a low substrate temperature of 600°C under metal-rich conditions. The nitrogen flow was initially varied from 3 sccm to 17 sccm with a fixed power of 350W, and then the plasma power was varied from 350W to 500W with a fixed nitrogen flow of 15 sccm. This resulted in growth rates of 1.5 μm/hour to 6.1 μm/hour. Using pure nitrogen at 500W RF power and increasing the flow to 34 sccm using a second mass flow controller yielded a growth rate of 8.4 μm/hour.

To assist in the initial striking of the plasma after baking the system, a light flow of argon gas was added which is easier to ignite than pure nitrogen. After the plasma ignited, the argon flow was cut off and the plasma transitioned to pure nitrogen. However, it was observed that this procedure resulted in an increase in the active nitrogen flux for films grown immediately after the use of argon. As such, another test was performed to determine the effect of argon on the growth rate for various conditions. From this test, it was discovered that the growth rate increased by approximately 20 to 50 percent at high and low nitrogen flows, respectively, with the addition of 7.7 sccm argon into the plasma. Shown in Figure 4.1 is the overall growth rate as a function of these various plasma conditions, with growth rates from approximately 1.5 μm/hour to 9.8 μm/hour. Moreover, the uniformity for these high growth rates was excellent as

measured across a 2" wafer by spectroscopic ellipsometry, demonstrating a standard deviation of just 2% for a 4 μm thick film.

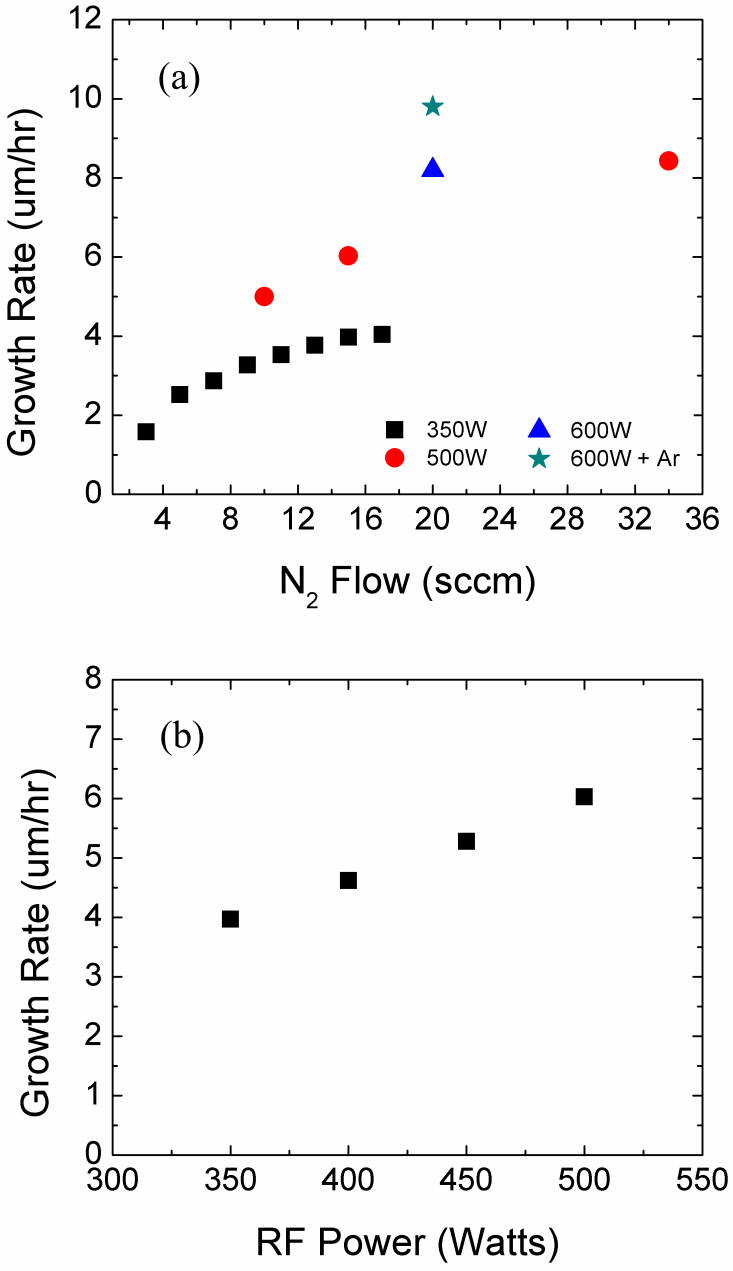

Figure 4.1: (a) GaN growth rate versus nitrogen flow for various RF power conditions, and (b) growth rate vs. RF power for a fixed nitrogen flow of 15 sccm.

The maximum growth rate was achieved using 600W RF power with 20 sccm

nitrogen and 7.7 sccm argon flows, which is limited by our current mass flow controller hardware configuration. This condition resulted in an extremely high growth rate of 9.8 μm/hour which is, to our knowledge, the highest ever reported for GaN grown by MBE. Under this same condition using 20 sccm nitrogen without argon, the growth rate dropped to 8.2 μm/hour.

While the demonstration of high growth rates is beneficial for future applications, the films must also remain sufficiently high quality in order to be useful. Shown in Figure 4.2 is a representative RHEED image during growth, as well as a 2x2 μm AFM image for a film grown at 6.1 μm/hour. As shown in Figure 4.2(a), during the growth of these films under metal-rich conditions at 600°C the RHEED patterns remained streaky and a 2x2 reconstruction was observed, indicating a smooth growth surface. The AFM image in Figure 4.2(b) shows excellent dislocation-mediated step-flow morphology with clear atomic steps and spiral hillocks and a root mean square (RMS) roughness of just 0.8 nm. Such a surface structure is typical for high quality GaN grown by MBE, and is also seen at much lower growth rates.[110, 155] For comparison, a similar AFM surface morphology is shown in Figure 4.2(c) which also demonstrates the same smooth step-flow growth at a lower growth rate of ~2 μm/hour. This observation confirms that the 2D growth mode is preserved even at growth rates more than an order of magnitude higher than are commonly used in GaN MBE.

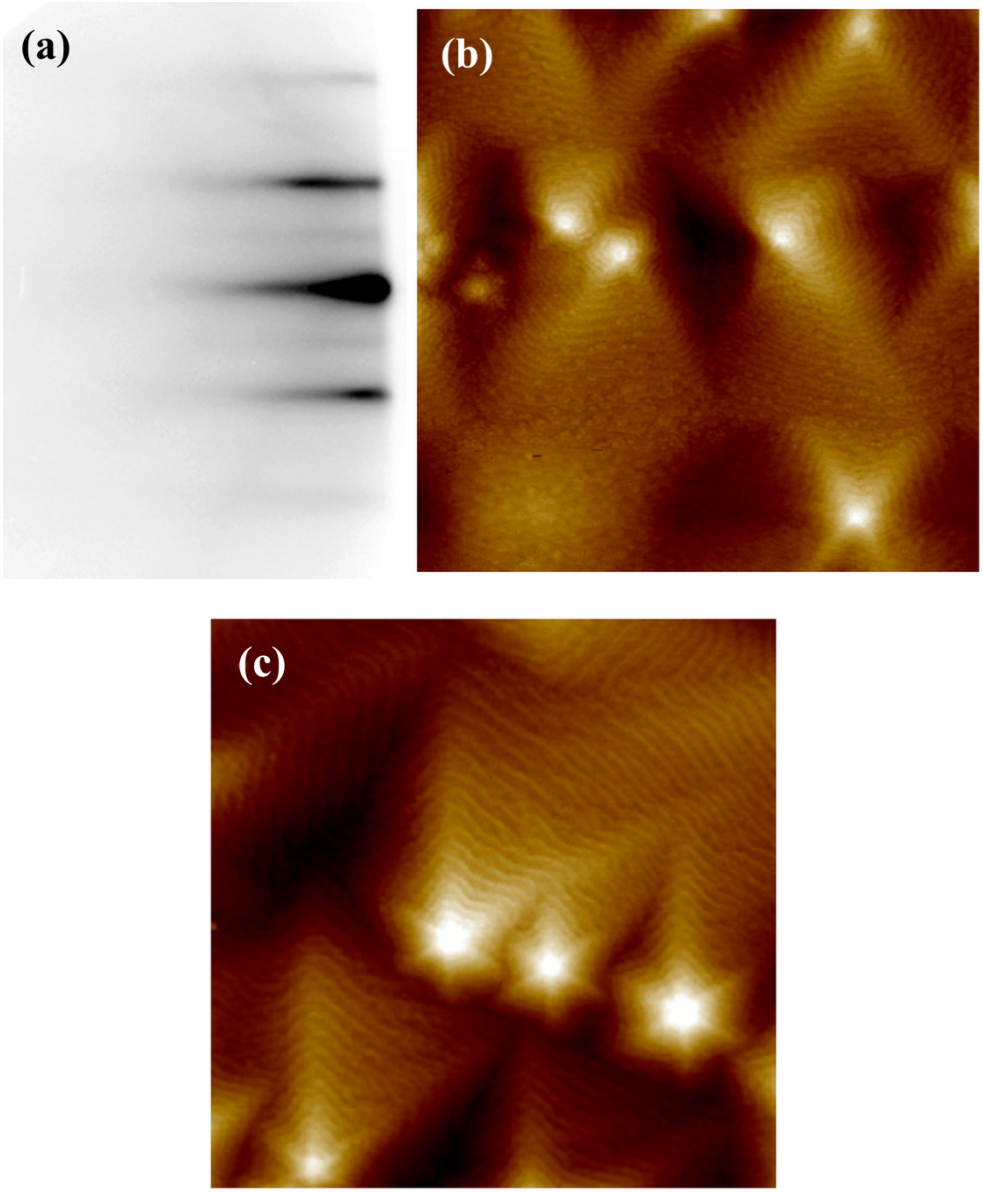

Figure 4.2: (a) RHEED image taken after growth, (b) resulting AFM scan for GaN film grown at 6.1 µm/hour at a substrate temperature of 600°C, and (c) additional AFM scan for a lower growth rate of 2.0 µm/hour. [Height scale = 7 nm, RMS roughness = (b) 0.8 nm, and (c) 1.0 nm]

In an effort to understand the physical explanation for the growth rate change with versus without argon, the plasma emission spectra were compared using a simple fiber-coupled spectrometer on the rear plasma window and are shown in Figure 4.3. The

spectra in Figure 4.3 represent 20 sccm pure N_2 (black), a mixed plasma using 20 sccm N_2 with 7.7 sccm Ar (red), and finally a pure 7.7 sccm Ar (blue) using 350W of RF power in all cases. Figure 4.3(b) shows the 550 nm to 690 nm region corresponding to excited molecular nitrogen (N_2^*) which has previously been shown to directly affect growth rate of III-nitrides in plasma MBE.[26, 144, 156]

From Figure 4.3(b) it is clear that the addition of argon had no meaningful effect on the excited molecular nitrogen bands, in contrast to other findings using a mixed N_2/Ar plasma.[24] However, the intensities of the argon-related emission lines were dramatically reduced by a factor of 3-4x in the mixed plasma compared to the pure argon plasma. Thus, it is possible that the reduction in argon-related emission intensity in the mixed plasma could be due to the transfer of kinetic energy from the argon species to the nitrogen species, enhancing the formation of other active nitrogen species besides molecular species and increasing the growth rate.

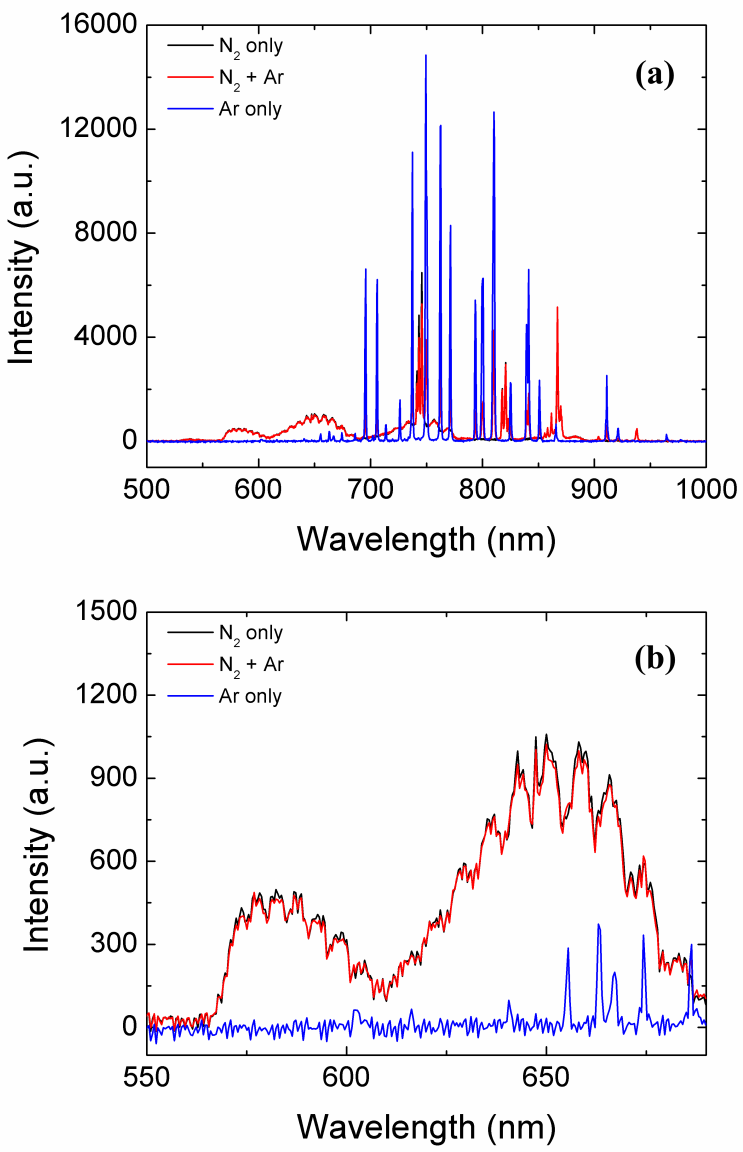

Figure 4.3: (a) Full range plasma spectra from 500-1000 nm and, (b) close-up of the 550-690 nm wavelength range (right) associated with excited molecular nitrogen species. Plasma power of 500W using gas flows: 20 sccm N2 only (black), 20 sccm N2 + 7.7 sccm Ar (red), and 7.7 sccm Ar only (blue).

To further explore the effects of argon in the plasma, the manipulator was put into the flux measurement position while measuring the collector current using a Keithley 6517B electrometer with the collector bias held at 0V. During the measurement, the grid voltage was set to 0V and the flux gauge filament was turned off to ensure with the

collector shielded by earth ground except for a small opening facing the plasma source. This ensured that the only ionized species reaching the collector were those coming from the plasma source itself and/or species created near the collector of the ion gauge. As such, the collector functioned similar to a Langmuir probe where the collector current is related, albeit indirectly, to the ion content of the plasma as will be discussed below.[157, 158] Shown in Figure 4.4 is the resulting probe current from this experiment at 300W RF power as a function of the nitrogen/argon concentrations as well as the approximate pressure inside the plasma bulb (i.e. behind the aperture plate) as calculated by the mass flow rate and the theoretical conductance of the aperture plate.

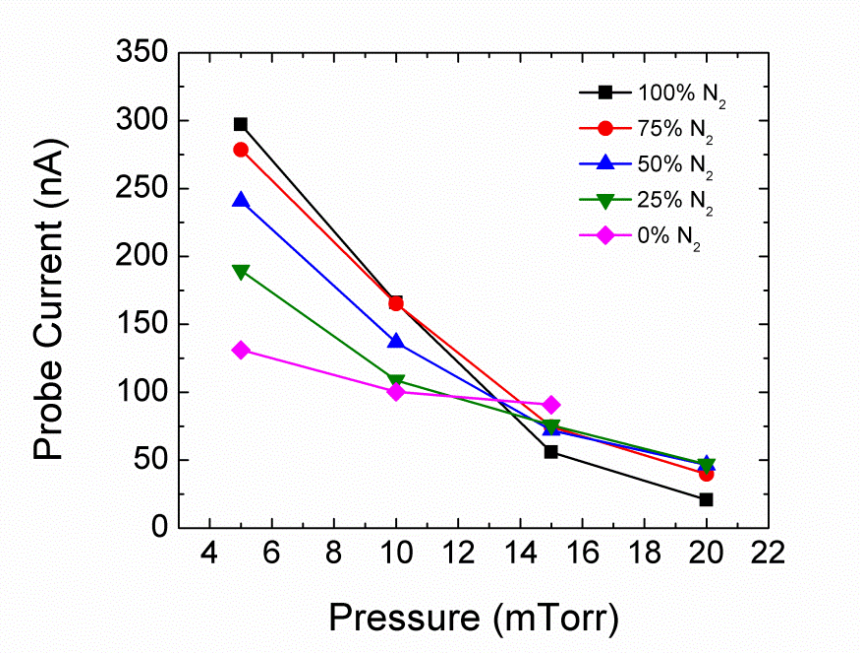

Figure 4.4: Probe current as a function of pressure measured for various plasma compositions.

It should be first emphasized that this experimental configuration with zero bias will result in the collection of both electrons and ions, and is thus related to but not equal to the ion content. With a positive bias applied to the grid, positively charged primary

ions should be rejected and negatively charged primary electrons attracted, or vice versa for a negative bias on the grid. However, in this experiment it was found that the probe current was always negative with a magnitude of at least 10 nA regardless of applied grid bias up to ±20V. This was not a measurement offset error as the probe current was less than 10 pA while the plasma was turned off. Thus, the only reasonable explanation for this persistent large negative current is the presence of a high density of secondary electrons created by the primary high energy species (ions and/or electrons from the plasma) which overwhelm the primary ion and electron currents from the plasma itself. Secondary electrons can be generated from nearby surfaces via impact ionization or photoemission, the latter having been acknowledged as a complicating factor but discounted herein as has been done in prior more detailed characterization efforts.[157] Because the trends in optical intensity (described later) do not follow the trends in probe current, the role of photoemission is assumed negligible in the present case. However, both of these mechanisms (impact ionization and photoemission) suggest that the plasma produces sufficiently high energy primary species to cause ionization and, thus, potential ionizing damage to the sample during growth. Thus, we do not treat the measured collector currents as a direct measure of ion current but instead an impact ionization enhanced current related to but not equal to ion current. Therefore regardless of sign of the current, variations in the current are assumed to originate from changes in the high energy, potentially damaging, primary plasma species.

From Figure 4.4 it is clear that, in the lower pressure regime, the pure nitrogen plasma results in a dramatic increase of more than 100% in probe current compared to the pure argon plasma. Additionally, with proper dilution of the nitrogen with argon at lower

pressure/flow, the probe current, and thus inferred ion/electron primary current, can be dramatically reduced in order to minimize any detrimental effect of high energy species bombarding the sample surface and causing damage. Higher plasma pressure suppresses the ion content, making the ion content relatively unaffected by plasma composition. This observation of probe current shows two mechanisms to control plasma damage due to high energy speces: in the lower flow regime by argon dilution and in the higher flow regime via pressure.

Shown in Figure 4.5(a) and (b) are the emission intensities at 300W RF power for the 650 nm and 821 nm plasma emission lines relating to molecular nitrogen and atomic nitrogen transitions, respectively. The 650 nm emission from excited molecular transitions in Figure 4.5(a) shows a monotonic increase in intensity with increasing nitrogen composition in the plasma, and also with increasing pressure. Interestingly, a substantially different trend can be seen in the 821 nm atomic emission in Figure 4.5(b) where the intensity trends do not follow the 650 nm molecular increases. At lower nitrogen compositions of 25% and 50%, the atomic nitrogen intensity increases with increasing pressure. However, above 50% nitrogen there is a peak in the atomic emission intensity at ~10 mTorr which then decreases at higher pressure. In the case of a pure nitrogen plasma, the atomic emission intensity is nearly 55% higher at 10 mTorr compared to 20 mTorr. The overall atomic nitrogen intensity is highest for a diluted plasma with just 50% nitrogen at 20 mTorr.

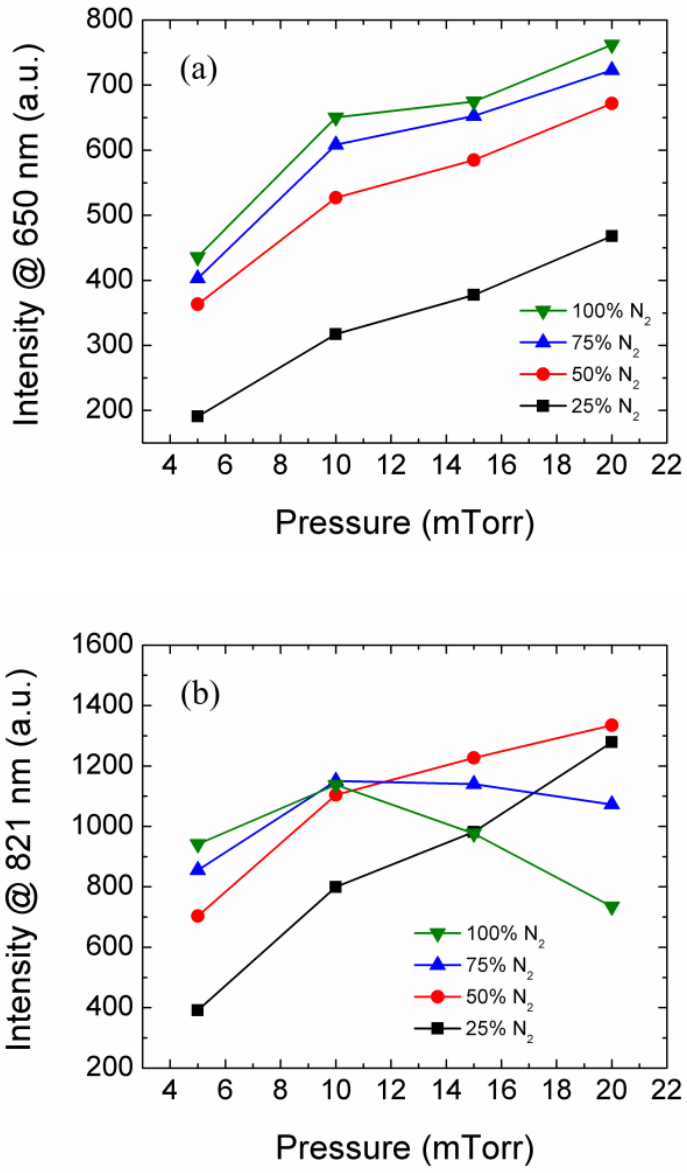

Figure 4.5: (a) Plasma emission intensity for various plasma pressures and compositions at 650 nm related to molecular nitrogen and, (b) 821 nm related to atomic nitrogen.

These trends in the atomic nitrogen intensity can further explain the increased growth rate with argon as described previously and as shown in Figure 4.1(a). In the literature, there is no clear consensus which nitrogen species (atomic or molecular) is the primary contributor to growth during PAMBE of III-nitrides.[26, 144, 159] In this work,

at the higher plasma pressures where the growth rate is highest, there is a substantial shift in the trends of atomic nitrogen intensity compared to molecular nitrogen. In the high pressure/flow case, the dilution with ~25-50% argon minimally reduces the molecular emission but substantially increases the atomic emission intensity of the plasma. Thus, one would assume that the 20-25% increase in growth rate observed in Figure 4.1(a) results from an enhancement in atomic nitrogen, not the traditionally assumed excited molecular species. At lower plasma chamber pressures, 10 mTorr or less, both the molecular and atomic nitrogen intensities are highest using a pure nitrogen plasma. But, at higher pressures like those used to achieve growth rates above 6 μm/hour, the atomic nitrogen is maximized for a mixed chemistry plasma with ~50% argon dilution. The maximum growth rate of 9.8 μm/hour reported here was achieved at a pressure of ~30 mTorr with a nitrogen composition of ~72%. A more in-depth study is currently underway in order to explore the relative effects of atomic and molecular nitrogen and the various plasma conditions on growth rate and structural/optical quality. But, from this preliminary characterization of the plasma, it is clear that both the atomic and molecular nitrogen species are important to consider, especially at the extremely high growth rates reported herein.

In this study, the maximum growth rate achieved was not limited by the plasma source, but rather by the 20 sccm nitrogen mass flow controller which indicates that even higher growth rates should be possible. In addition, the growth rate can be reduced by varying the nitrogen and argon at low flow rates. With pure nitrogen, the plasma extinguished at a flow of ~3 sccm due to insufficient back-pressure. However, it could be sustained by using a combination of 1 sccm of nitrogen with 7.7 sccm of argon,

resulting in more traditional growth rates closer to 1 μm/hour. By lowering the argon content further, an additional reduction in growth rate might also be achievable to extend the range of possible growth rates. The varied growth rate from ~1 μm/hour up to 9.8 μm/hour represents nearly an order of magnitude achievable range of growth rates which can be tuned for rapid growth of thick buffer layers or precisely controlled quantum wells.

4.5 Doping at High Growth Rates

In order to achieve sufficient n-type doping at these elevated growth rates, some reconsideration of the Si doping method is needed. Typically, n-type doping in MOCVD growth using Si is limited to the low or mid 10^{19} cm^{-3} range due to tensile stress and film cracking during cool-down, as well as morphological degradation at higher Si concentrations.[160, 161] In MBE, due primarily to the lower substrate temperatures, this is less of an issue.[162] Using MME, we have previously achieved extremely high Si doping with an electron concentration up to $2.5x10^{20}$ cm^{-3} and resistivity of $5x10^{-4}$ Ω-cm for a 900 nm thick film with RMS roughness of just 0.3 nm. This film was grown at ~1μm/hour, and the Si dopant cell required a temperature in excess of 1200°C. However, in order to achieve this high level of doping at elevated growth rates, an even higher cell temperature would be required, pushing the power limits of the cell and reducing effusion cell and/or crucible lifetime.

To circumvent this doping challenge at high growth rates, the use of Ge was explored as an alternative.[163, 164] Compared to Si, Ge has approximately two orders of magnitude higher vapor pressure for the same temperature.[165, 166] Or, to achieve

the same vapor pressure as Si, a Ge cell could be run at approximately 200°C lower temperature. Ge has been shown to have similar activation energy to Si in GaN, and induces substantially less stress on the crystal due to its closer atomic size match to the Ga atom it substitutes in the lattice.[167, 168] Given the lower temperature requirements with similar activation, Ge would seem an excellent alternative for high growth rate GaN. The use of Ge was investigated by varying the Ge cell temperature from 760°C to 1000°C with a fixed growth rate and Ga flux, as shown in Figure 4.6. Sapphire substrates were used for this study to provide complete electrical isolation and minimize the effect of surface contamination. A ~500 nm thick AlN buffer layer was grown by MME after low-temperature nitridation. The resulting AlN, grown at nearly 2 μm/hour, showed (002) rocking curve (omega scan) full width at half maximum (FWHM) of around 80 arcsec with RMS roughness of ~0.5 nm. For the Ge-doped GaN grown at 650°C, MME was employed using a 10s open / 10s closed shutter modulation with a III/V ratio of approximately 1.8, and both Ge and Ga were shuttered simultaneously. The plasma condition for these films was fixed at 350W RF power with 4 sccm N_2 flow, yielding a growth rate of approximately 2 μm/hour.

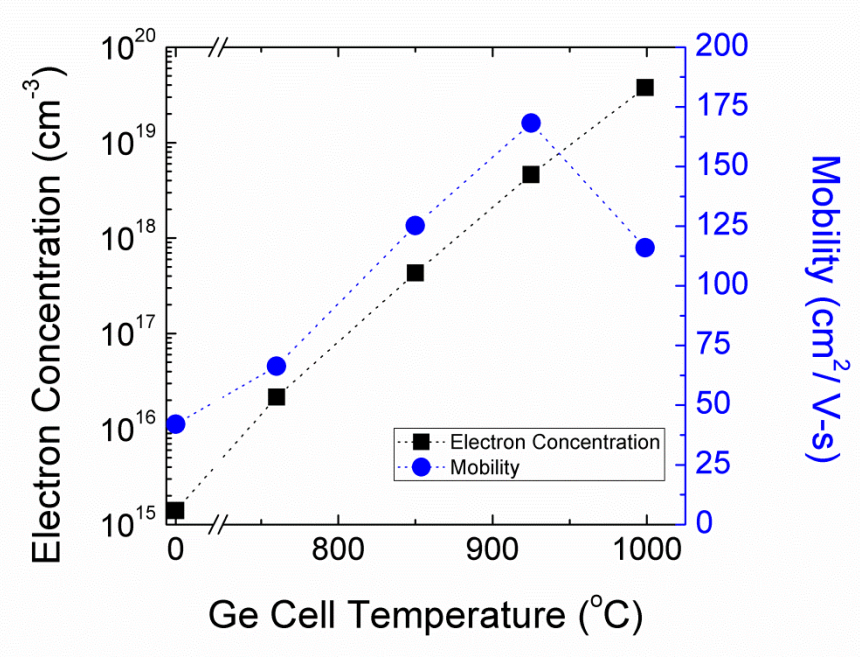

Figure 4.6: Electron concentration (black) and mobility (blue) as a function of Ge cell temperature.

As shown in Figure 4.6, the electron concentration exhibits a highly predictable exponential dependence on the Ge cell temperature. The electron concentrations achieved varied from 2.2×10^{16} cm^{-3} at a Ge cell temperature of 760°C up to 3.8×10^{19} cm^{-3} at a Ge cell temperature of 999°C. These low dopant cell temperatures leave substantial headroom for high n-type doping at high growth rates while simultaneously reducing wear on the cell and crucible. As a baseline, several unintentionally doped (UID) GaN films were grown by MME in order to characterize the background electron concentration. Since MBE grown films have background impurity concentrations inversely proportional to growth rate, low background impurity concentrations are expected at these high growth rates. Indeed, with the same conditions as discussed above, the UID GaN films exhibited repeatable background electron concentrations of 1-2×10^{15} cm^{-3} with resistivity on the order of 50-100 Ω-cm. The mobility, shown in blue in

Figure 4.6, initially rises with increasing Ge cell temperature then begins to fall once the electron concentration exceeds ~$4x10^{18}$ cm^{-3}. This trend, along with the relatively low overall mobility, can be explained in the context of relatively high dislocation density resulting from the immature nature of these initial high growth rate studies.

In these non-optimized 1.8 μm thick GaN films grown on AlN buffer layers on sapphire, the XRD GaN (002) and (102) omega rocking curve FWHM are typically on the order of 250 arcsec and 1500 arcsec, respectively. Based on simple estimations from these two rocking curves, the threading dislocation density in these Ge-doped films is expected to be on the order of $5x10^{9}$ to $1x10^{10}$ cm^{-2}.[10, 169, 170] With these relatively high dislocation densities, the mobility is strongly affected by dislocation scattering at low carrier concentrations. At higher carrier concentrations, the dislocation scattering is minimized due to charge screening, while at very high doping concentrations the mobility again decreases due to ionized impurity scattering.[171, 172] Thus, while the mobility in these Ge-doped samples is relatively low, it is well-described by physical models and limited by dislocation density.[173] It is expected that the mobility should be substantially higher when grown on lower dislocation density GaN templates or freestanding GaN.

4.6 Challenges at High Growth Rates

While the above results are promising for a number of possible applications, there are still challenges to be addressed at these extremely high growth rates. During the span of these studies, the most commonly encountered issue was macroscopic surface features on the film. Shown in Figure 4.7 is an optical microscope image for a film grown at 8.2

μm/hour which exhibits dark clusters as well as transparent hexagonal pyramids. The most likely explanation for these surface features is "spitting" from the Ga cell and subsequent nitridation / non-epitaxial crystal formation. At very high fluxes, like those used here, Ga has a tendency to "spit", wherein large clusters of Ga exit the end of the effusion cell rather than an ideal uniform flux. In Figure 4.7, the dark clusters are likely metallic gallium clusters which were unable to incorporate correctly or formed a nitride skin, while the transparent hexagonal pyramids are expected to be GaN crystallites.

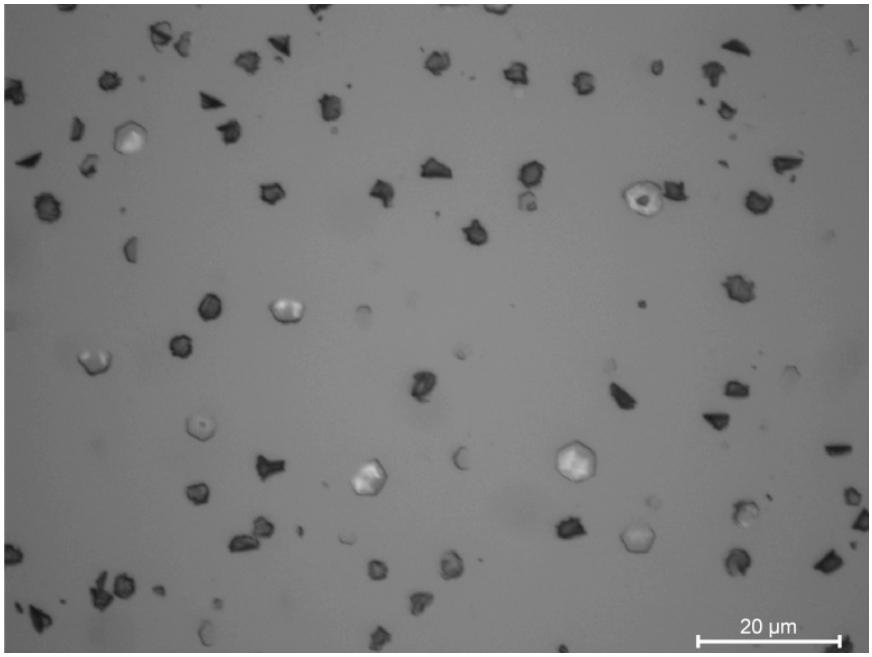

Figure 4.7: Optical microscope image of GaN grown at 8.2 μm/hour.

Given the smooth morphology in the AFM image in Figure 4.2(b), the surface features appear to be associated with the Ga source(s) rather than a degradation of the growth mode at elevated growth rates. The primary dual-filament Ga cell in this work was designed to mitigate the spitting issue but, at these extremely high growth rates, that

alone was insufficient to eliminate the surface features altogether. In our system, the simultaneous use of two Ga cells did show some reduction of the large surface features, but similarly did not completely eliminate the problem. Thus, some improvements in cell or crucible design would be necessary for this high growth rate to become commercially viable. A valved cell, aperture plate, or dramatically tapered crucible could potentially overcome this issue by removing or substantially decreasing the direct line-of-sight from the Ga pool to the sample surface. At elevated growth rates above 4 μm/hour, the onset of Ga spitting, and the resulting surface features, make Hall effect measurements impractical. As such, no accurate doping or UID electron concentration observations for high growth rate films can be made until the spitting issue is resolved.

4.7 Conclusions

In conclusion, we have demonstrated the use of a mixed chemistry plasma in order to achieve GaN growth rates of nearly 10 μm/hour by plasma assisted MBE. By adding argon to the plasma gas flow, substantial growth rate increases can be achieved while also allowing lower growth rates through proper dilution of the nitrogen at low flow rates, resulting in a growth rate range of ~1 μm/hour up to 9.8 μm/hour. The Langmuir probe current, and thus indirectly the ion content of the plasma, was measured *in situ*. It was found that the high energy species hitting the substrate could be reduced by changing the plasma pressure as well as the argon/nitrogen chemistry, providing an additional mechanism to tune the growth rate while simultaneously minimizing possible surface damage. Further characterization of the plasma emission spectra points to a significant contribution from atomic nitrogen to the net growth rate, where the atomic

nitrogen is maximized for a mixed argon/nitrogen plasma at higher plasma chamber pressures. The surface morphology of the high growth rate MME films shows no degradation of the growth mode, maintaining a dislocation-mediated step-flow growth with sub-nanometer RMS roughness even at relatively low substrate temperatures. In order to address doping challenges associated with Si doping at high growth rates, Ge was explored as a possible alternative. Electron concentrations were achieved from $2x10^{16}$ cm^{-3} up to $4x10^{19}$ cm^{-3} for growth rates of ~2 μm/hour while operating the Ge dopant cell nearly 200°C cooler than would be required for equivalent Si doping. Repeatable background electron concentrations of $1\text{-}2x10^{15}$ cm^{-3} were achieved for unintentionally doped films grown under these conditions. While these results are promising, films grown at higher growth rates exhibited large surface features, most likely due to Ga "spitting" from the effusion cell. Improved crucible or cell designs should minimize these detrimental surface features. Nonetheless, such an engineering challenge is relatively straightforward, and the preservation of an ideal step-flow growth mode proves the fundamental viability of these high growth rates.

CHAPTER 5: GROWTH OF GaN ON Si SUBSTRATES

5.1 Introduction

With existing Si solar cells with highly optimized designs approaching the theoretical limits, the question arises: where does Si go next? Given competition from thin-film solar materials such as copper indium gallium (di)selenide (CIGS) and CdTe which exceed 20% efficiency,[174] the next logical step in the evolution of Si PV devices is to a tandem device wherein the Si substrate is also the bottom sub-cell, with a wider bandgap collection junction grown on top. Unfortunately, the wider bandgap requirement of the top cell rules out many traditional semiconductor materials like GaAs. Thus, other compound semiconductor materials, such as InGaP or GaAsP, must be considered in order to achieve the correct band gap configuration. An alternative to these traditional III-V compound semiconductors is the III-nitride system which boasts a broadly tunable, direct bandgap as well as very high absorption coefficients and radiation tolerance, making it an attractive material for both terrestrial and space applications.

However, the growth of these compound semiconductor materials presents a number of major challenges. The lattice mismatch between GaN and (111)-Si is ~17%, resulting in a high density of defects including threading dislocations and stacking faults. Moreover, the Si material is non-polar which can result in mixed Ga-polar and N-polar GaN films if growth conditions and buffer layers are not carefully selected and monitored. The thermal coefficient of expansion mismatch between the film and the substrate often results in cracking for thick films due to tensile stress during cool-down from growth temperatures. However, thick III-nitride layers are desirable in order to

annihilate threading dislocations and improve device performance.

To address the issue of tensile stress for thick films, complicated buffer layers including AlGaN or AlN interlayers and superlattices are often employed, counteracting some of the tensile stress from cool-down by imposing a compressive stress. However, these buffer layers also prevent conduction to the underlying Si substrate, making them unfit for a vertical-conducting solar cell structure. Thus, in order to achieve a III-nitride on Si based solar cell, buffer layers must be carefully chosen to avoid current blocking while simultaneously maintaining sufficient material quality for a PV device. The purpose of this study is to explore various nucleation and buffer techniques in order to grow a III-nitride on Si heterojunction solar cell with a vertically conducting design using a back-contacted Si substrate.

5.2 Experimental Setup

All films in this study were grown in a Riber 32 MBE system using either traditional nitrogen-rich MBE growth or the Metal-Modulated Epitaxy (MME) technique. A Veeco UNI-Bulb RF plasma source was used to supply active nitrogen, and was operated with a power of 350W and flow rate from 1.3 sccm (using a standard aperture plate) up to 20 sccm (using a high-conductance aperture plate). A Veeco SUMO cell was used as the primary gallium source, while standard effusion cells were used for indium, silicon, and germanium. A cold-lip effusion cell was used for aluminum, and magnesium was supplied by a Veeco corrosive series valved cracker. The substrates used were 2" diameter single-side polished (111)-oriented n- and p-type prime grade Czochralski (CZ) grown silicon wafers with a resistivity of ~10 Ω-cm. Float zone (FZ) wafers with ~5 Ω-

cm resistivity (both n- and p-type), offering higher minority carrier lifetime compared to the standard CZ wafers, were also used for some devices in order to obtain better photovoltaic performance.

The silicon wafers were all cleaned using a procedure similar to the RCA clean.[175] A DI water rinse and nitrogen dry were performed between each step in the cleaning process. The wafers were first cleaned for 10 minutes in a 4:1:1 solution of H_2O : NH_4OH : H_2O_2 heated to 100°C in order to remove organic contamination while leaving a thin oxide passivation. The oxide was then removed by dipping the wafers into dilute (~50:1) HF for 30 seconds. The wafers were next subjected to a second clean for 10 minutes in a 4:1:1 solution of H_2O : HCl : H_2O_2 heated to 100°C to remove metallic contamination which similarly resulted in a thin surface oxide layer. Finally, the wafers were once again dipped into dilute HF to remove the oxide, then rinsed thoroughly with DI water and dried using a nitrogen gun before being loaded into an indium-free molybdenum block and placed in an introductory chamber. The wafers were outgassed at 150°C for 20 minutes in the introductory chamber before being loaded into the growth chamber.

5.3 Wafer Outgassing Considerations

Once in the growth chamber, the wafers were monitored carefully using reflection high energy electron diffraction (RHEED) to look for key changes to the surface structure. The (111) face of silicon exhibits a characteristic 7x7 reconstruction in the absence of a surface oxide, and the presence of that reconstruction is a key marker that the wafer is clean and well-prepared for the initiation of growth. Due to brief air

exposure before loading into a vacuum chamber, a native oxide was formed and, thus, all of these silicon wafers did not show a surface reconstruction when first loaded into the growth chamber. The wafers were then briefly heated to ~800-850°C in the growth chamber to thermally decompose the surface oxide layer, which resulted in the characteristic 7x7 reconstruction as the wafers cooled.

As shown in Figure 5.1, while most wafers exhibited a typical 7x7 reconstruction, some showed a degradation of the RHEED pattern into a mixed spotty/streak pattern. This pattern indicates some surface roughening (spottiness), but also is highly anomalous because it was invariant with rotational angle.. This suggests that the sample reacted with some contaminant during the surface oxide decomposition at high temperature to form surface structure of unknown origin.

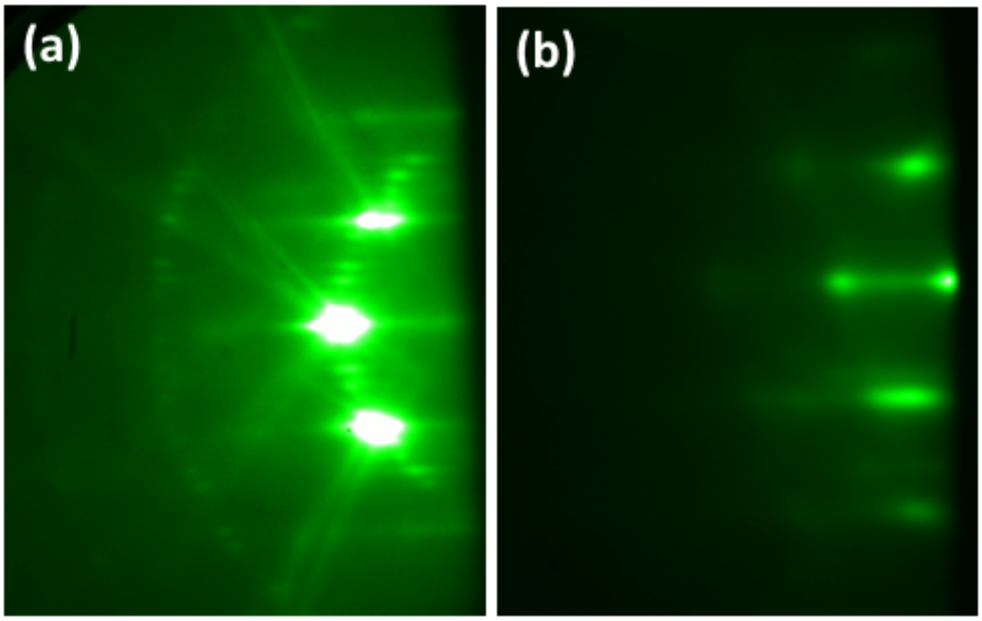

Figure 5.1: (Left) RHEED pattern for a clean Si wafer exhibiting 7x7 reconstruction from a smooth, oxide-free surface. (Right) Degraded RHEED pattern exhibited by certain samples indicative of surface contamination/reaction.

While the exact source of this RHEED degradation is not immediately clear, it is likely that the contamination comes from metallic residues on the molybdenum block, the decomposition of prior deposited nitride films on the block, or the molybdenum in the block itself. Because these molybdenum blocks were previously used for other III-nitride growths, they are inevitably coated in Al/Ga/In and their nitride compounds. While AlN is very thermally stable, even well above the 800°C outgas temperature, the same is not true for GaN, which begins to decompose at 750°C, or for InN, which begins to decompose well under 500°C.[176, 177] As the nitride films decompose, they release both metals and nitrogen which can react with the silicon surface at high temperature. This can be especially detrimental since all three metals can act as acceptors in Si which can potentially result in undesired p-type conductivity. After outgassing, the Si substrates were subjected to a number of different film nucleation procedures in order to limit some of the detrimental interface features discussed previously in Chapter 1. Substrate temperature, metal/nitrogen exposures, and various pre-treatments were all explored as possible routes to achieve a clean interface.

5.4 Gallium Droplet Nucleation

5.4.1 Surface Droplet Formation

In the first approach to this study, the goal was to achieve a surface whereby the subsequent GaN film could grow and coalesce laterally, thus resulting in a lower dislocation density via epitaxial lateral overgrowth (ELOG). The surface was exposed to ~2 monolayers of metallic gallium at 600°C, then the nitrogen plasma was ignited and

allowed to impinge on the substrate. This procedure resulted in the formation of small, sparse clusters of material on surface as shown in Figure 5.2.

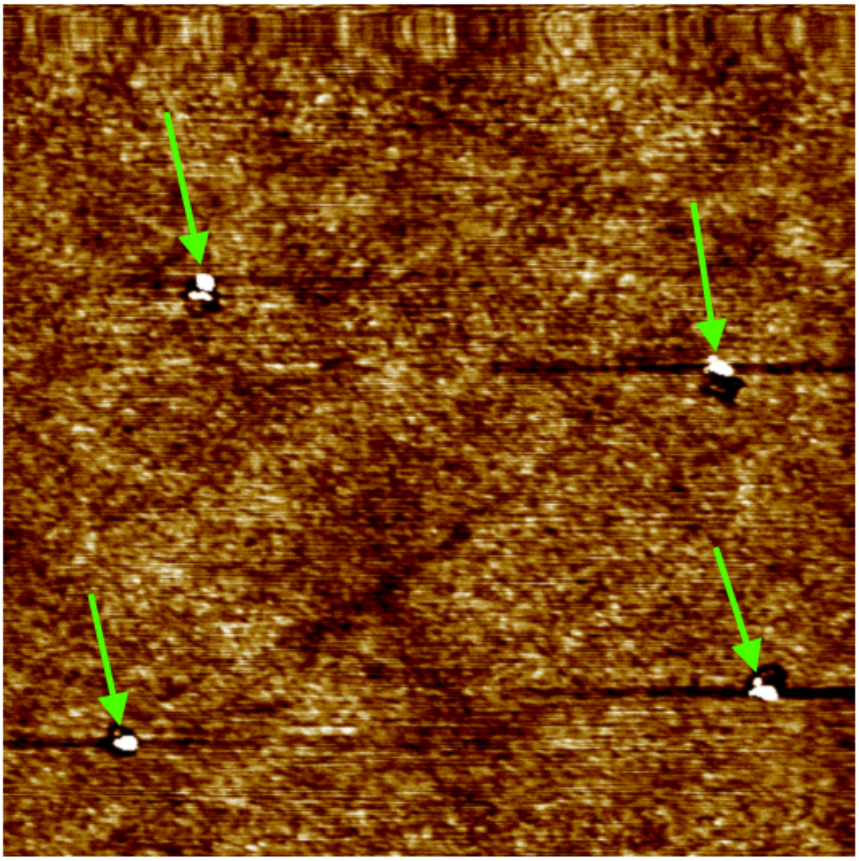

Figure 5.2: 2x2 μm AFM scan showing small ~50 nm diameter clusters of material (marked by green arrows) after pre-depositing 2 ML of metallic gallium then exposing to the nitrogen plasma.

Under normal conditions, a metal would typically deposit uniformly across the surface. However, in this case the metal was deposited at 600°C, well above the Ga melting point of just 30°C. Thus, the metal remained in a liquid state and formed droplets or clusters due to surface tension. When these droplets were exposed to the nitrogen plasma, they reacted to form a GaN crystallite. It was suggested that the crystallites, formed from a liquid melt, could be stress-free and contain very few

dislocations or structural defects which would be an excellent starting point for further GaN regrowth, provided that oriented coalescence of the nuclei could be achieved forming a complete film. The process flow for this concept is shown schematically in Figure 5.3.

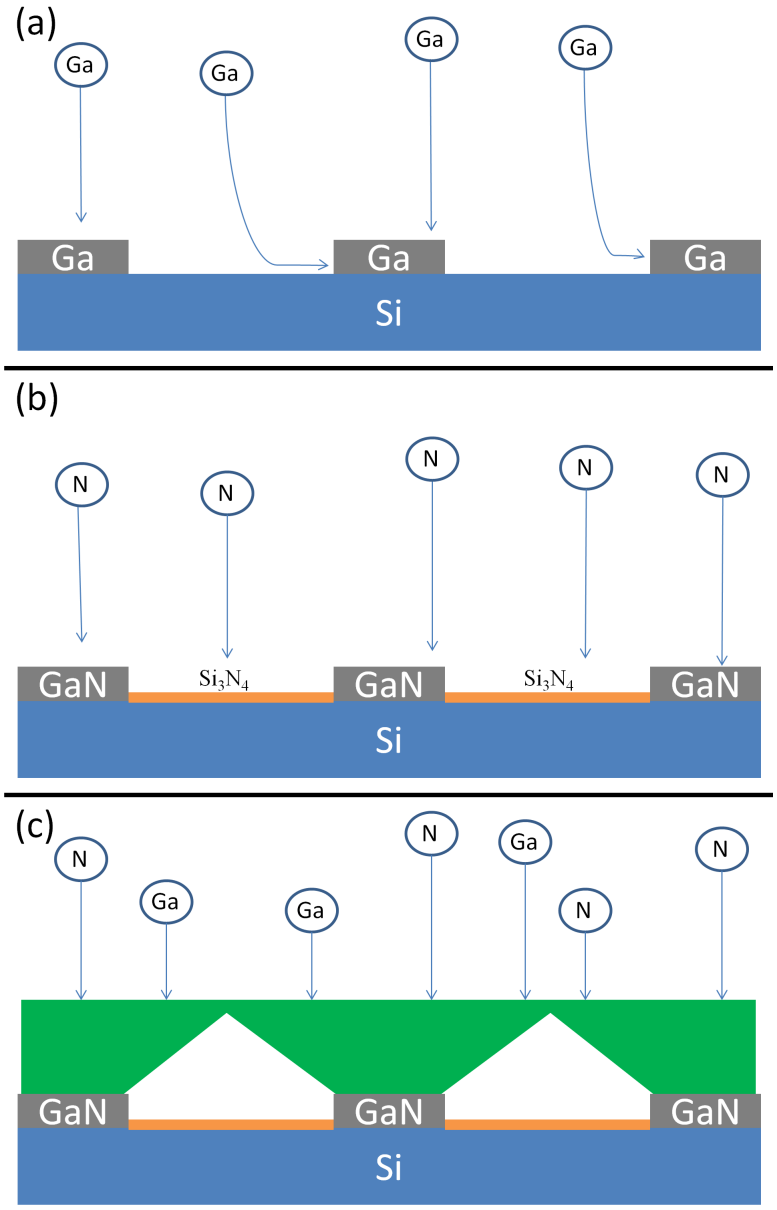

Figure 5.3: Schematic of growth sequence for GaN on Si. (a) Pre-exposure to Ga to form droplets, (b) nitridation to form GaN crystallites and Si_3N_4 in the field, and (c) growth of GaN with lateral coalescence.

5.4.2 Film Growth from GaN Crystallites

The next step attempting to build upon this promising idea/result in Figure 5.2 was to explore further GaN regrowth on the sparse GaN crystallites, as shown in the process flow in Figure 5.3. After Ga pre-exposure, the nitridation was allowed to proceed for a full 10 minute to ensure that all Ga was nitrided and that the remaining Si surface was fully converted to Si_3N_4. The conversion to Si_3N_4 is conceptually important since it should form an amorphous layer, preventing GaN growth and also passivating the surface to reduce surface recombination velocity in those areas of the Si wafer. Once the nitridation was completed, the GaN growth was performed using MME in an attempt to help promote lateral growth and smooth surfaces. The results of this are shown in the RHEED images during growth and AFM scan of the final film in Figure 5.4.

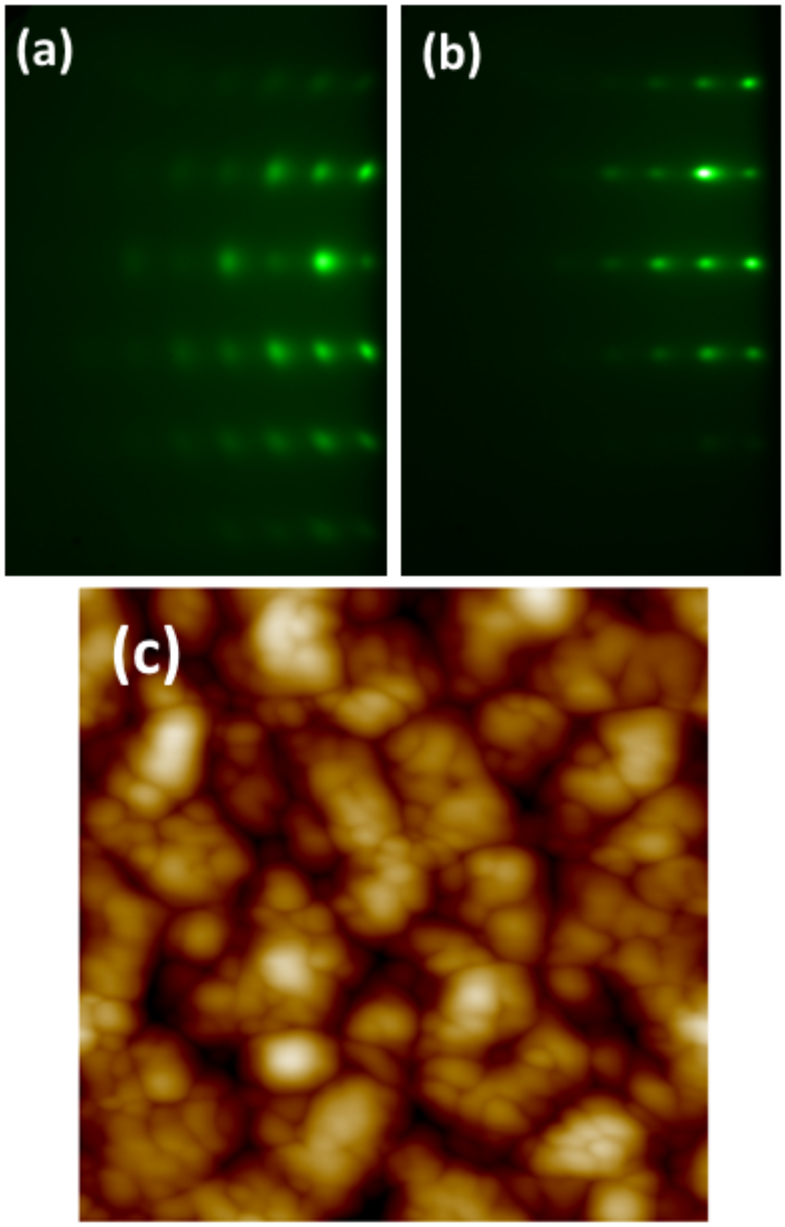

Figure 5.4: RHEED images (a) shortly after beginning GaN growth and (b) at the end of the GaN growth. (c) 1×1 AFM scan for GaN film grown on 111-oriented silicon substrate (RMS roughness = 6.5 nm).

The GaN growth initiated with a rough, spotty morphology as shown in Figure 5.4 (a). In fact, the RHEED spots appear to be a mix of traditional spots and concentric rings. Concentric rings in the RHEED typically indicate a polycrystalline film rather the

usual single-crystal films. This rough, spotty morphology continues into the final RHEED image in Figure 5.4(b) which indicates that the GaN film failed to achieve a smooth surface morphology even after 300 nm of MME GaN grown at conditions which typically result in excellent surface quality. The spotty pattern in the RHEED is further confirmed by the AFM scan in Figure 5.4 (bottom), which shows a generally rough surface, with a RMS roughness of 6.5 nm over the 1×1 μm scan area. There are no visible atomic steps or spiral hillocks typical of high quality GaN MBE. These observations can be explained in the context of the nitridation and nucleation processes. During the nitridation, the RHEED pattern (not shown) became spotty initially and then changed to a very dim, diffuse pattern. A diffuse pattern is typical of an amorphous film whereby no diffraction occurs and the beam is simply scattered onto the screen resulting in no pattern. While some residual pattern remained through the nitridation process, the pattern was weak and mostly diffuse, indicating that the silicon was likely being converted to amorphous silicon nitride.

The amorphous Si_3N_4 may be desirable if the coalescence is to occur laterally from the GaN crystallites, but the low substrate temperatures herein might have allowed GaN growth on the amorphous Si_3N_4 layers. If the film nucleated in the field on the Si_3N_4, instead of just from the GaN crystallites, then the resulting film quality should be very poor since there is no hexagonal crystal underlying the GaN growth onto which it can template. In addition, if GaN nuclei were formed on the amorphous Si_3N_4, then they would have no rotational alignment, resulting in grain boundaries as the rotationally misaligned nuclei coalesced. The XRD rocking curve FWHM of the (002) reflection for this film, and several others grown under similar conditions, was found to be in excess of

5000 arcsec and as high as 14000 arcsec, indicating a highly defective GaN film, which is not surprising given the nearly polycrystalline RHEED pattern present during the early phases of growth. When compared to a MOCVD GaN-on-sapphire template with a rocking curve FWHM of ~350 arcsec, or bulk quality wafers with rocking curve FWHM less than 20 arcsec, it is clear that these MME-grown films on Si were of very poor quality. This could point to growth in the amorphous Si_3N_4 field, or poor quality GaN crystallites and rotationally disordered subsequent coalescence.

To test the performance of this highly non-optimized initial structure of UID GaN on n-type Si, the wafer was fabricated into a basic solar cell using Ti/Al/Ti/Au finger-style contacts on the GaN and a full coating of Au on the backside of the silicon wafer. The I-V curve of the device under illumination is shown in Figure 5.5. Despite the poor GaN quality, under ~5 suns concentration the device exhibits a very promising short circuit current density (J_{SC}) of approximately 58 mA/cm^2 but a low open circuit voltage (V_{OC}) of just 0.3 V with a correspondingly low fill factor under 50%. The as-grown GaN film contained no intentional doping and, thus, the sheet resistance of the GaN film is likely far too high compared to normal solar cell structures. Moreover, the silicon wafer used as the substrate here was a simple moderately-doped silicon wafer rather than a solar-grade float zone wafer. While the device performance is nowhere near that of today's silicon solar cells, it nonetheless serves as a proof-of-concept that the GaN-on-Si heterojunction solar cell can potentially work. It is expected that further optimization of the growth, particularly for the initial nucleation process, and the use of higher quality substrates will result in substantially improved device performance.

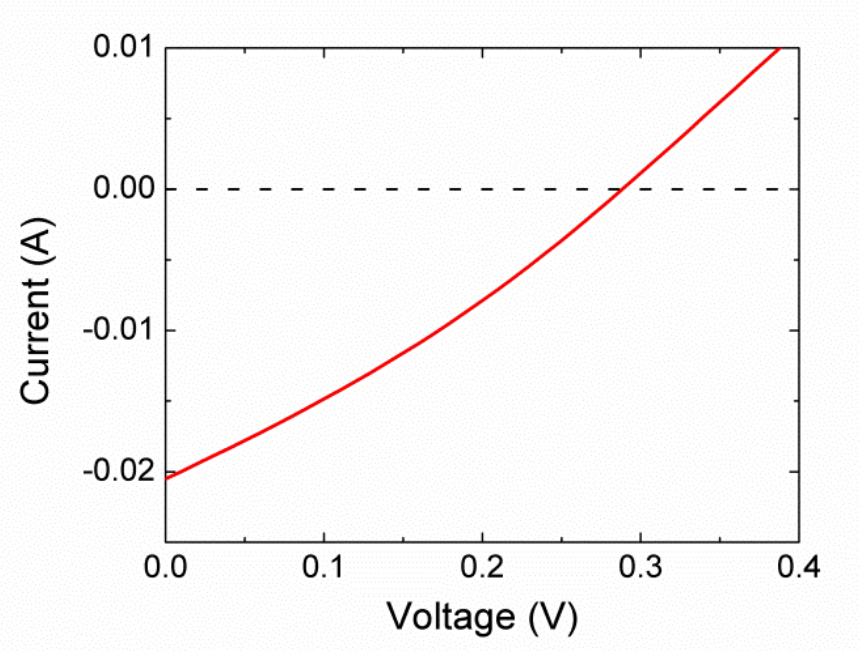

Figure 5.5: I-V curve of proof-of-concept GaN on Si solar cell with $J_{SC} \approx 58$ mA/cm^2 and $V_{OC} \approx 0.3$ V under ~5 Suns concentration.

5.4.3 GaN-Si Heterojunction Electrical Characteristics

Several growths were performed in parallel under similar conditions as above using high quality float zone Si wafers in an effort to understand the GaN/Si heterojunction: n-GaN/n-Si, n-GaN/p-Si, p-GaN/p-Si, and p-GaN/n-Si. For these films, the growth was performed with the modified plasma source discussed previously, yielding a growth rate of ~2 μm/hour. The n-type GaN was doped with Ge to provide an electron concentration of ~4x10^{18} cm^{-3}, while the p-type GaN was grown using a high hole concentration condition to yield hole concentrations on the order of 10^{19} cm^{-3}, and the III-nitride films were 100 nm thick in both cases. The Ga droplet formation and substrate temperatures were the same as described above, but maintaining the same III/V ratio resulted in smoother surfaces compared to the initial growth in the previous section

due to the higher overall metal dose per cycle. Shown below in Figure 5.6 are the 1x1 μm AFM images for these films showing the rough, grainy surface similar to Figure 5.4. Again, no atomic step edges are seen, and the resulting XRD rocking curve FWHM were on the order of 3000+ arcsec.

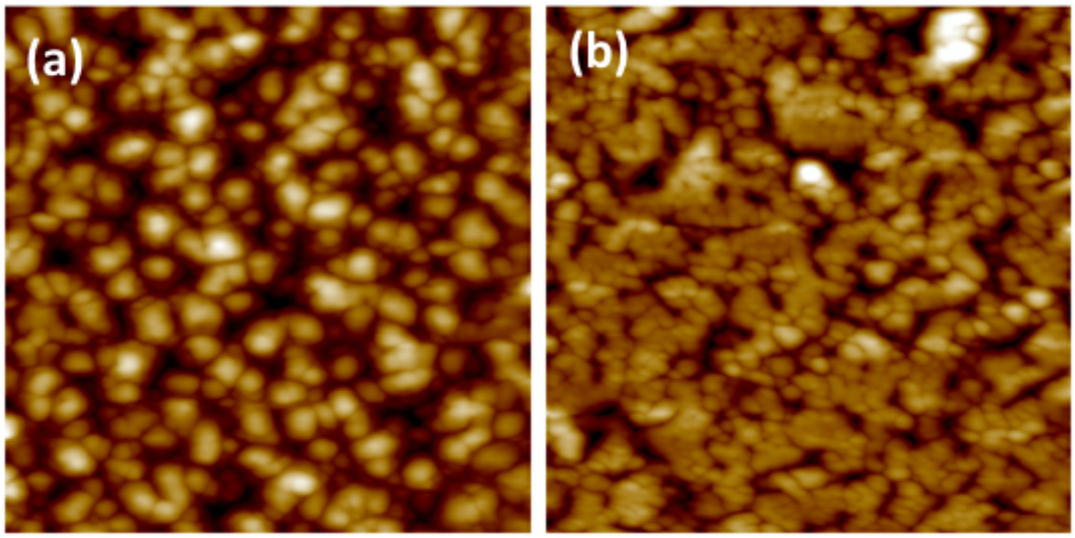

Figure 5.6: 1x1 μm AFM images showing surface morphology of (a) 100 nm thick p-type GaN (left, height scale = 32 nm , RMS roughness = 4.9 nm) and (b) n-type GaN (right, height scale = 25 nm, RMS roughness = 3.7 nm) grown on (111)-oriented Si substrates.

In spite of the poor crystal quality and rough surfaces, an effort was made to fabricate some simple solar cell structures. A finger pattern was defined using Pd/Au p-type GaN contacts and Ti/Al/Ti/Au n-type GaN contacts, while the back of the Si wafer was fully coated with Au. Shown in Figure 5.7 are the resulting I-V curves for these GaN/Si heterojunction solar cells in the dark (black) and under illumination (red). The illumination source was a 50 watt UV-deficient halogen bulb, operating at an approximate concentration of ~5 Suns.

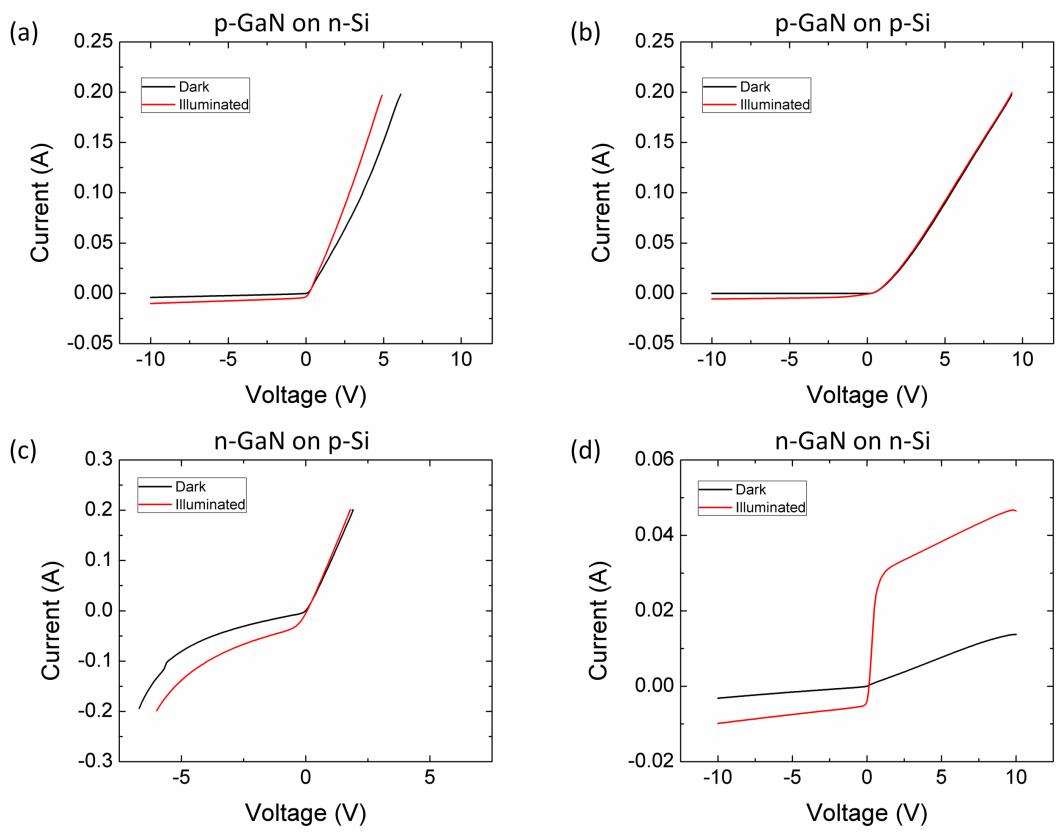

Figure 5.7: I-V curves for (a) p-GaN on n-Si, (b) p-GaN on p-Si, (c) n-GaN on p-Si, and (d) n-GaN on n-Si in the dark (black lines) and under illumination (red lines).

From Figure 5.7 it is clear that none of the GaN/Si heterojunctions had significant photovoltaic performance. While all of the devices showed some changes under illumination, the primary differences appear to be from photoconductance whereby the photogenerated carriers increase the conductivity of the material. The best photovoltaic performance came from the p-GaN on n-Si and p-GaN on p-Si devices, although they showed extremely low open-circuit voltage (V_{OC}) of 0.19 and 0.28 V, respectively. The maximum power output was on the order of ~1 mW/cm^2, resulting in a low conversion efficiency of approximately 0.25%. Worth noting however, is that the p-GaN on p-Si device shown in Figure 5.7(b) did have a clear diode-like rectifying behavior, albeit with

a very low turn-on voltage under 0.5 V. This particular device exhibited a strong blocking behavior in reverse bias, as shown in Figure 5.8, with a reverse bias breakdown voltage of approximately 170 V which shows great promise for future power device applications.

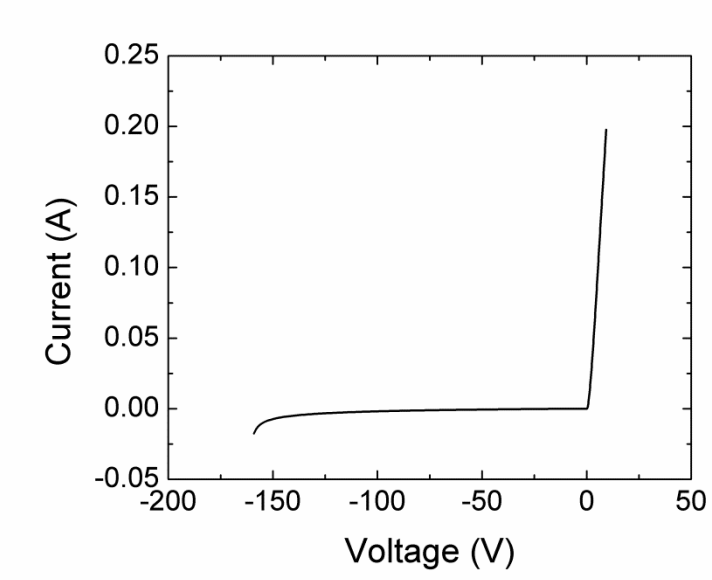

Figure 5.8: I-V curve for a p-GaN film on p-Si with clear rectifying behavior and a reverse bias breakdown voltage of ~170 V.

5.5 Nucleation from Aluminum Metal

5.5.1 Growth of Epitaxial (111)-Aluminum on (111)-Si

Given the rather poor GaN film quality demonstrated with the Ga droplet formation and subsequent regrowth, an alternative path was chosen for exploration. Previous growth of epitaxial aluminum on (111)-Si and (0001)-sapphire substrates was reported by MBE at low temperatures under 200°C with sub-nanometer RMS roughness, sharp interfaces, and high crystalline quality.[178] From this promising result, the same

growth sequence could be performed as in the gallium droplet formation experiment. In this case however, the aluminum melting point of ~660°C and Al-Si eutectic temperature of ~577°C allows a broader range of practical substrate temperatures since the liquid/solid phase can more easily be controlled compared to the 30°C melting temperature of gallium metal. Moreover, by cycling the temperature of the aluminum film on the Si substrate above the eutectic point, an aluminum-silicon melt will form with ~20-30% silicon composition. Then, a silicon liquid phase epitaxy (LPE) process can occur by reducing the substrate temperature, where the silicon precipitates out of the melt with a saturated concentration of aluminum on the order of 10^{17}-10^{18} cm^{-3}.[179] Since Al is a p-type dopant in Si, the LPE silicon layer would be highly p-type, thus forming either a p-n junction (if the substrate is n-type) or a front surface field (if the substrate is already p-type), and possibly improving the electrical contact to the MBE-grown GaN layer.

The growth of epitaxial (111)-Al on (111)-Si was performed using the same outgas procedure outlined above, except the substrate was then cooled down to the growth temperature of 150°C. After cool-down, the aluminum effusion cell was heated to provide an Al flux of approximately 1 Å/s. For the initial growth, a ~150 nm thick film was used to check that the growth conditions provided acceptable surface morphology and crystal quality of the epitaxial Al films. The XRD diffraction scan for this film is shown in Figure 5.9. The peaks at 28.46° and 58.88° are the diffraction peaks from the (111) and (222) reflections, respectively, of the face-centered cubic Si substrate with 5.45 Å lattice constant. The peaks at 38.49° and 82.5° are the (111) and (222) reflections, respectively, of the face-centered cubic aluminum film with lattice spacing of 4.05 Å, and the FWHM of the (111) rocking curve for the 150 nm thick AlN films was

623 arcsec. The film does show a weak peak at ~44.7° from the (200) reflection of Al, indicating some misoriented domains and/or slight polycrystalline structure, but the dominant peaks are those related to the (111) family.

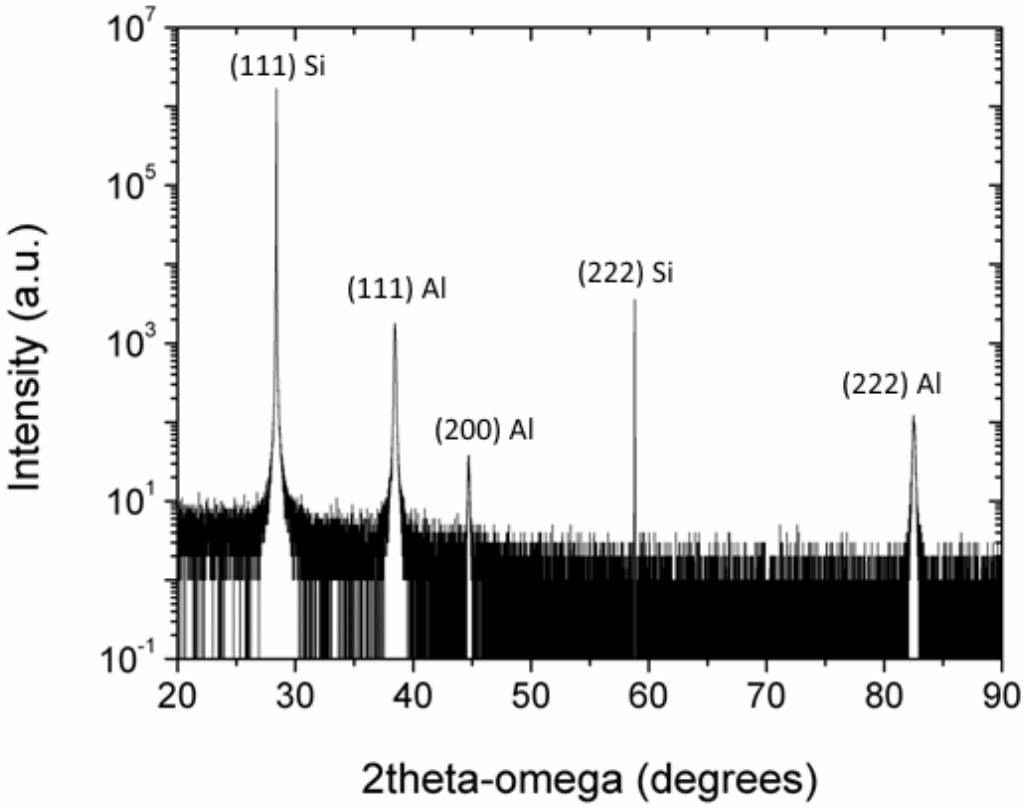

Figure 5.9: X-ray diffraction scan showing a highly textured Al film grown on Si, with the (111) and (222) peaks clearly visible for both materials.

Shown in Figure 5.10 is the resulting 5x5 μm AFM scan for this film which shows a non-coalesced and highly columnar structure. Upon further consideration, it was found that this particular silicon wafer was allowed to sit in a transfer chamber at a pressure of ~$1x10^{-8}$ Torr for several days before the growth was initiated. It is possible that the slow contamination of the substrate could have resulted in poor nucleation.

Discussion with the author of similar Al-on-Si work[178] confirmed this delay in growth as a common source of the poor surface morphology.

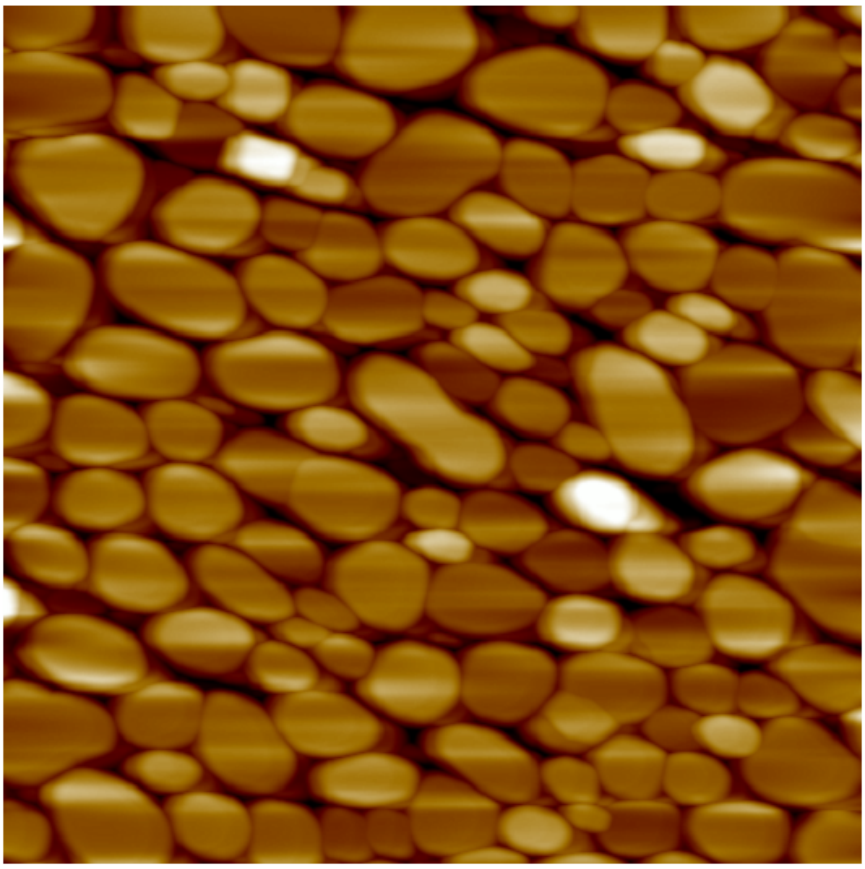

Figure 5.10: 5x5 μm AFM scan for a ~150 nm thick epitaxial Al film on (111)-Si showing columnar grains with RMS roughness of 14 nm. (Height scale = 108 nm)

The growth was then repeated using a new Si wafer for which the growth was initiated within 60 minutes of the wafer being loaded into the introductory chamber. This film, with a thickness of ~1 μm, showed dramatically improved surface quality as shown in Figure 5.11. This film exhibited a primarily smooth surface with clearly visible atomic steps and a 1.5 nm RMS roughness. Triangular features are present due to the (111) orientation of the aluminum cubic crystal structure resulting in a triangular/hexagonal

surface atomic arrangement.

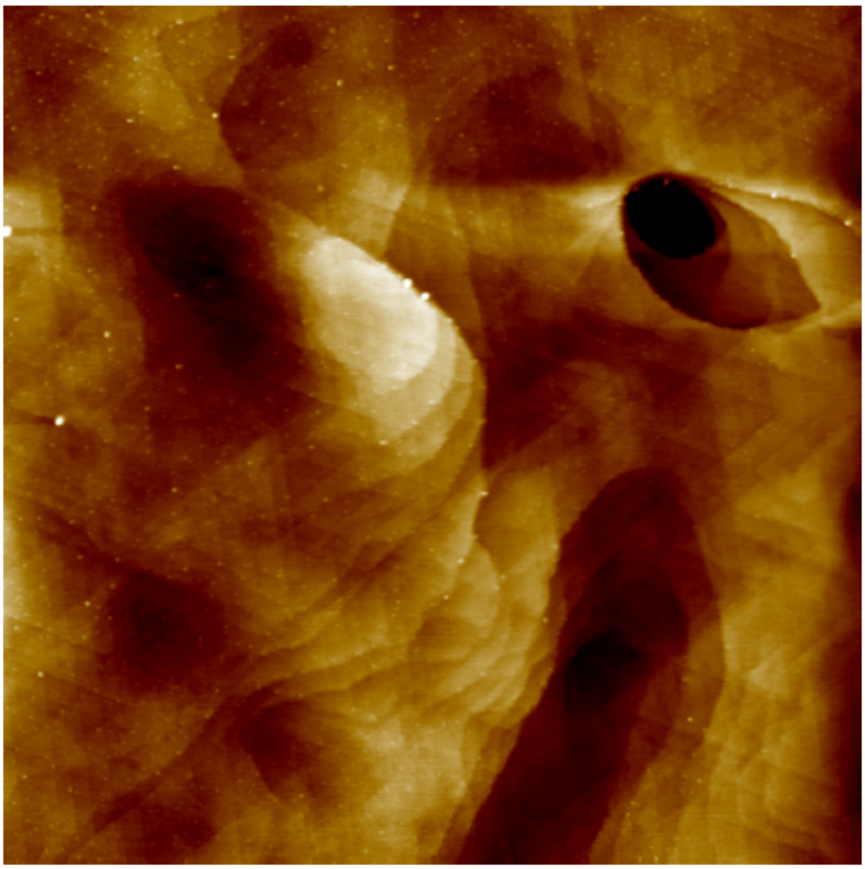

Figure 5.11: 5x5 µm AFM scan for 1 µm thick (111)-Al film using a Si wafer very soon after cleaning and loading into the chamber to prevent any contamination due to delayed growth. (Height scale = 11 nm, RMS roughness = 1.5 nm)

5.5.2 Growth of GaN from Al/Si

Given the improved surface features in Figure 5.11, the growth of GaN from the aluminum was next attempted, following a modified nucleation procedure. The epitaxial Al film was deposited on the clean Si substrate to a thickness of just 3 nm at 150°C after the same cleaning and outgassing process detailed above. The substrate temperature was then increased to 750°C, well above the eutectic temperature of 577°C, at which point the

aluminum film should melt and absorb ~25% Si into the liquid and form droplets due to surface tension. The substrate was then immediately cooled to 700°C in order to precipitate some of the aluminum-saturated Si from the melt. Next, the nitrogen plasma was ignited and the substrate was exposed to the plasma for 1 minute. Shown in Figure 5.12 are the RHEED images before (left) and after (right) the 1 minute nitridation at 700°C. Initially the RHEED started off dim due to the metal film/droplets on the surface. After 1 minute exposure to the nitrogen plasma, the RHEED pattern changed and brightened dramatically.

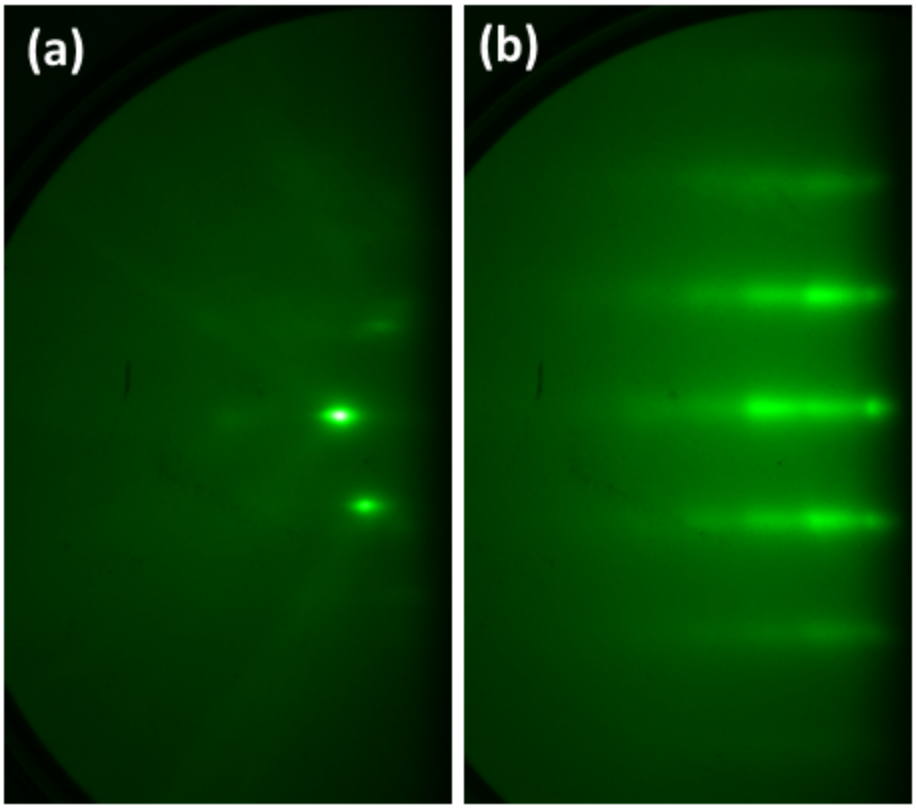

Figure 5.12: RHEED pattern of the Al-Si surface at 700°C before nitridation (left), and the same surface after 1 minute nitridation at 700°C (right).

The primarily streaky pattern in Figure 5.12(b) indicates a fairly smooth

crystalline surface, suggesting that the Al-Si melt crystallized during exposure to the nitrogen plasma, though the exact structure of AlN/SiN_x surface is unclear from the RHEED patterns. Even though a single RHEED spacing other was observed, at this elevated substrate temperature, the Si surface may have formed a crystalline SiN_x phase during the nitridation process as well. Regardless, this generally crystalline surface is dramatically different than that present after nitridation of the gallium droplets described above which showed a diffuse and amorphous surface leading to poor quality films with rough surfaces. Following the nitridation of the Al-Si melt, the substrate temperature was reduced to 600°C for GaN growth which was performed using the MME technique for a GaN thickness of 300 nm. Shown in Figure 5.13 are the RHEED patterns after just 20 seconds of GaN growth (left) and at the end of the growth (right) for the 300 nm thick film.

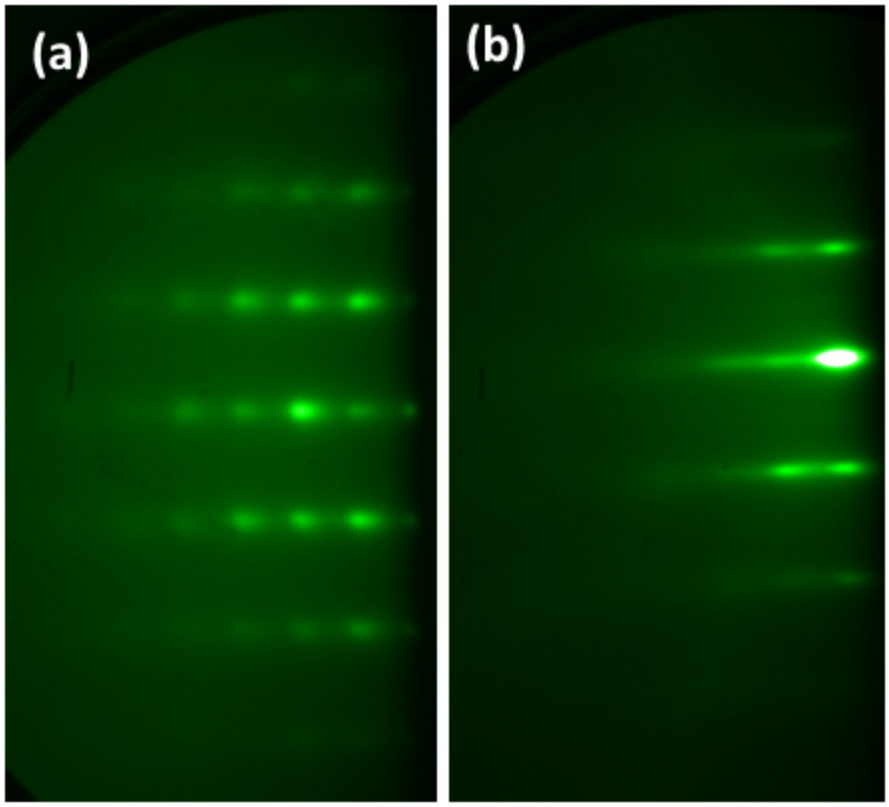

Figure 5.13: RHEED patterns after 20s of GaN growth (a), and at the end of the 300 nm thick film growth (b).

Owing to the more crystalline surface at the beginning of the GaN growth, the RHEED pattern even after just 20s of growth is immediately improved compared to the nucleation from Ga droplets and little or no polycrystalline concentric ring pattern is seen in Figure 5.13 (a). At the end of the growth in Figure 5.13 (b), the streaky pattern suggests a smoother surface compared to the growth from the Ga droplets above in Figure 5.4. The resulting 5x5 μm AFM surface scan is shown in Figure 5.14 below, which exhibits a rougher overall surface with RMS roughness of 6.0 nm. The surface roughness is dominated by large crystallites with diameters exceeding several hundred nanometers and heights of more than 30 nm. The surface features indicate that the film did not grow in a uniform sheet, but rather formed some large crystallites, possibly from

nitridation of the Al/Si liquid. In the flatter regions away from these large crystallites, the RMS surface roughness was ~2.0 nm.

Inspection of this film using SEM, shown in Figure 5.15, suggests that the film coalescence was not uniform for this 300 nm thick film, in agreement with the AFM morphology in Figure 5.14. The high density of small pits in Figure 5.15 as well as larger elongated pits and trenches means some improvement is still required to obtain a more uniform surface.

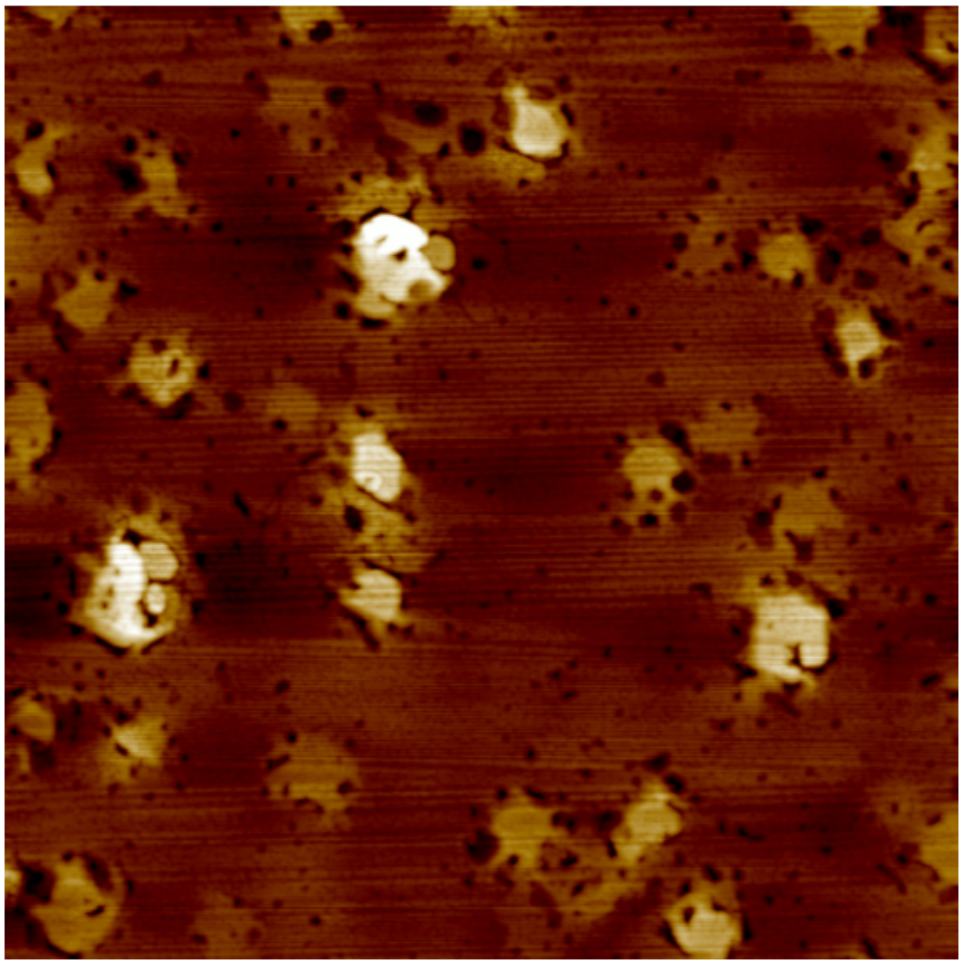

Figure 5.14: 5x5 μm AFM scan for a 300 nm thick GaN film nucleated from Al/Si. (Height scale = 55 nm, RMS roughness = 6.0 nm)

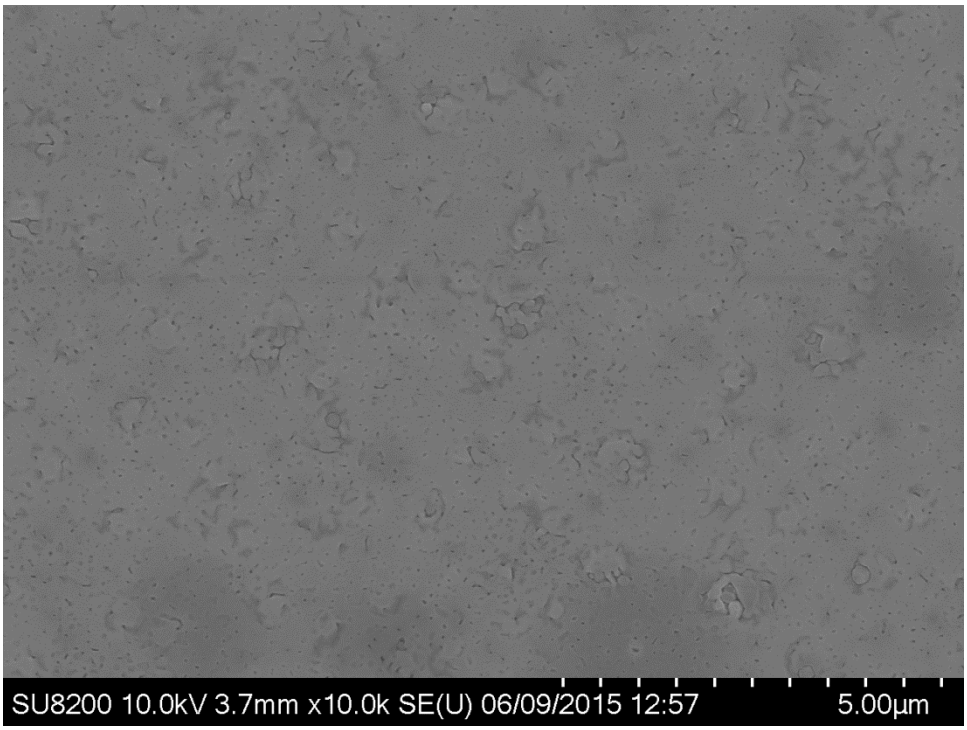

Figure 5.15: SEM image for 300 nm thick GaN film grown from the Al/Si nucleated surface.

To look for polycrystalline domains in the GaN film, a broad x-ray diffraction scan was performed as shown in Figure 5.16. From this scan, there are visible peaks for the (002) and (004) GaN reflections at 34.61° and 73.01°, respectively. The Si substrate peaks appear at 28.44° and 58.86° for the (111) and (222) reflections, respectively. No other peaks are visible, indicating that the GaN film is, at minimum, highly oriented in the c-axis, or possibly single crystal. The positioning of the (002) GaN reflection at 34.61° does indicate a significant degree of in-plane tensile stress since relaxed GaN should have occurred at 34.56°. Due to the coefficient of thermal expansion mismatch between GaN and Si causes, the GaN film shrinks more as it cools compared to the Si wafer resulting in a tensile stress. This, in turn, causes a compression of the *c* lattice parameter, shifting the (00ℓ) reflections to higher angle.

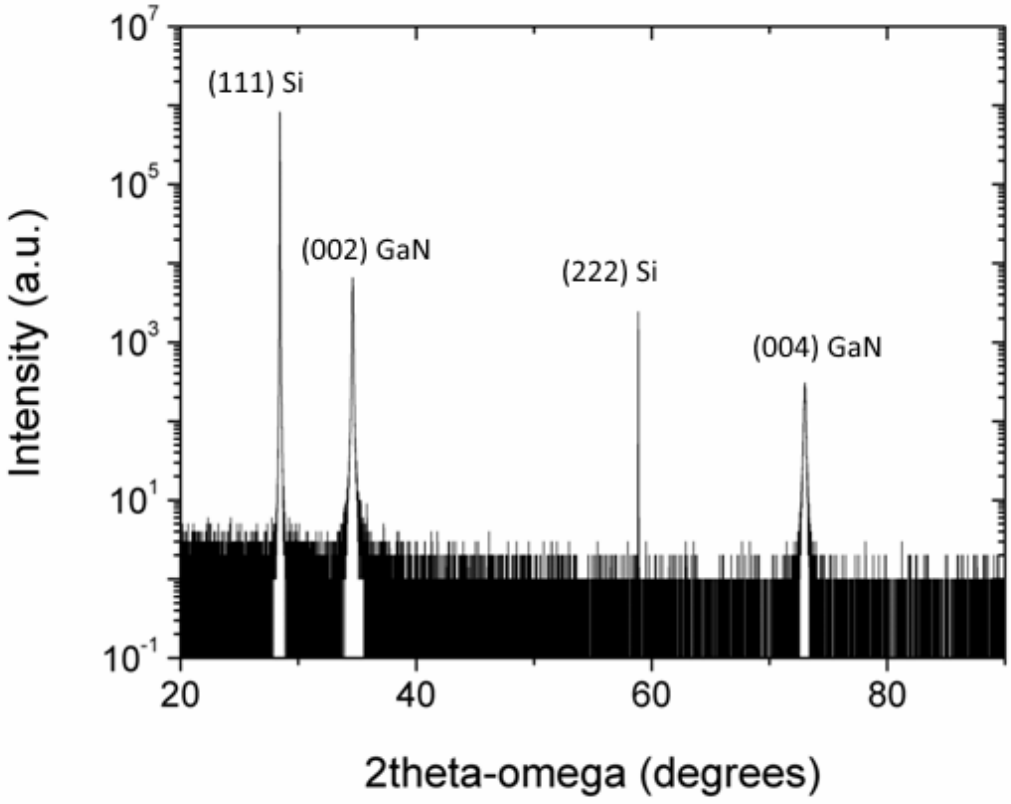

Figure 5.16: X-ray diffraction scan for 300 nm thick GaN film grown from Al/Si showing only the (002) and (004) GaN peaks, as well as the (111) and (222) Si peaks.

In addition to the diffraction scan in Figure 5.16, a rocking curve was performed about the (002) GaN peak which showed a FWHM of 2250 arcsec. While this rocking curve FWHM is much broader than those obtained from high quality GaN templates, this nonetheless represents a significant improvement compared to the >5000 arcsec rocking curves obtained from the films nucleated from Ga droplets as described previously. This provides definitive evidence of improved crystal quality, confirming the observations from the improved RHEED pattern.

While the diffraction scan in Figure 5.16 can give some information on the crystal

structure, a different scan is needed to determine whether the material is single crystal or simply a polycrystalline film with a primarily c-axis orientation. In this case, a pole figure is performed about the hexagonal GaN (112) reflection. The pole figure, as shown in Figure 5.17, is a polar coordinate plot of intensity versus a modified incident angle and rotation. The radius of the pole figure corresponds to an offset incident angle, or psi axis, ranging from 0° at the center to 90° at the outermost concentric circle. Each concentric circle in the pole figure denotes an increment of 30°. In performing this scan, several important determinations can be made, primarily the crystal symmetry and the presence of cubic phase inclusions in the film. In the case of a textured polycrystalline film where the grains are well-oriented to the c-axis but with severe or even complete rotational disordering, the pole figure would appear as a ring. The rotation of the sample would produce weak diffraction at all rotational angles since the grains are twisted relative to one another, resulting in a ring. In Figure 5.17, no such rings are observed, and several clear peaks are resolved. The outermost series of peaks labeled (a) shows 6-fold rotational symmetry at a radial (psi) angle of 74.7°. Analysis of the asymmetric diffraction angles indicate that these 6 peaks correspond to the hexagonal GaN (201) reflection with 6-fold rotational symmetry due to the hexagonal crystal structure. Similarly, the 6 peaks labeled (b) at a radial angle of 58.2° are from the hexagonal GaN (112) reflection. Finally, a third family of peaks labeled (c) is resolved at a slightly lower radial angle of 54.7°, but there are only 3 peaks in this group compared to the 6 peaks observed for (a) and (b). These peaks at 54.7° correspond to the Si (400) reflection which, due to the cubic crystal structure, only has 3-fold rotational symmetry. No other peaks are present in the pole figure, no cubic inclusions are seen, and no diffracted rings

are observed which suggests the film is primarily single crystal, c-plane wurtzite GaN.

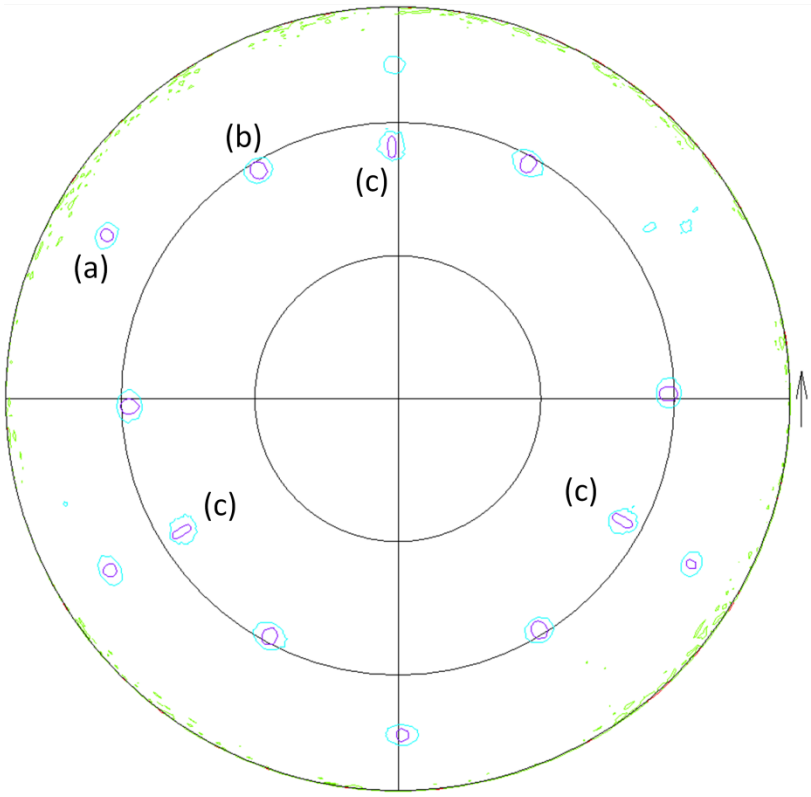

Figure 5.17: Pole figure of 300 nm thick GaN film nucleated on Al/Si with peaks visible for (a) 6-fold hexagonal GaN (201) reflections, (b) 6-fold hexagonal GaN (112) reflections, and (c) 3-fold cubic Si (400) reflections.

5.5.3 2-Step GaN Growth from Al/Si

While the improvement in crystal quality using the Al/Si nucleation was substantial, the film was nonetheless highly defective compared to films grown on sapphire. In an effort to improve the crystal quality further, a thicker film was grown using the same Al/Si surface for nucleation, but using a 300 nm thick N-rich GaN layer followed by a 700 nm thick regrowth by metal-rich MME for a total GaN thickness of ~1 μm. This combination is expected to result in improved crystal quality while maintaining

smooth surfaces and is based on prior work.[180] The rougher surface of the N-rich was chosen in order to bend dislocations resulting in more dislocation annihilation and, thus, reducing threading dislocation density, while the metal-rich layer should recover a smooth surface desirable for devices. The RHEED patterns in Figure 5.18 taken at the end of these steps qualitatively confirms these expectations, where the N-rich growth results in a rough spotty pattern while the metal-rich MME growth substantially smoothens the GaN film leading to a streaky pattern. The GaN (002) XRD rocking curve also shows an improvement in the crystal quality of this 2-step GaN film with a FWHM of 1750 arcsec, compared to the 2250 arcsec for the thinner single-step 300 nm MME film.

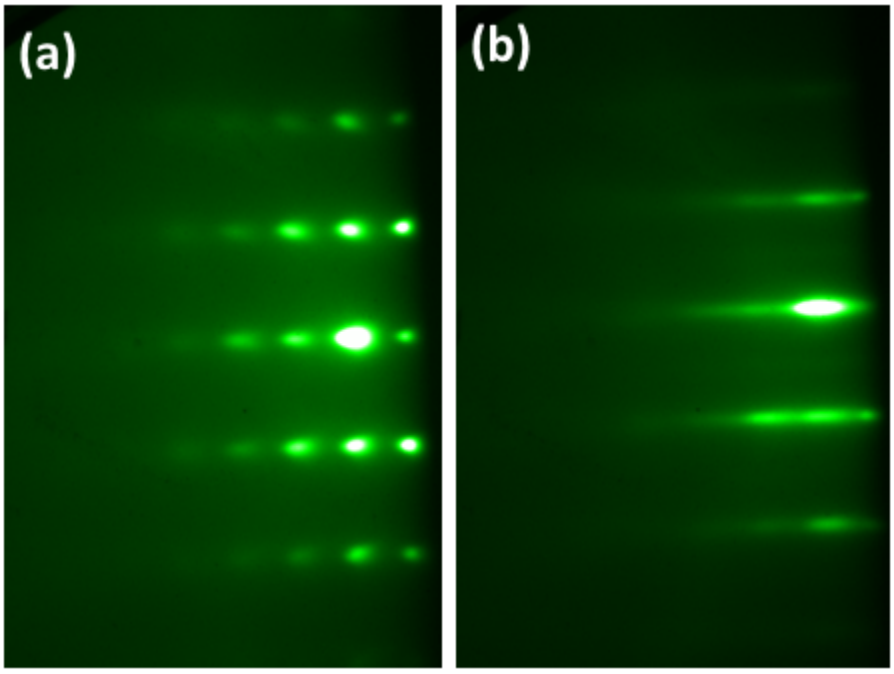

Figure 5.18: RHEED images taken at the end of the 300 nm thick N-rich step (a) and at the end of the subsequent 700 nm thick metal-rich MME step (b) for the 2-step GaN film grown nucleated from Al/Si.

The resulting 5x5 μm AFM scan for this film is shown in Figure 5.19, which exhibits a modestly improved RMS roughness of 3.3 nm compared to the 3.7 nm for the film nucleated from Ga droplets in Figure 5.6. The thicker 2-step GaN film shows improved coalescence, and in the flatter regions of Figure 5.19 away from the large pits the surface roughness is as low as 0.8 nm which is similar to high quality MBE-grown films on GaN templates (see Figure 4.2) or sapphire.

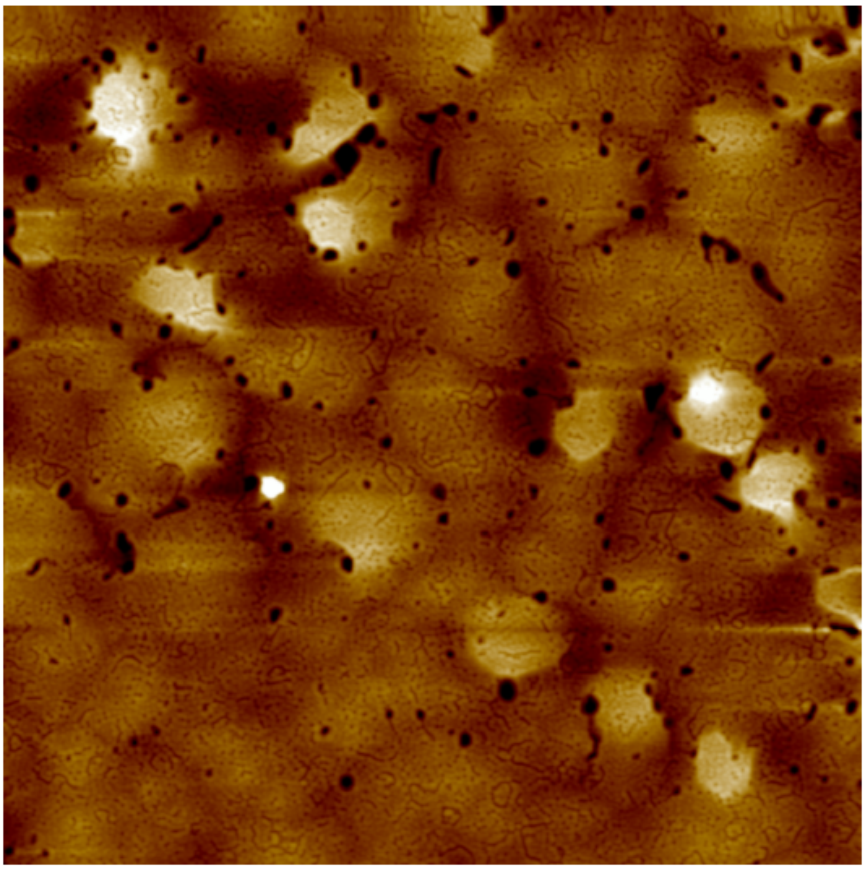

Figure 5.19: 5x5 μm AFM scan for a 1μm thick GaN film nucleated from Al/Si consisting of 300 nm of N-rich growth followed by 700 nm of metal-rich MME growth. (Height scale = 29 nm, RMS roughness = 3.4 nm)

While the AFM morphology of the film showed slight improvements to the general surface roughness, it is also clear that the film coalescence is substantially

improved with this thicker film using a 2-step growth procedure. The density of deep, elongated trenches and many of the pits shown in Figure 5.14 are significantly reduced using this technique, although they are not completely eliminated. However, as shown in Figure 5.20, the larger-scale surface images show several undesirable features including film cracking and sparse bright spots. The film cracking is due to excessive tensile stress in this substantially thicker film during cool-down from the growth temperature of 600°C. While the lower growth temperature of MBE compared to MOCVD should reduce the tendency towards cracking, it is clear that in this case the temperature alone was insufficient to prevent cracking entirely for this thicker film.

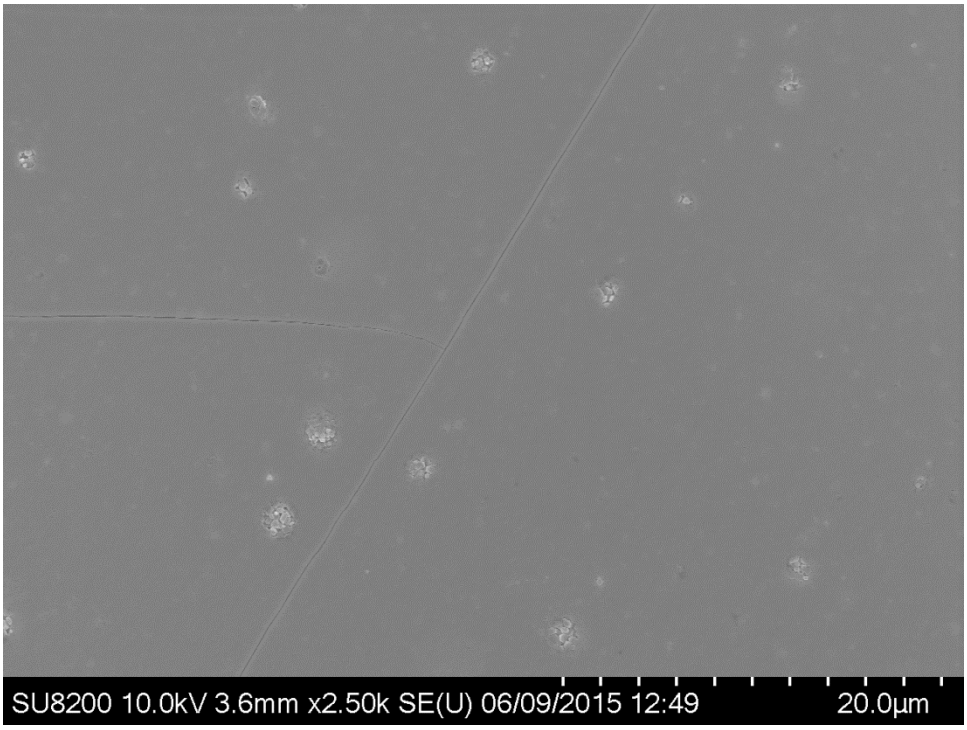

Figure 5.20: SEM capture for the 1 µm thick, 2-step GaN grown from Al/Si with material clusters and cracks in the film.

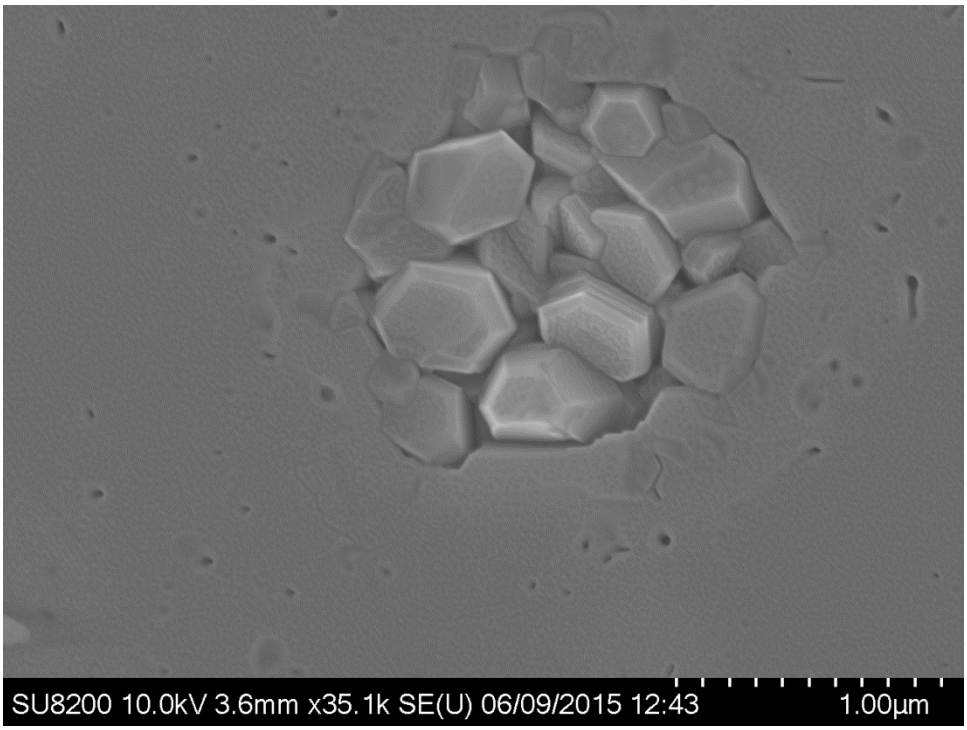

Figure 5.21: SEM detail of bright clusters from Figure 5.20 showing formation of crystallites with multiple orientations.

Focusing more closely on the bright clusters from Figure 5.20, one can see some interesting surface features. Most of these features are located closer to the edge of the 2" wafer. Shown in Figure 5.21 is a close-up of these bright spots at higher magnification which shows the formation of hexagonal crystallites with diameters on the order of ~300 nm, while the overall diameter of the crystallite "pool" is approximately 1.5 µm. A cross-sectional SEM image was also acquired for a cleaved piece of this sample, which is shown in Figure 5.22. In this image, the interface between the GaN film and the underlying Si wafer appears to be clean and sharp which is desirable for a heterojunction device. There is no apparent melt-back etching in this image or any other part of this cleaved sample, which would be catastrophic for any device applications. However, a cleaved sample offers limited range for finding the crystallite pools where

detrimental melt-back etching seems more likely to exist. Only by cleaving directly through one of these pools could the SEM image provide conclusive evidence as to the presence of melt-back etching for this nucleation technique. Thus, while the cross-sectional SEM shows a clean interface which is quite promising, it is not necessarily conclusive evidence that melt-back etching is not occurring in other areas.

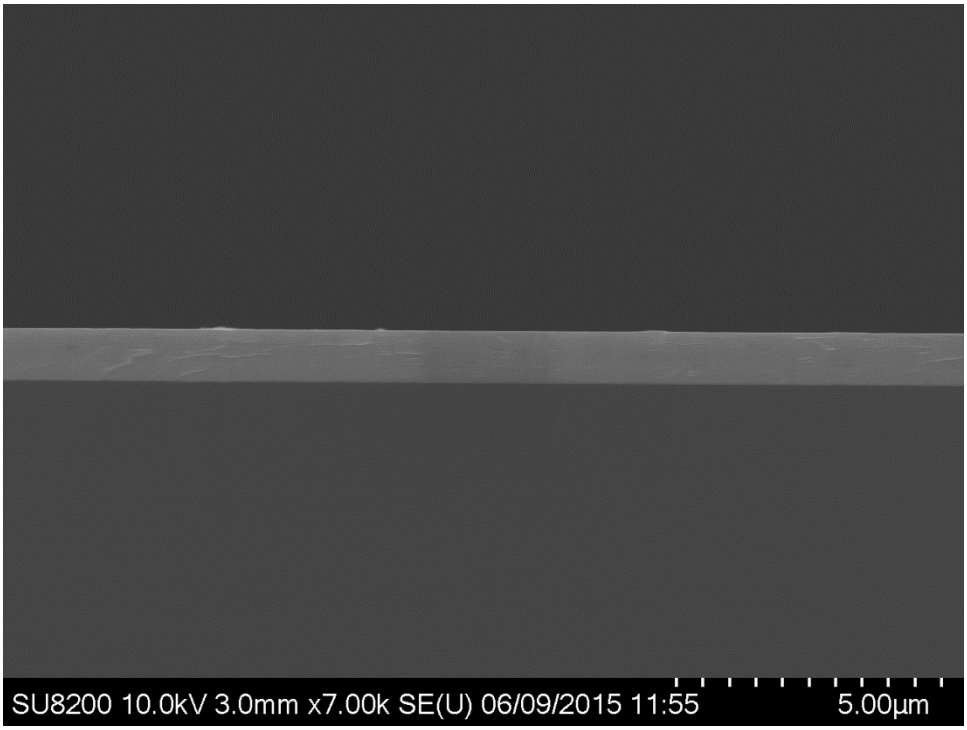

Figure 5.22: Cross-sectional SEM image of GaN film (bright) on Si (dark) nucleated from Al/Si.

Given the nucleation procedure used here, it is possible that the Al/Si melt droplets did not form clean single crystals during the nitridation, and instead formed several polycrystalline domains in the location of each droplet. If such is the case, then subsequent GaN growth from those domains would similarly tend towards polycrystalline

structure as it templates onto the underlying layer. Moreover, at a temperature of 700°C, the Al droplets are expected to contain on the order of 21% Si, forming an aluminum silicide instead of just silicon-doped aluminum.[181] As such, exposing these droplets to the nitrogen plasma likely didn't form the desired wurtzite AlN phase, but rather some mixed AlN/SiN_x material with an unknown crystal structure or poor crystal structure altogether.

In order to test the electrical properties of the heterojunction device resulting from this Al-Si nucleation process, two unintentionally-doped GaN films were tested on p-type and n-type float zone silicon wafers. Due to the growth being on silicon, the unintentionally doped GaN likely results in n-type GaN from out-diffusion of silicon into the growing film. The GaN growth consisted of a single unintentionally-doped 300 nm thick MME-grown film, as shown in Figure 5.14 and Figure 5.15. Full coverage metal contacts were evaporated on both sides of the wafer: Ti/Al/Ti/Au (30/100/30/50 nm) on the front GaN surface, and 100 nm Au on the rear Si surface. Shown in Figure 5.23 are the resulting I-V curves for these devices, with the u-GaN/p-Si shown in black and the u-GaN/n-Si shown in red.

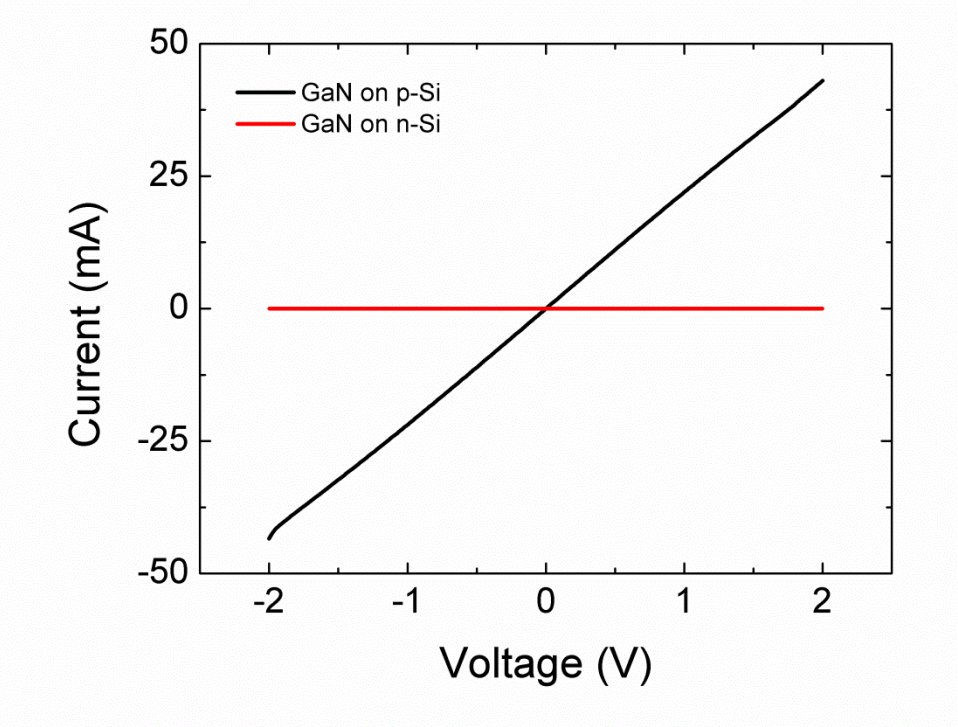

Figure 5.23: I-V curves for 1x2 mm GaN/Si heterojunction devices using the Al/Si nucleation procedure: u-GaN/p-Si (black) and u-GaN/n-Si (red).

From these I-V curves it is clear that the GaN/p-Si heterojunction was conductive and linear, indicating a nearly ohmic contact characteristic with a series resistance of ~47 Ω. On the contrary, the GaN/n-Si heterojunction was highly resistive with a peak current of just 13 μA at +2 V bias, more than 3 orders of magnitude smaller than the 43 mA at +2 V for the GaN/p-Si device. While PV performance has not been fully tested, the Al/Si nucleation technique for a p-type Si substrate shows great promise for the realization of a III-nitride on Si tandem solar cell with an ohmic tunnel junction connecting the two sub-cells.

5.6 Conclusion

In summary, the growth of III-nitride films on Si substrates has been demonstrated with the goal of using the underlying Si substrate as the absorbing region in a solar cell structure. The vertically conducting device structure necessitates careful design in order to prevent current blocking at the heterointerface, contrary to typical III-nitride growth on Si. To achieve this vertical conduction, several nucleation and growth techniques were employed by pre-exposing the surface to group III sources. Pre-exposure to a few monolayers of metallic gallium, followed by nitridation, resulted in a diffuse RHEED pattern indicating a primarily amorphous surface. Growth of GaN using this nucleation procedure resulted in extremely poor quality GaN and a slight polycrystalline contribution in the RHEED patterns. Nonetheless, basic devices were fabricated which showed some photovoltaic behavior with up to J_{SC} of up to 58 mA/cm^2. Furthermore, a p-GaN/p-Si heterojunction device exhibited highly rectifying diode behavior with turn-on voltage under 0.5 V and reverse bias breakdown voltage of ~170 V.

As an alternative to gallium, low-temperature pre-exposure of aluminum was similarly explored. Initially, the growth of epitaxial (111)-oriented aluminum films were demonstrated at a growth temperature of 150°C. From this, it was found that cleaning and surface preparation for the Si substrates were critical to achieving good quality interfaces and films. This procedure of low-temperature aluminum deposition was then modified for GaN growth by heating the Al film above the eutectic temperature and melting point, followed by a nitridation to crystallize the liquid Al/Si mixture. The resulting RHEED images indicated the surface was drastically more crystalline compared

to the Ga droplet nucleation procedure, and the resulting GaN films were also of higher quality as determined by XRD. Device structures were fabricated using the Al/Si nucleation for UID GaN films on n- and p-type Si. The u-GaN/n-Si structure was resistive, while the u-GaN/p-Si device showed a highly linear I-V curve which is promising for future GaN/Si heterojunction device applications.

Table 5.1: Summary of this work compared to existing state-of-the-art for GaN films grown on Si substrates. [44, 45, 182-188]

Author	**Technique**	**Buffer**	**(002) RC FWHM (arcsec)**	**RMS Roughness (nm)**	**Conductive?**
Irie *et al.[189]*	MOCVD	Varied thickness of AlN and InAlN	900 – 1200	--	Rectifying for ultra-thin AlN, otherwise inferred resistive
Sobanska *et al.[45]*	PAMBE	AlN	--	2.9	Inferred resistive
Semond *et al.[44]*	NH_3 MBE	AlN	1020	3	Inferred resistive
Cordier *et al.[182]*	NH_3 MBE	AlN	700 – 1350	5	Inferred resistive
Louarn *et al.[183]*	NH_3 MBE	AlN	800 – 1100	5.5	Inferred resistive
Lu *et al.[185]*	MOCVD	Thin AlN	900 – 1800	1.3	Possibly conductive
Ma *et al.[186]*	MOCVD	AlN, AlN/GaN superlattice	400 – 600	0.4 – 1	Inferred resistive
This work	PAMBE	None, or ultra-thin AlN	1710	3.4 – 6.5	Conductive, rectifying, or resistive
Xu *et al.[187]*	PAMBE	None	6500	--	Conductive or rectifying
Kumar *et*	PAMBE	None	2500 – 3300	3.9 – 5.3	Inferred conductive

al.[188]					
Lu *et al.[185]*	MOCVD	None	4800	--	Inferred conductive
Ager *et al.[190]*	PAMBE	None or AlN	--	--	Conductive or rectifying

Shown in Table 5.1 is a comparison of the results obtained from this preliminary work compared to some state-of-the-art results achieved in the literature. It is often challenging to draw direct comparisons since this type of vertical conduction is not often tested. Thus, the terms "inferred resistive" or "inferred conductive" are used here to denote the nature of the heterostructure based on the presence of, or lack of, thick insulating buffer layers. Highly optimized high-temperature MOCVD growth like that in Ma *et al.* [186] demonstrates excellent crystal quality, but the use of complex insulating buffer layers makes it unsuitable for this PV application. While the work presented here is certainly not a perfect solution to the issue of defects resulting from GaN grown on Si, marked improvement in the structural quality was obtained while simultaneously achieving a conductive interface to Si for the Al/Si nucleation method.

CHAPTER 6: GROWTH OF III-NITRIDES ON A NOVEL SUBSTRATE: ALEXANDRITE ($BeAl_2O_4$)

6.1 Introduction

Lack of a suitable substrate has long plagued the III-nitride material system, resulting in high defect densities. Significant research has been performed to improve material quality through buffer layers, superlattices, or lateral overgrowth techniques. Nonetheless, the defect densities remain high compared to traditional III-V semiconductors. Recently, a unique relaxation mechanism has been discovered in highly lattice mismatched III-nitride heteroepitaxial films.[191] It was proposed that the extreme lattice mismatch between GaN and $In_xGa_{1-x}N$ ($x > 0.6$) allowed the material to spontaneously relax upon nucleation. Because the critical thickness of the InGaN film on the GaN substrate was on the order of 1 monolayer, the film was unable to grow to any significant thickness in a strained manner before it relaxed. Thus, the film relaxed in the only direction it was able – laterally – pinning dislocations to the interface in a lateral misfit array instead of traditional threading dislocations more commonly seen in III-nitrides. This misfit array resulted in a dramatic improvement in material quality, recovering a strong photoluminescence signal which was absent for InGaN films below 60% indium fraction.[191] Seeing such a promising result exploiting lattice mismatch rather than avoiding it, the question arises if this type of result can be repeated using other substrate/film combinations. The purpose of this study is to use an alternative highly lattice-mismatched substrate in order to explore if this spontaneous relaxation mechanism demonstrated by Fischer *et al.* can be achieved with GaN, reducing defect

densities and improving material quality. In this case, the substrate chosen is a laser crystal known as alexandrite, $BeAl_2O_4$.

6.2 Properties of Alexandrite ($BeAl_2O_4$)

Alexandrite possesses an orthorhombic crystal structure with *a,b,* and *c* lattice constants of 5.476 Å, 9.404 Å, and 4.427 Å. While the chemical formula is similar to spinel ($MgAl_2O_4$), the crystal structures of the two materials are very different since spinel is a cubic crystal. Shown in Table 6.1 are some select properties of the alexandrite material used as substrates in this study.[192]

Table 6.1: Select properties of alexandrite, $BeAl_2O_4$

Formula	$BeAl_2O_4$
Crystal Structure	Orthorhombic
Space Group	*Pnma*
Lattice Constants	a = 5.476 Å, b = 9.404 Å, c = 4.427 Å
Melting Point	1870°C
Mohs Hardness	~8.5
Thermal Conductivity	0.23 W/cm-K
Doping Concentration (Chromium)	0.1 – 0.2 at % Cr^{3+}
Coefficient of Thermal Expansion	$\|\|a = 5.9 \times 10^{-6}$ K^{-1} $\|\|b = 6.1 \times 10^{-6}$ K^{-1} $\|\|c = 6.7 \times 10^{-6}$ K^{-1}
Refractive Index	~1.74

Alexandrite is a laser crystal with applications in the tattoo removal and laser hair removal industries. It possesses a tunable infrared emission wavelength in the 700-800 nm range which can be selected by modifying the crystal temperature.[192] The chromium dopant in the crystal, on the order of 0.1 to 0.2 atomic percent, allows for multiple optical transitions in the visible and near-infrared ranges. Traditional alexandrite lasers are pumped using flash lamps or arc lamps which emit broad band

light. Select wavelengths are absorbed into the various bands in the crystal, exciting carriers to higher energy states, as shown in Figure 6.1. The excited electrons can relax to lower energy states through photon emission, which can result in lasing at sufficiently high pumping conditions. Phonon interaction results in a modification of the emission/absorption energies, allowing a tunable emission wavelength as shown by the red 700-820 nm transition in Figure 6.1.[193]

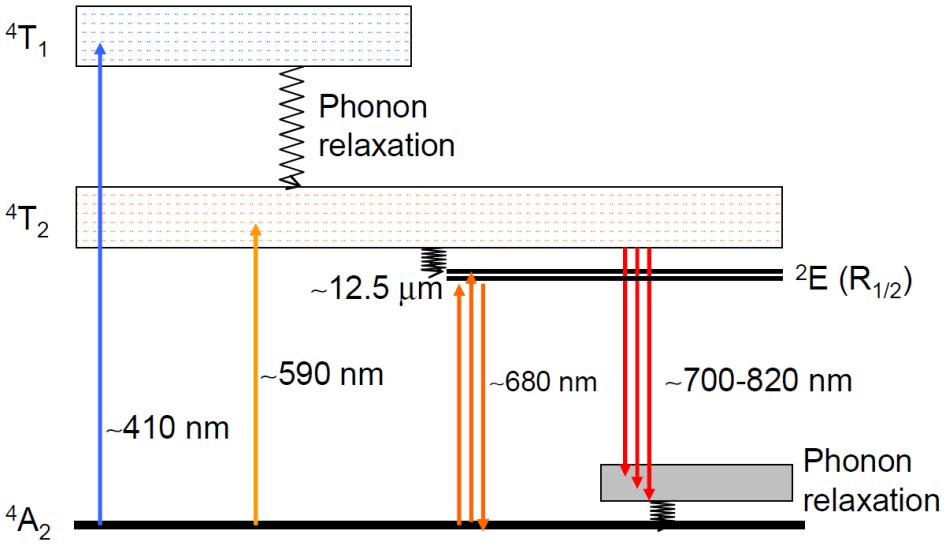

Figure 6.1: Schematic of optical transition bands in chromium-doped alexandrite crystals.[193]

6.3 Integrated Diode-Pumped Laser System: III-Nitride on Alexandrite

While flash lamps and arc lamps are a very common pumping mechanism for solid state lasers, they are generally inefficient owing to their broad emission wavelength, of which only a small portion is absorbed by the crystal. To improve upon this traditional design, a diode-pumped system can be used wherein another laser is used to pump the

alexandrite crystal.[194] This pump laser will have a carefully selected emission wavelength which is chosen to align with the absorption band of the alexandrite crystal. This system is much more efficient and compact compared to flash lamp pumping, which could be potentially viable for a portable system.

Typically, alexandrite lasers crystals are on the order of several square millimeters in cross-sectional area with lengths exceeding several centimeters. It may be possible to shrink such a system using an integrated epitaxial approach wherein a high power LED structure is grown epitaxially on the alexandrite. Given the 410 nm absorption line in alexandrite as shown in Figure 6.1, the III-nitride system could potentially fit for this type of integrated system, where the alexandrite crystal is optically pumped by an efficient GaN-based LED. The LED emission wavelength would be tuned to 410 nm based on the indium mole fraction in the InGaN quantum well. If a III-nitride film could be grown with sufficient quality on the alexandrite substrate to produce a high efficiency LED, then an extremely compact, integrated diode-pumped alexandrite laser might be possible.

6.4 Experimental Procedure

All films were grown in a Riber 32 MBE system (base pressure less than $1x10^{-10}$ Torr) equipped with a Veeco gallium SUMO® cell, a cold-lip aluminum cell, standard effusion cells for indium and silicon, and a Veeco corrosive series valved cracker for magnesium. The cracker temperatures, when applicable, were 295°C for the bulk and 900°C for the tip, and the valve position was 240 mils. Nitrogen was supplied by a Veeco Unibulb RF plasma operating at 13.56 MHz with 350W of RF power and 1.3 sccm

of nitrogen flow. All substrates in this experiment were commercially available (001)-oriented single-side polished alexandrite ($BeAl_2O_4:Cr^{3+}$) substrates (SurfaceNet GmbH, Germany). The substrate dimensions were 10x10 mm with 500 μm thickness, and the chromium doping level was approximately 0.1 to 0.2 atomic percent. All substrates were backside sputtered with approximately 2 μm of tantalum to promote radiative absorption from the substrate heater and to ensure uniform heat spreading. The substrates were ultrasonically degreased for 30 minutes each in trichloroethylene, acetone, methanol, and isopropanol. The alexandrite samples were then rinsed in deionized water and dried with nitrogen before being loaded into an introductory vacuum chamber where they were outgassed at 150°C for 30 minutes. Various outgas, nitridation, and buffering procedures were performed in the growth chamber for a series of four samples as shown in Table 6.2.

Table 6.2: Nucleation and growth conditions for III-nitride films grown on alexandrite ($BeAl_2O_4$) substrates.

	Sample A	***Sample B***	***Sample C***	***Sample D***
Outgas	600°C – 10 mins	600°C – 10 mins	850°C – 10 mins	850°C – 10 mins
Nitridation	none	200°C – 60 mins	none	200°C – 60 mins
Buffer	none	none	1-step AlN	2-step AlN, and GaN anneal

Unless otherwise noted, the nitride films were grown using the metal-modulated epitaxy technique with a shutter scheme of 10s open / 10s closed and a III/V ratio of approximately 1.8. The AlN buffers, where applicable, were grown for a thickness of approximately 150 nm. The thick GaN films for each of the four samples was grown at 600°C for a thickness of approximately 1.6 μm, and all films in samples A through D in

Table 6.2 were unintentionally doped. Reflection high energy electron diffraction (RHEED) was used throughout the growth procedure to monitor the growth surface, and atomic force microscopy (AFM) was performed post-growth using a Veeco Dimension 3100 to determine the final surface morphology. To characterize the phase, orientation, and quality of the nitride films, x-ray diffraction (XRD) was performed using a Philips X'Pert Pro MRD. Optical properties were investigated by photoluminescence spectroscopy (PL) at room temperature and at 77K using a Spex 1702 spectrometer with 325 nm excitation from a HeCd laser. Electrical properties of the nitride films, where applicable, were determined by Hall effect measurements using either a 0.3T fixed magnet or a 1.5T electromagnet with traditional indium dot contacts.

6.5 RHEED and AFM surface morphology

Shown in Figure 6.2 are several representative RHEED images of the bare alexandrite substrate. Three distinct patterns arise from the orthorhombic crystal structure which has three two-fold rotation axes of symmetry about the c-axis. These patterns remained unchanged with increasing temperature up to 850°C.

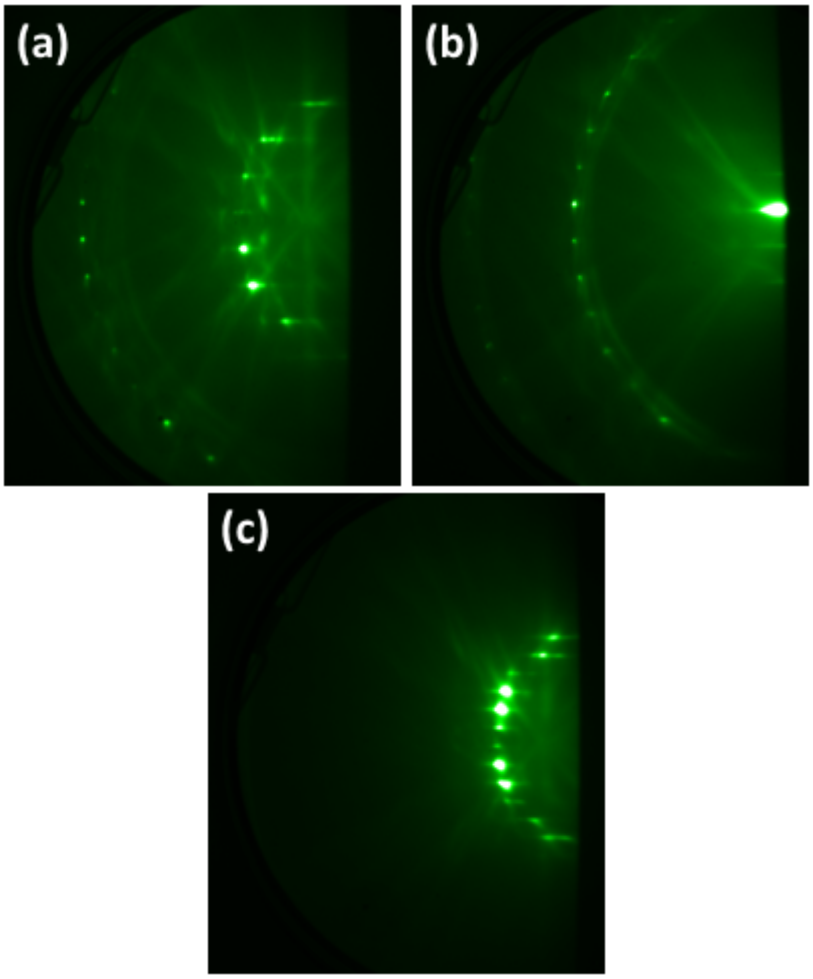

Figure 6.2: RHEED images of the bare alexandrite substrates at various rotational angles before high temperature outgas and growth.

In the case of sample A, no further surface preparation was performed before growth except for a 10 minute outgas at the GaN growth temperature of 600°C. Growth was initiated under metal-rich conditions using MME and the growth was continued for 2.5 hours with the resulting film thickness of approximately 1.6 μm. The RHEED patterns for the GaN film after ~20 seconds of growth and at the end of growth can be seen in Figure 6.3 along with a 5x5 μm AFM image. In the left RHEED image, a mixed streaky and spotty pattern can be seen with cubic and hexagonal features, most likely due to the lattice and crystal structure mismatch. This mixed pattern quickly evolved into a

streaky pattern within 1-2 minutes and showed a 2x2 reconstruction after approximately 15 minutes of growth. At the end of growth, a strong 2x2 reconstruction in the RHEED image (middle) indicates that the final film was smooth and 2-dimensional resulting in a flat surface. While the overall surface morphology is somewhat grainy and without obvious atomic steps, the root mean square (RMS) roughness of sample A, as shown in Figure 6.3(c), is just 0.7 nm which represents a sufficiently smooth surface for use in devices.

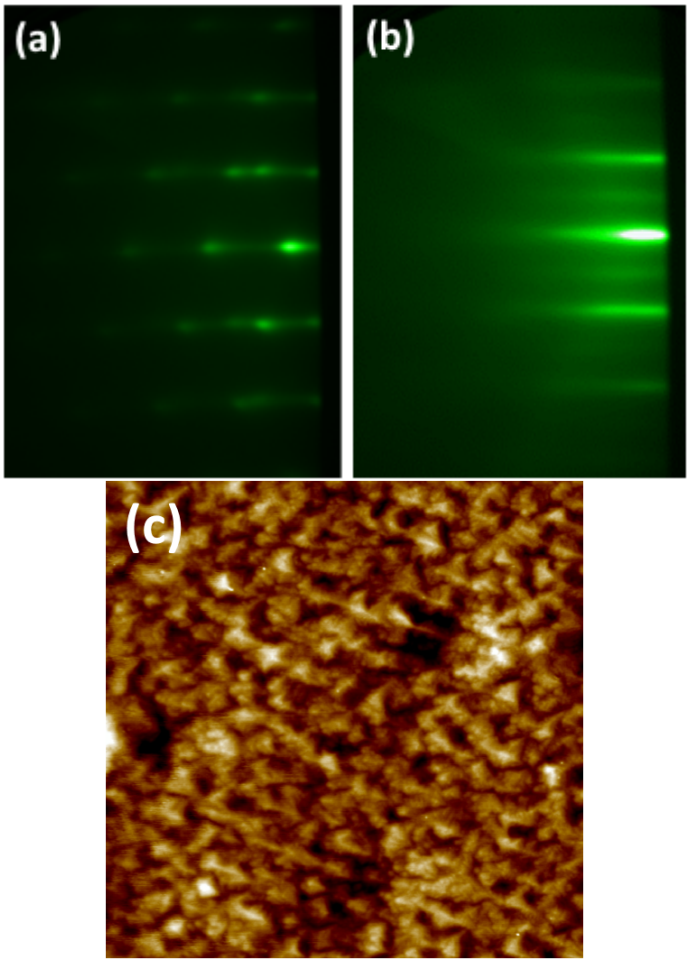

Figure 6.3: (a) RHEED image taken after the first shutter cycle (~20s). (b) RHEED image at the end of growth for sample A. (c) 5x5 μm AFM image (height scale = 5 nm) for sample A with RMS roughness of 0.7 nm.

Taking a lesson from MBE growth of GaN on sapphire, a low-temperature nitridation step was performed at 200°C for 60 minutes for sample B. In the case of sapphire, the nitridation converts the first 1-2 layers of Al_2O_3 into AlN, giving a better template for further nitride growth.[88, 91, 92] In addition, films grown on nitrided sapphire typically show better polarity control with fewer inversion domains.[85-87] The low nitridation temperature limits the formation of oxy-nitride complexes, thereby reducing or eliminating the undesirable yellow luminescence often seen in the PL spectrum with high-temperature nitridation. As shown in Figure 6.4(a), the RHEED pattern after nitridation was changed from the bare alexandrite patterns in Figure 6.2, but unlike nitridation of sapphire there was no distinct AlN pattern. After ~20s of growth, shown in Figure 6.4(b), the RHEED pattern indicates the presence of cubic and hexagonal phases at the early stages of growth similar to sample A. By the end of growth in Figure 6.4(c) a 2x2 reconstruction clearly emerges but some spottiness can also be seen indicating a slightly rougher surface. The AFM for sample B in Figure 6.4(d) is qualitatively similar to sample A with a slight increase in surface roughness to 0.8 nm RMS.

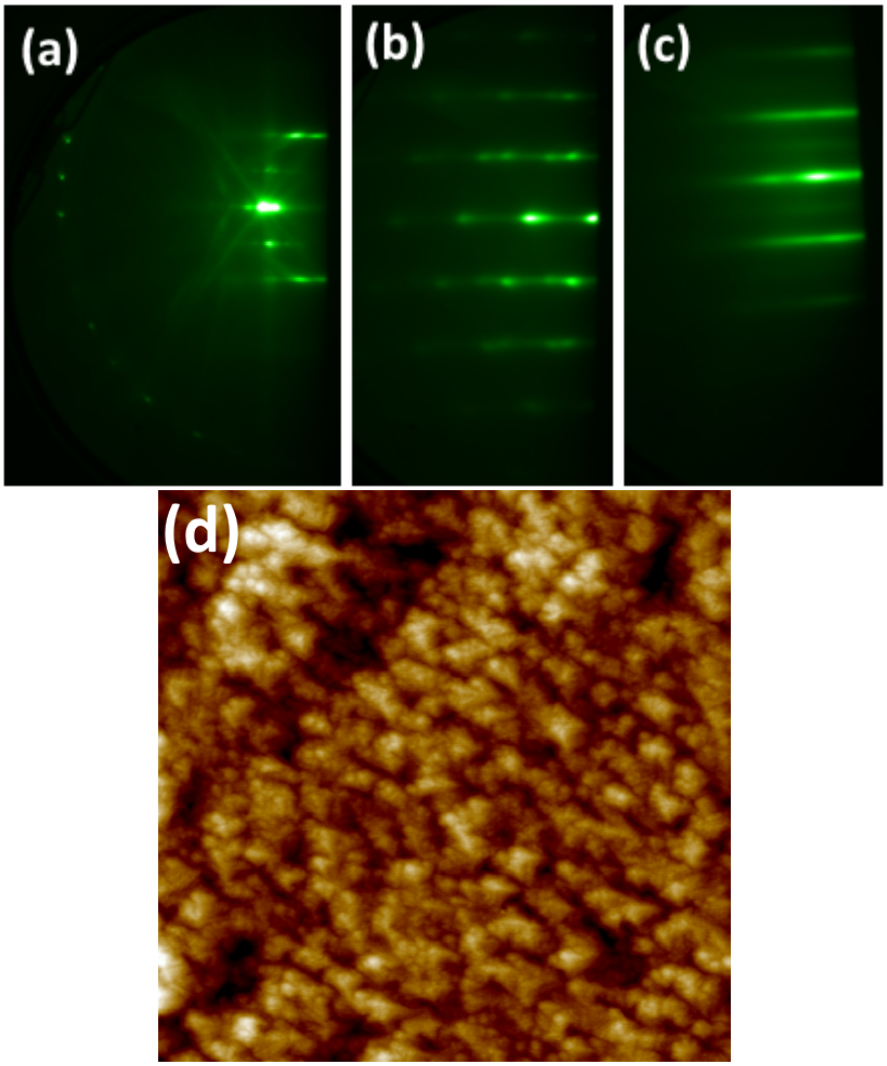

Figure 6.4: RHEED images for sample B - (a) after 60 minute nitridation at 200°C, (b) after first shutter cycle (~20s), (c) at the end of growth, and (d) 5x5 µm AFM scan with RMS roughness of 0.8 nm (height scale = 6 nm).

For sample C, AlN was used as a buffer layer with a thickness of approximately 150 nm also grown by MME under metal-rich conditions. AlN has also been shown to improve the quality of subsequent GaN films by controlling polarity and providing a closer template for GaN growth. In this case, no nitridation of the substrate was performed, although the outgas temperature was increased to 850°C to account for the

higher growth temperature of AlN (850°C) as compared to GaN (600°C).

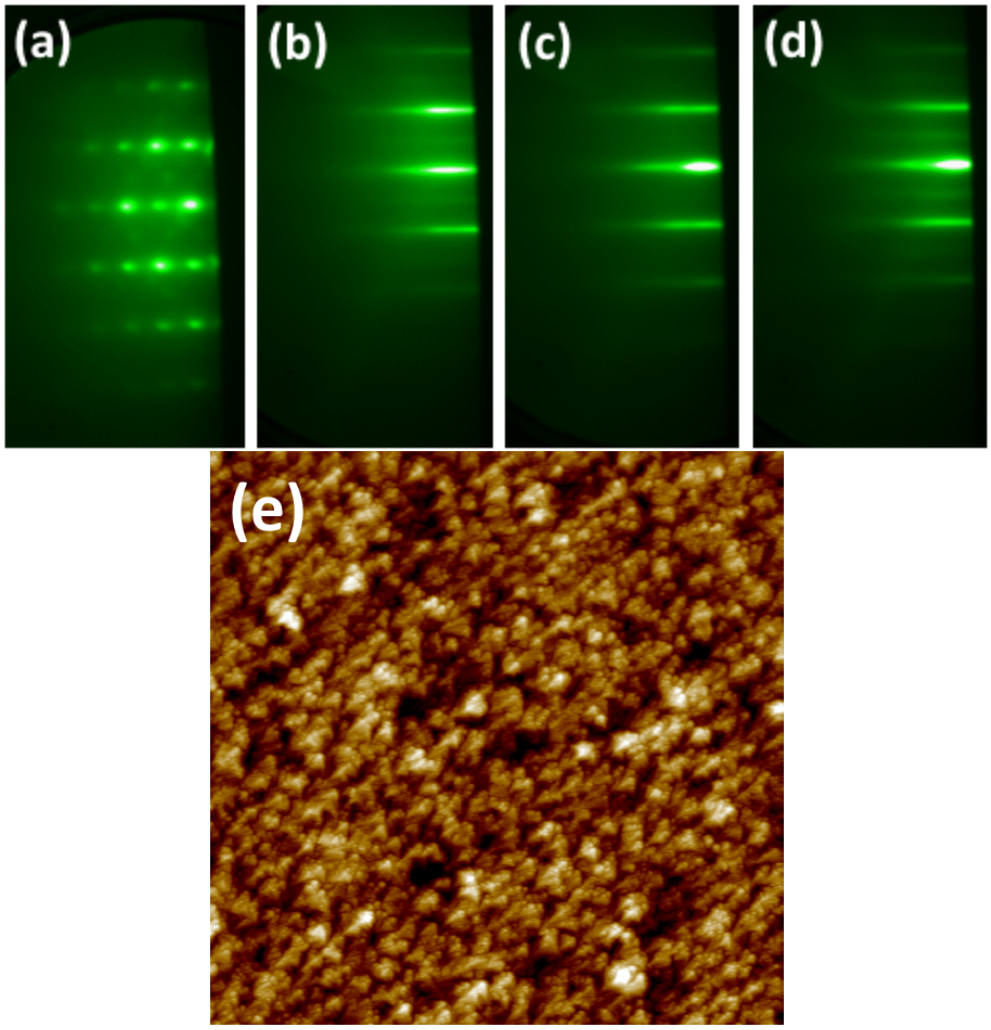

Figure 6.5: RHEED images for sample C – (a) after 20s of AlN, (b) at the end of 150 nm thick AlN buffer layer, (c) after 20s of GaN on the AlN buffer layer, (d) at the end of the thick GaN layer, and (e) 10x10 μm AFM image (height scale = 6 nm) with RMS roughness of 0.9 nm.

As shown in Figure 6.5(a), the AlN buffer nucleation directly on the alexandrite substrate resulted in an unusual RHEED pattern with mixed cubic/hexagonal phases and possibly polycrystalline domains. However, as the AlN growth progressed, the spotty and mixed phase pattern developed into clear streaks. At the end of AlN growth in

Figure 6.5(b) a sharp and streaky pattern with 2x2 reconstruction was clearly visible. The GaN film grown on this AlN buffer had no mixed phase or spotty patterns whatsoever as visible in Figure 4(c) taken after just 20 seconds of GaN growth. The GaN RHEED pattern was smooth and streaky from the onset of growth which developed into a 2x2 reconstruction after just 1 minute and continued to the end of growth in Figure 6.5(d). Finally, a 10x10 μm AFM image is shown in Figure 6.5(e) with an RMS roughness of 0.9 nm.

Finally, sample D was grown using a 60 minute low-temperature nitridation followed by a 2-step AlN buffer layer and a GaN anneal/regrowth procedure. The first part of the 2-step AlN layer was a ~5 nm thick nucleation layer grown at 700°C under nitrogen-rich conditions with a III/V ratio of 0.7. The second step was a 150 nm thick AlN layer grown under metal-rich conditions by MME at 750°C. The slightly N-rich nucleation layer has been shown to improve polarity control, surface morphology, and crystal quality as compared to Al-rich or highly N-rich nucleation layers due to higher density, more uniform nuclei.[195, 196] Then, the GaN anneal/regrowth procedure was performed by first growing a ~30 nm thick GaN layer at 600°C by MME, then halting the growth and annealing the film at 800°C for 5 minutes while exposed to the nitrogen plasma. The substrate temperature was then reduced to 600°C and growth by MME was resumed. This procedure has been shown to substantially improve the asymmetric rocking curve FWHM via Ostwald ripening and recrystallization.[87] Shown in Figure 6.6 are the RHEED images for this process.

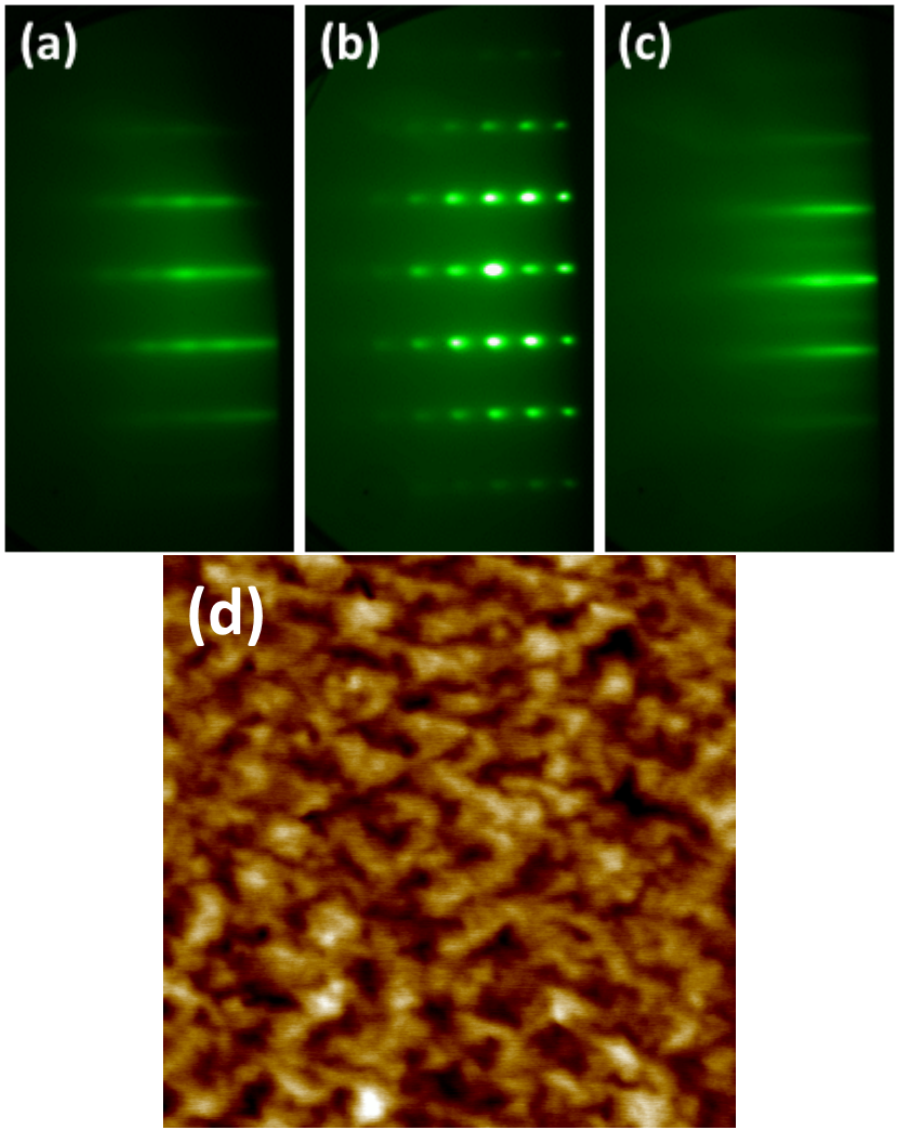

Figure 6.6: RHEED images for sample D - (a) at the end of the 2-step AlN buffer layer, (b) after 800°C GaN anneal, (c) at the end of the thick GaN layer. (d) AFM surface morphology for sample D with RMS roughness of 0.8 nm (height scale = 6 nm).

Figure 6.6(a) shows the AlN at the end of the 2-step buffer layer growth with slightly more diffuse streaks and clear spotting with no visible 2x2 reconstruction as compared to sample C (Figure 6.5) which had very sharp streaks and a clear 2x2 reconstruction with no spottiness in the RHEED pattern. This rougher pattern could be due to a modified surface structure from the nitridation, but is more likely due to the

reduced growth temperature of the main AlN layer which was grown at 750°C instead of 850°C. The lower substrate temperature would reduce surface adatom mobility, limiting lateral diffusion of the Al adatoms and inhibiting proper step-flow growth. At the end of the 800°C GaN anneal in Figure 6.6(b) a spotty pattern is visible indicating substantial roughening due to the decomposition of the thin GaN film. At the end of the GaN growth in Figure 6.6(c), the RHEED pattern has returned to a primarily streaky pattern indicating a smoother surface confirmed by the 2x2 reconstruction.

While the final RHEED patterns for the thick GaN films were all qualitatively similar, some important differences could be seen in the early stages of growth and in the buffer layers. In samples A and B where the GaN was nucleated directly on the alexandrite substrate, a mixed phase cubic/hexagonal pattern was clearly visible which indicates that the nitridation for sample B had minimal effect on the GaN nucleation. In addition, sample B with low temperature nitridation actually resulted in a spottier RHEED pattern and a rougher surface. This slight roughening was visible in the AlN buffer for sample D as well, which can be attributed primarily to the thin N-rich AlN nucleation layer and possibly to the nitridation step. For sample D, a thicker AlN layer would have given more time for complete coalescence and smoothing. For example, Fälth *et al* saw morphological improvement for buffer layers more than 250 nm thick.[196] In addition, the reduced substrate temperature for AlN in sample D, which was done to mitigate aluminum clustering at high temperature, could also contribute to the slightly rougher AlN as compared to sample C. With the direct nucleation of AlN on alexandrite with no nitridation, sample C showed the sharpest streaks and the brightest 2x2 reconstruction. Together, these results indicate that the nitridation might be

detrimental to surface morphology which is counter to what is seen for nitridation of sapphire.

6.6 XRD Characterization of III-Nitride Films on Alexandrite

X-ray diffraction was performed to characterize the phase, orientation, and crystal quality of the AlN and GaN films grown on alexandrite, as well as the alexandrite substrate itself. For the alexandrite substrates, rocking curves (ω-scan, not shown) about the symmetric (004) and asymmetric (222) peaks demonstrate FWHM of approximately 38 and 17 arcsec, respectively. These extremely narrow rocking curve FWHM values are in line with those of other Czochralski-grown bulk materials with dislocation densities on the order of 10^3 cm^{-2}.

As shown in Figure 6.7(a), the diffraction scan for sample A demonstrates single orientation c-axis GaN, with only the (002) and (004) GaN peaks visible indicating the single-orientation nature of the GaN film, along with the (002) and (004) alexandrite peaks. A weak peak at 20.05° is for the forbidden (001) alexandrite peak. A phi scan, shown in Figure 6.7(b), about the (102) GaN reflection shows 6 distinct peaks confirming the hexagonal single-crystal nature of the film rather than simply a textured polycrystalline film.

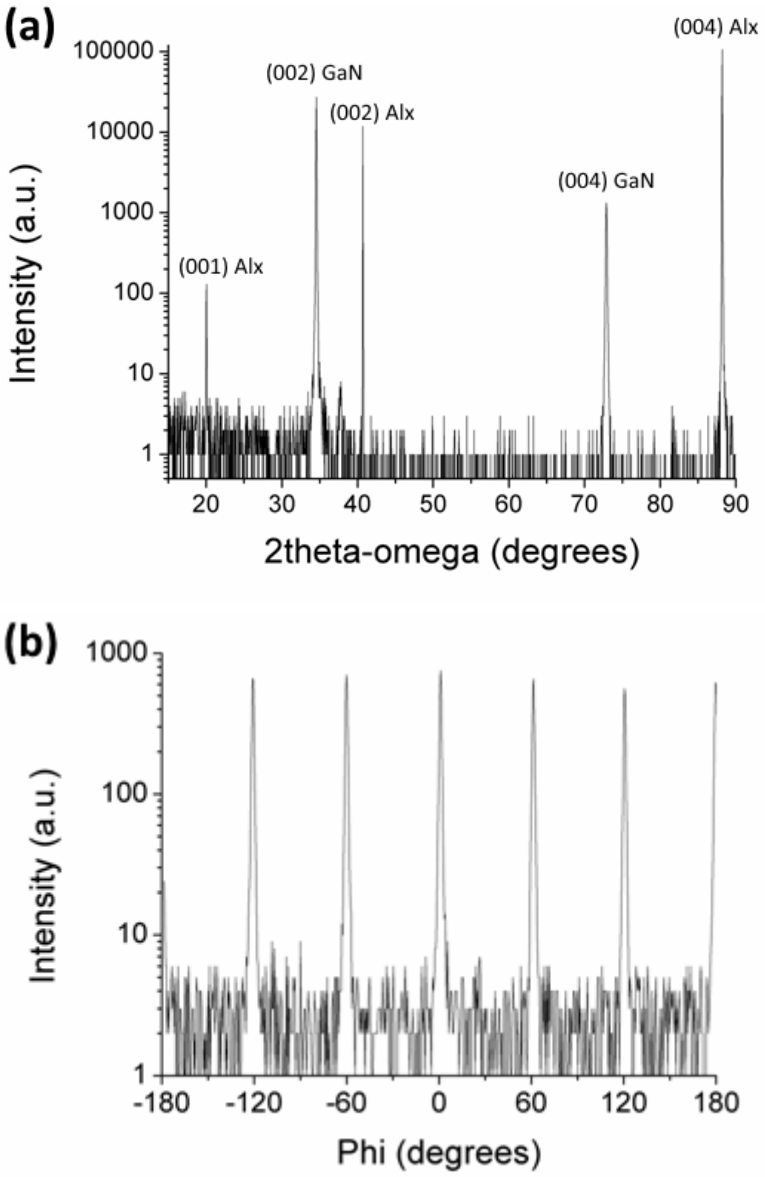

Figure 6.7: (a) Long-range 2θ-ω diffraction scan for sample A with GaN nucleated directly on the alexandrite substrate. (b) Phi scan about the (102) GaN peak with 6-fold symmetry.

A pole figure (not shown) was also performed to check for possible cubic inclusions, and no such inclusions were found. The ω rocking curve about the (002) GaN peak shows a broad FWHM of 2544 arcsec, while the (102) rocking curve FWHM is 3353 arcsec. These broad rocking curve widths can be attributed to the nucleation of

GaN directly on a non-polar, highly lattice mismatched substrate with no buffer layer or nitridation treatment as are typically performed with sapphire. A reciprocal space map (not shown) was also performed about the (105) GaN peak from which the *a* and *c* lattice constants were determined to be 3.188 Å and 5.186 Å, respectively, which represents approximately 0.03% residual in-plane compressive stress compared to 3.189 Å and 5.185 Å commonly reported for bulk GaN. Rocking curve measurements for all four GaN films with different nucleation and/or buffer layers are shown in Table 6.3 below.

Table 6.3: XRD rocking curve (ω scan) FWHM for symmetric and asymmetric reflections of GaN films grown on alexandrite substrates.

	(002) RC FWHM	**(105) RC FWHM**	**(102) RC FWHM**
Sample A (GaN only)	2553 arcsec	1040 arcsec	3550 arcsec
Sample B (nitridation + GaN)	1875 arcsec	734 arcsec	3117 arcsec
Sample C (AlN + GaN)	1601 arcsec	800 arcsec	2743 arcsec
Sample D (nitridation + 2-step AlN+ GaN)	2368 arcsec	926 arcsec	3769 arcsec

From Table 6.3 it is clear that the best overall GaN crystal quality came from sample C, which was grown without a nitridation process, but rather using direct nucleation of a thin AlN buffer layer before the growth of GaN. This further confirms the observation from the RHEED patterns which suggested that the best overall surface quality similarly came from sample C, with a very bright and sharp pattern. This result is markedly different from MBE growth on sapphire where a nitridation process is employed almost universally to improve nucleation and resulting film quality. The

RHEED pattern during nitridation remained primarily unchanged, suggesting that the surface chemistry was not heavily influenced by the nitridation process. This is, again, different than what is reported for MBE growth on sapphire where the nitridation causes a conversion of the surface to a very thin AlN layer which is clearly observed in the RHEED.

6.7 III-Nitride on Alexandrite Device

In spite of the poor crystal quality as determined by XRD, an attempt was made to fabricate a III-nitride LED using the alexandrite substrate. The LED was grown using the nucleation procedure from sample C with no nitridation and a single-step AlN buffer layer grown at 800°C to a thickness of 170 nm. A 1.6 μm thick Si-doped GaN layer was then grown by MME at 600°C with a target electron concentration of ~$5x10^{18}$ cm^{-3}. The 3-period MQW active region was grown at 500°C, consisting of 10 nm Si-doped GaN barriers grown by MME and 2 nm undoped $In_{0.12}Ga_{0.88}N$ quantum wells. After the final barrier, the substrate temperature was increased to 610°C for the growth of a 20 nm thick p-$Al_{0.10}Ga_{0.90}N$ electron blocking layer followed by the p-type contact layer at 600°C, both under conditions to resulting in high hole concentrations >10^{19} cm^{-3}. The device was then fabricated using traditional optical lithography and ICP etching to define the mesa structure. The metal contacts, deposited by electron beam evaporation, were Ni/Au for the p-type contact and Ti/Al/Ti/Au for the n-type contact. As with other devices grown using MME with high p-type doping, no contact or p-type activation anneals whatsoever were performed for this device.[54]

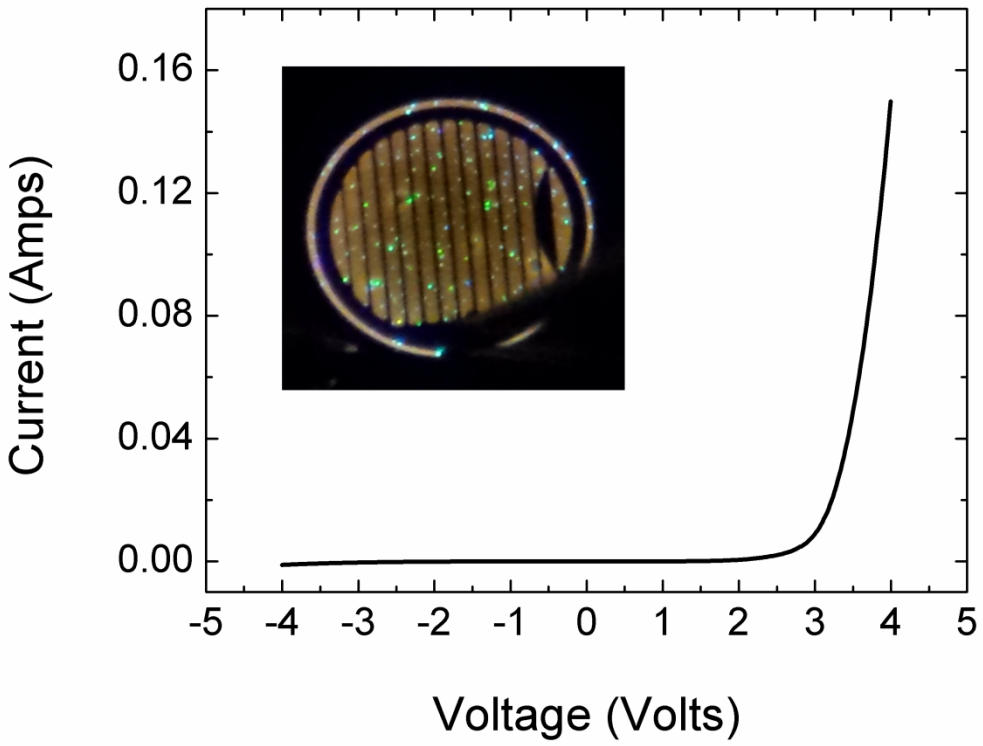

Figure 6.8: I-V curve for III-nitride on alexandrite LED with picture of LED under operation (inset).

Shown in Figure 6.8 is the resulting I-V curve from the LED structure with a clear rectifying behavior and proper turn-on at ~3 V. In spite of the highly defective nature of these films grown on alexandrite, the device nonetheless shows respectable diode behavior with a relatively low reverse bias leakage current, particularly considering the metal-rich nature of the growth technique used herein. Unfortunately, the LED did not exhibit uniform luminescence in the expected violet-blue wavelength range as seen in Figure 6.8 (inset). The likely cause of this is the highly defective material used for the device, which results in a high density of non-radiative recombination centers including threading dislocations and possibly stacking faults. While such defects showed minimal

detrimental effect on the electrical performance of the LED device, the optical properties were clearly affected negatively. The green/blue luminescence "specks" could be from macro defects where higher indium compositions clustered, resulting in additional localized carrier confinement and improved luminescence. Thus, while the electrical characteristics of the LED were promising, the optical performance leaves much to be desired and improvements must be made to the material quality in order to realistically address the present issues.

6.8 Conclusion

In conclusion, for the first time, the growth of GaN films on alexandrite ($BeAl_2O_4$) substrates was explored using plasma-assisted molecular beam epitaxy. Several nucleation methods were attempted including direct nucleation of GaN, and low-temperature nitridation with and without AlN buffer layers. The RHEED patterns during the nucleation showed significantly different behavior for the varied nucleation conditions, while the final RHEED patterns were smooth and streaky owing to the metal-rich growth technique. The surface roughness for all films was consistently between 0.5 and 1 nm RMS as determined by AFM surface morphology characterization, but did not exhibit the ideal dislocation-mediated step-flow growth character. X-ray diffraction showed that the GaN and AlN films were highly defective, regardless of the nucleation condition chosen, with (002) rocking curve FWHM >1500 arcsec in all cases. A simple LED was fabricated, in spite of the poor crystal quality, which demonstrated a clear rectifying behavior and proper turn-on at ~3 V. However, the luminescence of the LED was extremely non-uniform with only blue/green luminescence from small specks rather

than a violet/blue luminescence as was expected from the quantum well design. For a sensitive light-emitting device, a significant reduction in defect densities is likely required for the device to function more ideally. Nonetheless, the respectable rectifying behavior of this highly preliminary device offers some promise for the future of GaN using these non-traditional substrates. If the material quality issues can be addressed, then the application to an extremely compact, epitaxially integrated diode-pumped alexandrite laser system might be achievable.

CHAPTER 7: SUMMARY AND FUTURE DIRECTIONS

In summary, several of the major impediments facing III-nitride materials and devices were examined: p-type doping, defect densities, and substrates. A novel growth technique called metal-modulated epitaxy was employed to achieve record high hole concentrations in III-nitride thin films. In-depth studies of the electrical transport properties, optical properties, and structural properties in highly p-type GaN, InGaN, and AlGaN were performed. A modified plasma source was explored to improve MBE growth rates of III-nitride films. A mixed chemistry plasma was employed to mitigate detrimental plasma effects, and record high growth rates were demonstrated. GaN growth on Si was performed using direct and buffered nucleation techniques for a vertically conducting heterojunction device. Finally, GaN was grown on an alternative substrate called alexandrite to explore the possibility for unique misfit dislocation generation mechanisms in highly lattice mismatched heteroepitaxy.

7.1 P-Type Doping

A temperature-dependent Hall effect study of high p-type doping effects in GaN was performed. Highly p-type GaN films grown using the MME technique with hole concentrations exceeding 10^{19} cm^{-3} were found to exhibit dramatically different electrical characteristics compared to films with more traditional doping levels of ~10^{18} cm^{-3}. As expected from a deep, isolated acceptor, the more lightly doped material exhibited significant carrier freeze-out at cryogenic temperatures resulting in high resistivity and an

inversion to n-type conductivity from donor compensation. On the other hand, the highly p-type MME-grown films exhibited minimal carrier freeze-out while remaining p-type throughout the entire measured temperature range. Acceptor activation energies were found to drop to just 43 meV as doping levels increased. SIMS analysis was performed on a highly p-type film grown by MME which demonstrated a Mg activation efficiency of 52% compared with 1-5% for conventional p-type GaN. Together, the high hole concentrations, lack of carrier freeze-out, high activation efficiency, and reduced activation energies of these highly p-type films point to the onset of the Mott insulator transition as the explanation for these unique results, with a highest achieved room temperature hole concentration in GaN of 7.9×10^{19} cm^{-3}.

Further exploration in the growth of these highly doped films was performed, and it was found that the III/V ratio plays a critical role in the proper incorporation of electrically active Mg. At a III/V ratio above 1.5, the Mg concentrations decreased compared to growths at lower III/V ratio, suggesting that the excessively metal-rich surface may have enhanced Mg desorption, allowed Mg clustering, or simply allowed Mg to incorporate on nitrogen sites. The electrical characterization pointed to several conduction mechanisms, where the higher III/V ratio films were dominated by 2D transport in a 2DHG at the AlN/p-GaN interface. Lower III/V ratio resulted in significantly higher hole concentrations and bulk-dominated conductivity where the 2DHG contributed less than 10% of the overall measured hole concentrations. Structural characterization by TEM showed that films grown using optimal conditions resulted in no Mg precipitation, stacking faults, or inversion domains, even for Mg concentrations of 2.5×10^{20} cm^{-3}, while traditional high temperature growth techniques show Mg

precipitation for Mg concentrations of just $5x10^{19}$ cm^{-3}.

Optical characterization of MME-grown p-GaN and p-AlGaN was performed to better understand some of the unique electrical properties. All films exhibited room temperature hole concentrations exceeding $2x10^{19}$ cm^{-3}, even for p-AlGaN with Al fractions of 11% and 27%. The photoluminescence spectrum for the p-type GaN exhibited a single, broad emission peak centered at ~378 nm with a high energy tail intercepting the valence band and no visible phonon replicas. A similar effect was seen in p-AlGaN with 11% Al fraction and a peak emission wavelength of ~358 nm. These broad luminescence peaks intercepting the valence band, along with the absence of phonon replicas and high hole concentrations, provide further evidence for the presence of an acceptor band. As the isolated acceptor energy splits into a band, more possible transition energies emerge, thus resulting in broad PL emission as was shown here.

To further confirm the p-type nature of these highly Mg-doped MME-grown films, several simple diode devices were fabricated using traditional optical lithography, dry etching, and metal evaporation techniques. The resulting device showed clear rectifying behavior with a turn-on of ~3 V and a respectable series resistance of 6 Ω, even with no p-type activation anneal or contact anneals, simplifying the fabrication process and further confirming the highly p-type nature of these MME-grown p-GaN films such that the contacts were ohmic as-deposited. A simple three-period multi-quantum well LED was also fabricated, and the diode showed proper rectifying behavior with ~3 V turn-on and 10 Ω series resistance. The device showed violet-blue emission which continued even while submerged in liquid nitrogen. The rectifying behavior of the diodes without the need for p-type activation or contact anneals provides unambiguous proof

that these highly Mg-doped MME-grown GaN films are truly p-type.

7.2 High Growth Rate GaN

To address the slow growth rates of MBE, a modified high-conductance nitrogen plasma source was explored with the goal of achieving rapid growth of thick layers to reduce defect densities. Using pure nitrogen, growth rates from 1.6 μm/hour up to 8.4 μm/hour were achieved. Even for growth at 6 μm/hour, step-flow growth with sub-nanometer RMS roughness was demonstrated. A mixed argon-nitrogen plasma chemistry was also explored which resulted in significant reductions in ion content and showed increased growth rates up to 9.8 μm/hour, more than an order of magnitude higher than typical MBE growth rates. Trends in atomic and molecular nitrogen content were studied and the mixed chemistry plasma showed a dramatic increase in the atomic nitrogen signals at high flow rates with a peak between 50% and 75% argon. These trends suggest that a mixed chemistry plasma could simultaneously reduce damaging ion content and improve growth rates through more efficient generation of reactive atomic nitrogen species. Germanium doping was explored at high growth rates for n-type doping due to the low vapor pressure of silicon, and the electron concentration was controllable from $2x10^{16}$ up to $4x10^{19}$ cm^{-3}. Uninentionally-doped GaN films grown at ~2 μm/hour demonstrated repeatable background electron concentrations of just $1\text{-}2x10^{15}$ cm^{-3}, showing great promise for power electronics.

7.3 GaN Growth on Si

GaN growth on Si was explored with the goal of making a III-nitride/Si

heterojunction solar cell. Nucleation from a pre-exposure of gallium droplets results in relatively rough surfaces and polycrystalline GaN films. X-ray diffraction analysis for these films showed very poor crystal quality suggesting the need for further optimization. Devices using this nucleation method resulted in either conducting or rectifying vertical devices. A simple GaN/Si heterojunction solar cell exhibited J_{SC} of ~58 mA/cm^2 and V_{OC} of ~0.3 V at a concentration of ~5 suns, showing promise for future work. For the case of p-GaN on p-Si, the reverse bias breakdown of the vertical device was ~170 V. The demonstration of epitaxial aluminum with smooth surfaces led to an alternative nucleation technique attempting to exploit the Al-Si eutectic formation. The AlN/SiN_X formed from this technique resulted in an improvement in the crystal quality of the subsequent GaN layers, smoother surfaces, and no polycrystalline features in the RHEED and XRD analysis. However, some misaligned crystallite formations were visible in SEM images with significant surface pits still present. Moreover, ~1 μm thick films demonstrated cracking from tensile stress during cool-down in spite of the lower temperature MBE techniques used herein.

7.4 Growth of GaN on Alexandrite ($BeAl_2O_4$)

Seeing the success of growing highly lattice mismatched InGaN on GaN, this work was performed to see if similar relaxation mechanisms could be achieved in the heteroepitaxy of GaN on lattice mismatched substrates. Alexandrite ($BeAl_2O_4$), with an orthorhombic crystal structure, was used as the substrate for this study. Several nucleation and buffer layers were attempted, and it was found that both direct nucleation of GaN as well as the use of AlN buffer layers resulted in poor crystal quality.

Nonetheless, smooth surfaces with sub-nanometer RMS roughnesses were demonstrated in all cases. The best GaN crystal quality was achieved with a ~150 nm thick AlN buffer, and this structure was then used as the basis for a multi-quantum well LED. The LED did not show the expected violet-blue luminescence, but rather highly non-uniform green/blue spots. In spite of the poor crystal quality, the device demonstrated proper rectifying behavior with turn-on voltage of ~3 V, showing promise for future work.

7.5 Future Work

1. **Optimization of p-type contacts**. Although no contact anneal was required for proper device behavior in this work, little effort was made to explore nature of the p-type contacts on this unique, highly p-type material. Further study using different contacts and spreading layers (i.e. Pt, Pd, ITO, etc.) should yield improvements in contact resistance and overall device performance.
2. **Elimination of macroscopic surface features at high growth rates**. Given the dramatic improvements in growth rate made herein, the most pressing improvement required in future work is to eliminate the macroscopic surface features which became problematic at elevated growth rates. If this gallium spitting can be mitigated, then it could be possible to achieve extremely low background electron concentrations $<10^{15}$ cm^{-3} in GaN. This would open the door for MBE growth of power electronic devices like high voltage p-i-n

rectifiers with thick, rapidly-grown drift regions for ultra-high breakdown voltages. A re-designed effusion cell could help eliminate gallium spitting and also increase usable volume for longer growth campaigns.

3. **Push growth rates higher**. While the 9.8 μm/hour growth rate achieved herein represents more than a 10x improvement compared to traditional MBE, it is not necessarily an upper bound. The mass flow controller configuration in this work limited the nitrogen and argon flows and, thus, the growth rate. Using more nitrogen and/or argon flow and optimizing the gas ratios in the plasma should lead to even higher growth rates than those achieved in this work.
4. **Improve GaN-on-Si crystal quality**. While the use of AlN/SiN_X resulted in improved crystal quality compared to direct growth of GaN on Si, the GaN films still left much to be desired. Further optimization of the coalescence and better control of the nucleation to eliminate the crystallite formations should improve surface quality while reducing crystalline defects. Higher temperature growth might be required to prevent the growth of GaN in the SiN_X field in order to enhance the lateral overgrowth effects from the AlN seeds. Such improvements in crystal quality and surface roughness/uniformity would be necessary for the eventual realization of a III-nitride/Si tandem solar cell for high efficiency, lower cost applications.

REFERENCES

[1] Y. Nanishi, Y. Saito and T. Yamaguchi, "RF-Molecular Beam Epitaxy Growth and Properties of InN and Related Alloys," Jpn. J. Appl. Phys., **42**, 2549 (2003).

[2] N. S. Mansour, K. W. Kim and M. A. Littlejohn, "Theoretical study of electron transport in gallium nitride," J. Appl. Phys., **77**, 2834 (1995).

[3] J. Kolník, I. H. Oğuzman, K. F. Brennan, R. Wang, P. P. Ruden and Y. Wang, "Electronic transport studies of bulk zincblende and wurtzite phases of GaN based on an ensemble Monte Carlo calculation including a full zone band structure," J. Appl. Phys., **78**, 1033 (1995).

[4] S. Nakamura, "Present Status of InGaN-Based Laser Diodes," Phys. Status Solidi A, **176**, 15 (1999).

[5] O. Jani, I. Ferguson, C. Honsberg and S. Kurtz, "Design and characterization of GaN/InGaN solar cells," Appl. Phys. Lett., **91**, 132117 (2007).

[6] P. Schlotter, R. Schmidt and J. Schneider, "Luminescence conversion of blue light emitting diodes," Appl. Phys. A, **64**, 417 (1997).

[7] S. Nakamura, T. Mukai and M. Senoh, "Candela-class high-brightness InGaN/AlGaN double-heterostructure blue-light-emitting diodes," Appl. Phys. Lett., **64**, 1687 (1994).

[8] C.-Y. Yeh, Z. W. Lu, S. Froyen and A. Zunger, "Zinc-blende - wurtzite polytypism in semiconductors," Phys. Rev. B, **46**, (1992).

[9] J. Kim, Ph.D. thesis, Georgia Institute of Technology, 2014.

[10] M. A. Moram and M. E. Vickers, "X-ray diffraction of III-nitrides," Rep. Prog. Phys., **72**, 036502 (2009).

[11] Z. M. Lochner, Ph.D. thesis, Georgia Institute of Technology, 2013.

[12] O. Ambacher, R. Dimitrov, M. Stutzmann, B. E. Foutz, M. J. Murphy, J. A. Smart, J. R. Shealy, N. G. Weimann, K. Chu, M. Chumbes, B. Green, A. J. Sierakowski, W. J. Schaff and L. F. Eastman, "Role of Spontaneous and Piezoelectric Polarization Induced Effects in Group-III Nitride Based Heterostructures and Devices," Phys. Status Solidi B, **216**, 381 (1999).

[13] C. A. M. Fabien, M. Moseley, B. Gunning, W. A. Doolittle, A. M. Fischer, Y. O. Wei and F. A. Ponce, "Simulations, Practical Limitations, and Novel Growth Technology for InGaN-Based Solar Cells," IEEE J. Photovolt., **4**, 601 (2014).

[14] S. Chichibu, T. Azuhata, T. Sota and S. Nakamura, "Spontaneous emission of localized excitons in InGaN single and multiquantum well structures," Appl.

Phys. Lett., **69**, 4188 (1996).

[15] L.-H. Peng, C.-W. Chuang and L.-H. Lou, "Piezoelectric effects in the optical properties of strained InGaN quantum wells," Appl. Phys. Lett., **74**, 795 (1999).

[16] M. Moseley, Ph.D. thesis, Georgia Institute of Technology, 2013.

[17] A. Castiglia, J.-F. Carlin and N. Grandjean, "Role of stable and metastable Mg-H complexes in p-type GaN for cw blue laser diodes," Appl. Phys. Lett., **98**, 213505 (2011).

[18] J. Neugebauer and C. G. V. d. Walle, "Theory of point defects and complexes in GaN," Mater. Res. Soc. Symp. P, **395**, 645 (1995).

[19] F. A. Reboredo and S. T. Pantelides, "Novel defect complexes and their role in the p-type doping of GaN," Phys. Rev. Lett., **82**, 1887 (1999).

[20] L. Liu and J. H. Edgar, "Substrates for gallium nitride epitaxy," Mater. Sci. Eng., R **37**, 61 (2002).

[21] S. A. Nikishin, N. N. Faleev, V. G. Antipov, S. Francoeur, L. G. d. Peralta, G. A. Seryogin, H. Temkin, T. I. Prokofyeva, M. Holtz and S. N. G. Chu, "High quality GaN grown on Si(111) by gas source molecular beam epitaxy with ammonia," Appl. Phys. Lett., **75**, 2073 (1999).

[22] S. Zamir, B. Meyler, E. Zolotoyabko and J. Salzman, "The effect of AlN buffer layer on GaN grown on (111)-oriented Si substrates by MOCVD," J. Cryst. Growth, **218**, 181 (2000).

[23] X. H. Wu, L. M. Brown, D. Kapolnek, S. Keller, B. Keller, S. P. DenBaars and J. S. Speck, "Defect structure of metal-organic chemical vapor deposition-grown epitaxial (0001) GaN/Al2O3," J. Appl. Phys., **80**, 3228 (1996).

[24] S. Kosaraju, J. A. Marino, J. A. Harvey and C. A. Wolden, "The role of argon in plasma-assisted deposition of indium nitride," J. Cryst. Growth, **286**, 400 (2006).

[25] S. W. Kaun, M. H. Wong, S. Dasgupta, S. Choi, R. Chung, U. K. Mishra and J. S. Speck, "Effects of Threading Dislocation Density on the Gate Leakage of AlGaN/GaN Heterostructures for High Electron Mobility Transistors," Appl. Phys. Express, **4**, 024101 (2011).

[26] A. J. Ptak, M. R. Millecchia, T. H. Myers, K. S. Ziemer and C. D. Stinespring, "The relation of active nitrogen species to high-temperature limitations for (000$\bar{1}$) GaN growth by radio-frequency-plasma-assisted molecular beam epitaxy," Appl. Phys. Lett., **74**, 3836 - 3838 (1999).

[27] R. Dwilinski, R. Doradzinski, J. Garczynski, L. P. Sierzputowski, A. Puchalski, Y. Kanbara, K. Yagi, H. Minakuchi and H. Hayashi, "Bulk ammonothermal

GaN," J. Cryst. Growth, **311**, 3015 (2009).

[28] R. Dwilinski, R. Doradzinski, J. Garczynski, L. P. Sierzputowski, A. Puchalski, Y. Kanbara, K. Yagi, H. Minakuchi and H. Hayashi, "Excellent crystallinity of truly bulk ammonothermal GaN," J. Cryst. Growth, **310**, 3911 (2008).

[29] A. Yoshikawa, E. Ohshima, T. Fukuda, H. Tsuji and K. Oshima, "Crystal growth of GaN by ammonothermal method," J. Cryst. Growth, **260**, 67 (2004).

[30] T. Hashimoto, F. Wu, J. S. Speck and S. Nakamura, "A GaN bulk crystal with improved structural quality grown by the ammonothermal method," Nat. Mater., **6**, 568 (2007).

[31] J. H. Edgar, L. Liu, B. Liu, D. Zhuang, J. Chaudhuri, M. Kuball and S. Rajasingam, "Bulk AlN crystal growth: self-seeding and seeding on 6H-SiC substrates," J. Cryst. Growth, **246**, 187 (2002).

[32] R. Schlesser, R. Dalmau and Z. Sitar, "Seeded growth of AlN bulk single crystals by sublimation," J. Cryst. Growth, **241**, 416 (2002).

[33] H. Lahreche, P. Vennegues, O. Tottereau, M. Laugt, P. Lorenzini, M. Leroux, B. Beaumont and P. Gibart, "Optimisation of AlN and GaN growth by metalorganic vapour-phase epitaxy (MOVPE) on Si(1 1 1)," J. Cryst. Growth, **217**, 13 (2000).

[34] P. Chen, R. Zhang, Z. M. Zhao, D. J. Xi, B. Shen, Z. Z. Chen, Y. G. Zhou, S. Y. Xie, W. F. Lu and Y. D. Zheng, "Growth of high quality GaN layers with AlN buffer on Si(1 1 1) substrates," J. Cryst. Growth, **225**, 150 (2001).

[35] Y. Nakada, I. Aksenov and H. Okumura, "GaN heteroepitaxial growth on silicon nitride buffer layers formed on Si (111) surfaces by plasma-assisted molecular beam epitaxy," Appl. Phys. Lett., **73**, 827 (1998).

[36] A. Dadgar, M. Poschenrieder, J. Blasing, K. Fehse, A. Diez and A. Krost, "Thick, crack-free blue light-emitting diodes on Si(111) using low-temperature AlN interlayers and in situ Si_xN_y masking," Appl. Phys. Lett., **80**, 3670 (2002).

[37] A. Dadgar, J. Blasing, A. Diez, A. Alam, M. Heuken and A. Krost, "Metalorganic Chemical Vapor Phase Epitaxy of Crack-Free GaN on Si (111) Exceeding 1μm in Thickness," Jpn. J. Appl. Phys., **39**, L1183 (2000).

[38] A. Dadgar, M. Poschenrieder, A. Reiher, J. Bläsing, J. Christen, A. Krtschil, T. Finger, T. Hempel, A. Diez and A. Krost, "Reduction of stress at the initial stages of GaN growth on Si(111)," Appl. Phys. Lett., **82**, 28 (2003).

[39] A. Reiher, J. Blasing, A. Dadgar, A. Diez and A. Krost, "Efficient stress relief in GaN heteroepitaxy on Si(1 1 1) using low-temperature AlN interlayers," J. Cryst. Growth, **248**, 150 (2003).

[40] D. G. Zhao, S. J. Xu, M. H. Xie, S. Y. Tong and H. Yang, "Stress and its effect on optical properties of GaN epilayers grown on S(111), 6H-SiC(0001), and c-plane sapphire," Appl. Phys. Lett., **83**, 677 (2003).

[41] S.-H. Jang and C.-R. Lee, "High-quality GaN/Si(1 1 1) epitaxial layers grown with various $Al_{0.3}Ga_{0.7}N$/GaN superlattices as intermediate layer by MOCVD," J. Cryst. Growth, **253**, 64 (2003).

[42] L. Zhe, W. Xiao-Liang, W. Jun-Xi, H. Guo-Xin, G. Lun-Chun and L. Jin-Min, "The influence of AlN/GaN superlattice intermediate layer on the properties of GaN grown on Si(111) substrates," Chin. Phys., **16**, 1467 (2007).

[43] A. Able, W. Wegscheider, K. Engl and J. Zweck, "Growth of crack-free GaN on Si(1 1 1) with graded AlGaN buffer layers," J. Cryst. Growth, **276**, 415 (2005).

[44] F. Semond, Y. Cordier, N. Grandjean, F. Natali, B. Damilano, S. Vezian and J. Massies, "Molecular Beam Epitaxy of Group-III Nitrides on Silicon Substrates: Growth, Properties and Device Applications," Phys. Status Solidi A, **188**, 501 (2001).

[45] M. Sobanska, K. Klosek, Z. R. Zytkiewicz, J. Borysiuk, B. S. Witkowski, E. Lusakowska, A. Reszka and R. Jakiela, "Plasma-assisted MBE growth of GaN on Si(111) substrates," Cryst. Res. Technol., **47**, 307 (2012).

[46] M. K. Sunkara, S. Sharma, R. Miranda, G. Lian and E. C. Dickey, "Bulk synthesis of silicon nanowires using a low-temperature vapor–liquid–solid method," Appl. Phys. Lett., **79**, 1546 (2001).

[47] H. Ishikawa, K. Yamamoto, T. Egawa, T. Soga, T. Jimbo and M. Umeno, "Thermal stability of GaN on (1 1 1) Si substrate," J. Cryst. Growth, **189/190**, 178 (1998).

[48] J. Wu, W. Walukiewicz, K. M. Yu, W. Shan, J. W. Ager, E. E. Haller, H. Lu, W. J. Schaff, W. K. Metzger and S. Kurtz, "Superior radiation resistance of $In_{1-x}Ga_xN$ alloys: Full-solar-spectrum photovoltaic material system," J. Appl. Phys., **94**, 6477 (2003).

[49] M. Mesrine, N. Grandjean and J. Massies, "Efficiency of NH_3 as nitrogen source for GaN molecular beam epitaxy," Appl. Phys. Lett., **72**, 350 (1998).

[50] G. W. Wicks, M. W. Koch and J. R. Pedrazzani, "Studies of ammonia dissociation during the gas source molecular-beam epitaxial growth of III nitrides," J. Vac. Sci. Technol. B, **23**, 1186 (2005).

[51] N. A. El-Masry, E. L. Piner, S. X. Liu and S. M. Bedair, "Phase separation in InGaN grown by metalorganic chemical vapor deposition," Appl. Phys. Lett., **72**, 40 (1998).

[52] G. B. Stringfellow, "Microstructures produced during the epitaxial growth of InGaN alloys," J. Cryst. Growth, **312**, 735 (2010).

[53] I. Ho and G. B. Stringfellow, "Solid phase immiscibility in GaInN," Appl. Phys. Lett., **69**, 2701 (1996).

[54] B. P. Gunning, C. A. M. Fabien, J. J. Merola, E. A. Clinton, W. A. Doolittle, S. Wang, A. M. Fischer and F. A. Ponce, "Comprehensive study of the electronic and optical behavior of highly degenerate p-type Mg-doped GaN and AlGaN," J. Appl. Phys., **117**, 045710 (2015).

[55] R. Singh, D. Doppalapudi and T. D. Moustakas, "Phase sepaation in InGaN thick films and formation of InGaN/GaN double heterostructures in the entire alloy composition," Appl. Phys. Lett., **70**, 1089 (1997).

[56] I.-H. Kim, H.-S. Park, Y.-J. Park and T. Kim, "Formation of V-shaped pits in InGaN/GaN multiquantum wells and bulk InGaN films," Appl. Phys. Lett., **73**, 1634 (1998).

[57] R. Dahal, B. Pantha, J. Li, J. Y. Lin and H. X. Jiang, "InGaN/GaN multiple quantum well solar cells with long operating wavelengths," Appl. Phys. Lett., **94**, 063505 (2009).

[58] R. M. Farrell, C. J. Neufeld, C. Cruz, J. R. Lang, M. Iza, S. Keller, S. Nakamura, S. P. DenBaars, U. K. Mishra and J. S. Speck, "High quantum efficiency InGaN/GaN multiple quantum well solar cells with spectral response extending out to 520 nm," Appl. Phys. Lett., **98**, 201107 (2011).

[59] C. J. Neufeld, N. G. Toledo, S. C. Cruz, M. Iza, S. P. DenBaars and U. K. Mishra, "High quantum efficiency InGaN/GaN solar cells with 2.95 eV band gap," Appl. Phys. Lett., **93**, 143502 (2008).

[60] E. Matioli, C. Neufeld, M. Iza, S. C. Cruz, A. A. Al-Heji, X. Chen, R. M. Farrell, S. Keller, S. DenBaars, U. Mishra, S. Nakamura, J. Speck and C. Weisbuch, "High internal and external quantum efficiency InGaN/GaN solar cells," Appl. Phys. Lett., **93**, 021102 (2011).

[61] Z. Q. Li, M. Lestradet, Y. G. Xiao and S. Li, "Effects of polarization charge on the photovoltaic properties of InGaN solar cells," Phys. Status Solidi A, **208**, 928 (2011).

[62] G. F. Brown, J. W. A. III, W. Walukiewicz and J. Wu, "Finite element simulations of compositionally graded InGaN solar cells," Sol. Energy Mater. Sol. Cells, **94**, 478 (2010).

[63] C. J. Neufeld, S. C. Cruz, R. M. Farrell, M. Iza, J. R. Lang, S. Keller, S. Nakamura, S. P. DenBaars, J. S. Speck and U. K. Mishra, "Effect of doping and polarization on carrier collection in InGaN quantum well solar cells," Appl. Phys.

Lett., **98**, 243507 (2011).

[64] W. Götz, N. M. Johnson, J. Walker, D. P. Bour and R. A. Street, "Activation of acceptors in Mg-doped GaN grown by metalorganic chemical vapor deposition," Appl. Phys. Lett., **68**, 667 (1996).

[65] S. Nakamura, T. Mukai, M. Senoh and N. Iwasa, "Thermal annealing effects on p-type Mg-doped GaN films," Jpn. J. Appl. Phys., **31**, L139 (1992).

[66] O. Svensk, S. Suihkonen, T. Lang, H. Lipsanen, M. Sopanen, M. A. Odnoblyudov and V. E. Bougrov, "Effect of growth conditions on electrical properties of Mg-doped p-GaN," J. Cryst. Growth, **298**, 811 (2007).

[67] P. Kozodoy, S. Keller, S. P. DenBaars and U. K. Mishra, "MOVPE growth and characterization of Mg-doped GaN," J. Cryst. Growth, **195**, 265 (1998).

[68] Z. Liliental-Weber, M. Benamara, W. Swider, J. Washburn, I. Grzegory, S. Porowski, D. J. H. Lambert, C. J. Eiting and R. D. Dupuis, "Mg-doped GaN: Similar defects in bulk crystals and layers grown on Al_2O_3 by metal–organic chemical-vapor deposition," Appl. Phys. Lett., **75**, 4159 (1999).

[69] A. Bell, R. Liu, F. A. Ponce, H. Amano, I. Akasaki and D. Cherns, "Light emission and microstructure of Mg-doped AlGaN grown on patterned sapphire," Appl. Phys. Lett., **82**, 349 (2003).

[70] S. Pezzagna, P. Vennéguès, N. Grandjean and J. Massies, "Polarity inversion of GaN(0001) by a high Mg doping," J. Cryst. Growth, **269**, 249 (2004).

[71] D. S. Green, E. Haus, F. Wu, L. Chen, U. K. Mishra and J. S. Speck, "Polarity control during molecular beam epitaxy growth of Mg-doped GaN," J. Vac. Sci. Technol. B, **21**, 1804 (2003).

[72] A. Bhattacharyya, W. Li, J. Cabalu, T. D. Moustakas, D. J. Smith and R. L. Hervig, "Efficient p-type doping of GaN films by plasma-assisted molecular beam epitaxy," Appl. Phys. Lett., **85**, 4956 (2004).

[73] M. Zhang, P. Bhattacharya, W. Guo and A. Banerjee, "Mg doping of GaN grown by plasma-assisted molecular beam epitaxy under nitrogen-rich conditions," Appl. Phys. Lett., **96**, 132103 (2010).

[74] J. Neugebauer and C. G. V. d. Walle, "Role of hydrogen in doping of GaN," Appl. Phys. Lett., **63**, 1829 (1996).

[75] G. Koblmüller, F. Reurings, F. Tuomisto and J. S. Speck, "Influence of Ga/N ratio on morphology, vacancies, and electrical transport in GaN grown by molecular beam epitaxy at high temperature," Appl. Phys. Lett., **97**, 191915 (2010).

[76] U. Kaufmann, P. Schlotter, H. Obloh, K. Kohler and M. Maier, "Hole

conductivity and compensation in epitaxial GaN:Mg layers," Phys. Rev. B, **62**, 10867 (2000).

[77] J. Xie, X. Ni, Q. Fan, R. Shimada, Ü. Özgür and H. Morkoç, "On the efficiency droop in InGaN multiple quantum well blue light emitting diodes and its reduction with p-doped quantum well barriers," Appl. Phys. Lett., **93**, 121107-1 - 121107-3 (2008).

[78] X. Li, X. Ni, J. Lee, M. Wu, Ü. Özgür, H. Morkoç, T. Paskova, G. Mulholland and K. R. Evans, "Efficiency retention at high current injection levels in m-plane InGaN light emitting diodes," Appl. Phys. Lett., **95**, 121107 (2009).

[79] T. Chung, J. Limb, J.-H. Ryou, W. Lee, P. Li, D. Yoo, X.-B. Zhang, S.-C. Shen, R. D. Dupuis, D. Keogh, P. Asbeck, B. Chukung, M. Feng, D. Zakharov and Z. Lilienthal-Weber, "Growth of InGaN HBTs by MOCVD," J. Electron. Mater., **35**, 695 (2006).

[80] S. D. Burnham and W. A. Doolittle, "*In situ* growth regime characterization of AlN using reflection high energy electron diffraction," J. Vac. Sci. Technol. B, **24**, 2100 (2006).

[81] S. D. Burnham, W. Henderson and W. A. Doolittle, "Closed-loop MBE growth of droplet-free GaN with very metal rich conditions using Metal Modulated Epitaxy with Mg and In," Phys. Status Solidi C, **5**, 1855 (2008).

[82] M. Moseley, D. Billingsley, W. Henderson, E. Trybus and W. A. Doolittle, "Transient atomic behavior and surface kinetics of GaN," J. Appl. Phys., **106**, 014905 (2009).

[83] G. Namkoong, E. Trybus, K. K. Lee, M. Moseley, W. A. Doolittle and D. C. Look, "Metal modulation epitaxy growth for extremely high hole concentrations above 10^{19} cm^{-3} in GaN," Appl. Phys. Lett., **93**, 172112 (2008).

[84] E. Trybus, W. A. Doolittle, M. Moseley, W. Henderson, D. Billingsley, G. Namkoong and D. C. Look, "Extremely high hole concentrations in c-plane GaN," Phys. Status Solidi C, **6**, S788 (2009).

[85] G. Namkoong, W. A. Doolittle, A. S. Brown, M. Losurdo, P. Capezzuto and G. Bruno, "Role of sapphire nitridation temperature on GaN growth by plasma assisted molecular beam epitaxy: Part I. Impact of the nitridation chemistry on material characteristics," J. Appl. Phys., **91**, 2499 (2002).

[86] M. Losurdo, P. Capezzuto, G. Bruno, G. Namkoong, W. A. Doolittle and A. S. Brown, "Role of sapphire nitridation temperature on GaN growth by plasma assisted molecular beam epitaxy: Part II. Interplay between chemistry and structure of layers," J. Appl. Phys., **91**, 2508 (2002).

[87] G. Namkoong, W. A. Doolittle, A. S. Brown, M. Losurdo, M. M. Giangregorio

and G. Bruno, "The impact of substrate nitridation temperature and buffer design and synthesis on the polarity of GaN epitaxial films," J. Cryst. Growth, **252**, 159 (2003).

[88] G. Namkoong, W. A. Doolittle, S. Kang, H. Sa, A. S. Brown and S. R. Stock, "Low temperature nitridation combined with high temperature buffer annealing for high quality GaN grown by plasma-assisted MBE," MRS Internet J. Nitride Semicond. Res., **5**, 1 (2000).

[89] X. Q. Shen, T. Ide, S. H. Cho, M. Shimizu, S. Hara, H. Okumura, S. Sonoda and S. Shimizu, "Realization of Ga-polarity GaN films in radio-frequency plasma-assisted molecular beam epitaxy," J. Cryst. Growth, **218**, 155 (2000).

[90] D. Huang, P. Visconti, K. M. Jones, M. A. Reshchikov, F. Yun, A. A. Baski, T. King and H. Morkoç, "Dependence of GaN polarity on the parameters of the buffer layer grown by molecular beam epitaxy," Appl. Phys. Lett., **78**, 4145 (2001).

[91] M. Losurdo, P. Capezzuto, G. Bruno, G. Namkoong, W. A. Doolittle and A. S. Brown, "The Chemistry of Sapphire Nitridation in Relation to the GaN Structural Quality: Why Low Temperature 200 C Nitridation?," Phys. Status Solidi A, **188**, 561 (2001).

[92] G. Namkoong, W. A. Doolittle, A. S. Brown, M. Losurdo, P. Capezzuto and G. Bruno, "Role of low-temperature (200°C) nitridation in the growth of GaN by plasma-assisted molecular-beam epitaxy," J. Vac. Sci. Technol. B, **20**, 1221 (2002).

[93] S. D. Burnham, W. A. Doolittle, G. Namkoong and W. Henderson, "Mg doped GaN using a valved, thermally energetic source: enhanced incorporation, and control," J. Cryst. Growth, **279**, 26 (2005).

[94] ASTM Standard F76, "Test Methods for Measuring Resistivity and Hall Coefficient and Determining Hall Mobility in Single-Crystal Semiconductors," ASTM International, West Conshohocken, PA, 2011.

[95] R. R. Lieten, V. Motsnyi, L. Zhang, K. Cheng, M. Leys, S. Degroote, G. Buchowicz, O. Dubon and G. Borghs, "Mg Doping of GaN by Molecular Beam Epitaxy," J. Phys. D: Appl. Phys., **44**, 1345406 (2011).

[96] H. Heinke, V. Kirchner, S. Einfeldt and D. Hommel, "X-ray diffraction analysis of the defect structure in epitaxial GaN," Appl. Phys. Lett., **77**, 2145 (2000).

[97] J. Pereiro, A. Redondo-Cubero, S. Fernandez-Garrido, C. Rivera, A. Navarro, E. Muñoz, E. Calleja and R. Gago, "Mg doping of InGaN layers grown by PA-MBE for the fabrication of Schottky barrier photodiodes," J. Phys. D: Appl. Phys., **43**, 335101 (2010).

[98] M. Lachab, D. H. Youn, R. S. Q. Fareed, T. Wang and S. Sakai, "Characterization of Mg-doped GaN grown by metalorganic chemical vapor deposition," Solid State Electron., **44**, 1669 (2000).

[99] J. Simon and D. Jena, "Effect of growth conditions on the conductivity of Mg doped p-type GaN by Molecular Beam Epitax," Phys. Status Solidi A, **205**, 1074 (2008).

[100] D. K. Schroder, *Semiconductor Material and Device Characterization*, Third Ed. (J. Wiley, New York, 2006), 466-479.

[101] H. Amano, M. Kito, K. Hiramatsu and I. Akasaki, "P-Type Conduction in Mg-Doped GaN Treated with Low-Energy Electron Beam Irradiation (LEEBI)," Jpn. J. Appl. Phys., **28**, L2112 (1989).

[102] S. Nakamura, M. Senoh and T. Mukai, "Highly p-type Mg-doped GaN films grown with GaN buffer layers," Jpn. J. Appl. Phys., **30**, L1708 (1991).

[103] G. Namkoong, W. A. Doolittle and A. S. Brown, "Incorporation of Mg in GaN grown by plasma-assisted molecular beam epitaxy," Appl. Phys. Lett., **77**, 4386 (2000).

[104] S. D. Burnham, G. Namkoong, D. C. Look, B. Clafin and W. A. Doolittle, "Reproducible increased Mg incorporation and large hole concentration in GaN using metal modulated epitaxy," J. Appl. Phys., **104**, 024902 (2008).

[105] B. Gunning, J. Lowder, M. Moseley and W. A. Doolittle, "Negligible carrier freeze-out facilitated by impurity band conduction in highly p-type GaN," Appl. Phys. Lett., **101**, 082106 (2012).

[106] Y. Gong, Y. Gu, I. L. Kuskovsky, G. F. Neumark, J. Li, J. Y. Lin, H. X. Jiang and I. Ferguson, "Non-Equilibrium Acceptor Concentration in GaN:Mg Grown by Metalorganic Chemical Vapor Deposition," Mat. Res. Soc. Symp. Proc., **798**, Y5.16.1 (2004).

[107] W. Wang, W. Liu, M. S. Hao, S. J. Chua and R. Liu, "Temperature-dependent Hall study on p-type GaN epilayers grown by metal-organic chemical vapor deposition," IPAP Conference Ser., **1**, 736 (2000).

[108] P. Kozodoy, H. Xing, S. P. DenBaars, U. K. Mishra, A. Saxler, R. Perrin, S. Elhamri and W. C. Mitchel, "Heavy doping effects in Mg-doped GaN," J. Appl. Phys., **87**, 1832 (2000).

[109] E. Haus, I. P. Smorchkova, B. Heying, P. Fini, C. Poblenz, T. Mates, U. K. Mishra and J. S. Speck, "The role of growth conditions on the p-doping of GaN by plasma-assisted molecular beam epitaxy," J. Cryst. Growth, **246**, 55 (2002).

[110] B. Heying, R. Averbeck, L. F. Chen, E. Haus, H. Riechert and J. S. Speck,

"Control of GaN surface morphologies using plasma-assisted molecular beam epitaxy," J. Appl. Phys., **88**, 1855 (2000).

[111] J. E. Northrup, J. Neugebauer, R. M. Feenstra and A. R. Smith, "Structure of GaN(0001): The laterally contracted Ga bilayer model," Phys. Rev. B, **61**, 9932 (2000).

[112] C. Adelmann, J. Brault, G. Mula and B. Daudin, "Gallium adsorption on (0001) GaN surfaces," Phys. Rev. B, **67**, 165419 (2003).

[113] C. Adelmann, J. Brault, D. Jalabert, P. Gentile, H. Mariette, G. Mula and B. Daudin, "Dynamically stable gallium surface coverages during plasma-assisted molecular-beam epitaxy of (0001) GaN," J. Appl. Phys., **91**, 9638 (2002).

[114] G. Mula, C. Adelmann, S. Moehl, J. Oullier and B. Daudin, "Surfactant effect of gallium during molecular-beam epitaxy of GaN on AlN (0001)," Phys. Rev. B, **64**, 195406 (2001).

[115] C. Adelmann, J. Brault, E. Martinez-Guerrero, G. Mula, H. Mariette, L. S. Dang and B. Daudin, "Molecular-Beam Epitaxy of GaN: A Phase Diagram," Phys. Status Solidi A, **188**, 575 (2001).

[116] S. D. Burnham, W. A. Doolittle, G. Namkoong and W. Henderson, "Mg doped GaN using a valved, thermally energetic source: enhanced incorporation, control and quantitative optimization," Materials Research Society Proceeding, **798**, Y8.11 (2003).

[117] S. D. Burnham, G. Namkoong, K.-K. Lee and W. A. Doolittle, "Reproducible reflection high energy electron diffraction signatures for improvement of AlN using *in situ* growth regime characterization," J. Vac. Sci. Technol. B, **25**, 1009 (2007).

[118] ASTM Standard F76, "Test Methods for Measuring Resistivity and Hall Coefficient and Determining Hall Mobility in Single-Crystal Semiconductors," ASTM International, West Conshohocken, PA, 2011.

[119] A. R. Smith, R. M. Feenstra, D. W. Greve, M.-S. Shin, M. Skowronski, J. Neugebauer and J. E. Northrup, "Determination of wurtzite GaN lattice polarity based on surface reconstruction," Appl. Phys. Lett., **72**, 2114 (1998).

[120] Q. Sun, A. Selloni, T. H. Myers and W. A. Doolittle, "Energetics of Mg incorporation at GaN(0001) and GaN(000-1) surfaces," Phys. Rev. B, **73**, 155337 (2006).

[121] M. E. Zvanut, Y. Uprety, J. Dashdorj, M. Moseley and W. A. Doolittle, "Passivation and activation of Mg acceptors in heavily doped GaN," J. Appl. Phys., **110**, 044508 (2011).

[122] M. A. Khan, J. N. Kuznia, J. M. V. Hove, N. Pan and J. Carter, "Observation of a two-dimensional electron gas in low pressure metalorganic chemical vapor deposited GaN-$Al_xGa_{a-x}N$ Heterojunctions," Appl. Phys. Lett., **60**, 3027 (1992).

[123] J. Guo, G. Li, F. Faria, Y. Cao, Ronghua Wang, J. Verma, X. Gao, S. Guo, E. Beam, A. Ketterson, M. Schuette, P. Saunier, M. Wistey, D. Jena and H. Xing, "MBE-Regrown Ohmics in InAlN HEMTs With a Regrowth Interface Resistance of 0.05 Ω · mm," IEEE Electr. Device L., **33**, 525 (2012).

[124] M. S. Shur, A. D. Bykhovski, R. Gaska, J. W. Yang, G. Simin and M. A. Khan, "Accumulation hole layer in p-GaN/AlGaN heterostructures," Appl. Phys. Lett., **76**, 3061 (2000).

[125] Q. Wei, Z. Wu, K. Sun, F. A. Ponce, J. Hertkorn and F. Scholz, "Evidence of Two-Dimensional Hole Gas in p-Type AlGaN/AlN/GaN Heterostructures," Appl. Phys. Express, **2**, 121001 (2009).

[126] A. Nakajima, Y. Sumida, M. H. Dhyani, H. Kawai and E. M. S. Narayanan, "High Density Two-Dimensional Hole Gas Induced by Negative Polarization at GaN/AlGaN Heterointerface," Appl. Phys. Express, **3**, 121004 (2010).

[127] G. Li, R. Wang, B. Song, J. Verma, Y. Cao, S. Ganguly, A. Verma, J. Guo, H. G. Xing and D. Jena, "Polarization-Induced GaN-on-Insulator E/D Mode p-Channel Heterostructure FETs," IEEE Electr. Device L., **34**, 852 (2013).

[128] J. Verma, S. M. Islam, V. Protasenko, P. K. Kandaswamy, H. G. Xing and D. Jena, "Tunnel-injection quantum dot deep-ultraviolet light-emitting diodes with polarization-induced doping in III-nitride heterostructures," Appl. Phys. Lett., **104**, 021105 (2014).

[129] S. Acar, S. B. Lisesivdin, M. Kasap, S. Özçelik and E. Özbay, "Determination of two-dimensional electron and hole gas carriers in AlGaN/GaN/AlN heterostructures grown by Metal Organic Chemical Vapor Deposition," Thin Solid Films, **516**, 2041 (2008).

[130] J. Hertkorn, S. B. Thapa, T. Wunderer, F. Scholz, Z. H. Wu, Q. Y. Wei, F. A. Ponce, M. A. Moram, C. J. Humphreys, C. Vierheilig and U. T. Schwarz, "Highly conductive modulation doped composition graded p-AlGaN/(AlN)/GaN multiheterostructures grown by metalorganic vapor phase epitaxy," J. Appl. Phys., **106**, 013720 (2009).

[131] J. Simon, V. Protasenko, C. Lian, H. Xing and D. Jena, "Polarization-Induced Hole Doping in Wide–Band-Gap Uniaxial Semiconductor Heterostructures," Science, **327**, 60 (2010).

[132] T. Zimmermann, M. Neuburger, M. Kunze, I. Daumiller, A. Denisenko, A. Dadgar, A. Krost and E. Kohn, "P-Channel InGaN-HFET Structure Based on Polarization Doping," IEEE Electr. Device L., **25**, 450 (2004).

[133] S. Hackenbuchner, J. A. Majewski, G. Zandler and P. Vogl, "Polarization induced 2D hole gas in GaN/AlGaN heterostructures," J. Cryst. Growth, **230**, 607 (2001).

[134] P. Kozodoy, Y. P. Smorchkova, M. Hansen, H. Xing, S. P. DenBaars, U. K. Mishra, A. W. Saxler, R. Perrin and W. C. Mitchel, "Polarization-enhanced Mg doping of AlGaN/GaN superlattices," Appl. Phys. Lett., **75**, 2444 (1999).

[135] O. Ambacher, J. Smart, J. R. Shealy, N. G. Weimann, K. Chu, M. Murphy, W. J. Schaff, L. F. Eastman, R. Dimitrov, L. Wittmer, M. Stutzmann, W. Rieger and J. Hilsenbeck, "Two-dimensional electron gases induced by spontaneous and piezoelectric polarization charges in N- and Ga-face AlGaN/GaN heterostructures," J. Appl. Phys., **85**, 3222 (1999).

[136] C. Kim, I. K. Robinson, J. Myoung, K. Shim, M.-C. Yoo and K. Kim, "Critical thickness of GaN thin films on sapphire (0001)," Appl. Phys. Lett., **69**, 2358 (1996).

[137] A. D. Bykhovski, B. L. Gelmont and M. S. Shur, "Elastic strain relaxation and piezoeffect in GaN-AlN, GaN-AlGaN and GaN-InGaN superlattices," J. Appl. Phys., **81**, 6332 (1997).

[138] H. Yu, E. Ulker and E. Ozbay, "MOCVD growth and electrical studies of p-type AlGaN with Al fraction 0.35," J. Cryst. Growth, **289**, 419 (2006).

[139] T. Tanaka, A. Watanabe, H. Amano, Y. Kobayashi, I. Akasaki, S. Yamazaki and M. Koike, "ptype conduction in Mgdoped GaN and $Al_{0.08}Ga_{0.92}N$ grown by metalorganic vapor phase epitaxy," Appl. Phys. Lett., **65**, 593 (1994).

[140] M. L. Nakarmi, K. H. Kim, J. Li, J. Y. Lin and H. X. Jiang, "Enhanced p-type conduction in GaN and AlGaN by Mg-d-doping," Appl. Phys. Lett., **82**, 3041 (2003).

[141] V. Kirchner, H. Heinke, U. Birkle, S. Einfeldt, D. Hommel, H. Selke and P. L. Ryder, "Ion-induced crystal damage during plasma-assisted MBE growth of GaN layers," Phys. Rev. B, **58**, 15749 (1998).

[142] M. E. Lin, B. Sverdlov, G. L. Zhou and H. Morkoç, "A comparative study of GaN epilayers grown on sapphire and SiC substrates by plasma-assisted molecular-beam epitaxy," Appl. Phys. Lett., **62**, 3479 (1993).

[143] W. C. Hughes, W. H. R. Jr., M. A. L. Johnson, S. Fujita, J. W. C. Jr., J. F. Schetzina, J. Ren and J. A. Edmond, "Molecular beam epitaxy growth and properties of GaN films on GaN/SiC substrates," J. Vac. Sci. Technol. B, **13**, 1571 (1995).

[144] T. H. Myers, M. R. Millecchia, A. J. Ptak, K. S. Ziemer and C. D. Stinespring, "Influence of active nitrogen species on high temperature limitations for (0001_) GaN growth by rf plasma-assisted molecular beam epitaxy," J. Vac. Sci. Technol.

B, **17**, 1654 (1999).

[145] B. M. McSkimming, F. Wu, T. Huault, C. Chaix and J. S. Speck, "Plasma assisted molecular beam epitaxy of GaN with growth rates >2.6 um/h," J. Cryst. Growth, **386**, 168 (2013).

[146] E. J. Tarsa, B. Heying, X. H. Wu, P. Fini, S. P. DenBaars and J. S. Speck, "Homoepitaxial growth of GaN under Ga-stable and N-stable conditions by plasma-assisted molecular beam epitaxy," J. Appl. Phys., **82**, 5472 (1997).

[147] J.-I. Chyi, C.-M. Lee, C.-C. Chuo, X. A. Cao, G. T. Dang, A. P. Zhang, F. Ren, S. J. Pearton, S. N. G. Chu and R. G. Wilson, "Temperature dependence of GaN high breakdown voltage diode rectifiers," Solid State Electron., **44**, 613 (2000).

[148] A. R. Boyd, S. Degroote, M. Leys, F. Schulte, O. Rockenfeller, M. Luenenbuerger, M. Germain, J. Kaeppeler and M. Heuken, "Growth of GaN/AlGaN on 200 mm diameter silicon (111) wafers by MOCVD," Phys. Status Solidi C, **52**, S1045 (2009).

[149] S. Nakamura, Y. Harada and M. Seno, "Novel metalorganic chemical vapor deposition system for GaN growth," Appl. Phys. Lett., **58**, 2021 (1991).

[150] S. Heikman, S. Keller, S. P. DenBaars and U. K. Mishra, "Growth of Fe doped semi-insulating GaN by metalorganic chemical vapor deposition," Appl. Phys. Lett., **81**, 439 (2002).

[151] R. A. Oliver, M. J. Kappers, C. J. Humphreys and G. A. D. Briggs, "Growth modes in heteroepitaxy of InGaN on GaN," J. Appl. Phys., **97**, 013707 (2005).

[152] M. E. Aumer, S. F. LeBoeuf, F. G. McIntosh and S. M. Bedair, "High optical quality AlInGaN by metalorganic chemical vapor deposition," Appl. Phys. Lett., **75**, 3315 (1999).

[153] M. Moseley, B. Gunning, J. Lowder, W. A. Doolittle and G. Namkoong, "Structural and electrical characterization of InN, InGaN, and p-InGaN grown by metal-modulated epitaxy," J. Vac. Sci. Technol. B, **31**, 01C104-1 (2013).

[154] M. Moseley, J. Lowder, D. Billingsley and W. A. Doolittle, "Control of surface adatom kinetics for the growth of high-indium content InGaN throughout the miscibility gap," Appl. Phys. Lett., **97**, 191902 (2010).

[155] B. Heying, E. J. Tarsa, C. R. Elsass, P. Fini, S. P. DenBaars and J. S. Speck, "Dislocation mediated surface morphology of GaN," J. Appl. Phys., **85**, 6470 (1999).

[156] E. Iliopoulos, A. Adikimenakis, E. Dimakis, K. Tsagaraki, G. Konstantinidis and A. Georgakilas, "Active nitrogen species dependence on radiofrequency plasma source operating parameters and their role in GaN growth," J. Cryst. Growth, **278**,

426 (2005).

[157] M. A. Wistey, S. R. Bank, H. B. Yuen, J. S. H. Jr., M. M. Oye and A. L. H. Jr., "Using beam flux monitor as Langmuir probe for plasma-assisted molecular beam epitaxy," J. Vac. Sci. Technol. A, **23**, 460 (2005).

[158] A. V. Blant, O. H. Hughes, T. S. Cheng, S. V. Novikov and C. T. Foxon, "Nitrogen species from radio frequency plasma sources used for molecular beam epitaxy growth of GaN," Plasma Sources Sci. Technol., **9**, 12 (2000).

[159] J. Osaka, M. S. Kumar, H. Toyoda, T. Ishijima, H. Sugai and T. Mizutani, "Role of atomic nitrogen during GaN growth by plasma-assisted molecular beam epitaxy revealed by appearance mass spectrometry," Appl. Phys. Lett., **90**, 172114 (2011).

[160] L. T. Romano, C. G. V. d. Walle, J. W. A. III, W. Gotz and R. S. Kern, "Effect of Si doping on strain, cracking, and microstructure in GaN thin films grown by metalorganic chemical vapor deposition," J. Appl. Phys., **87**, 7745 (2000).

[161] T. Sugiyama, D. Iida, T. Yasuda, M. Iwaya, T. Takeuchi, S. Kamiyama and I. Akasaki, "Extremely Low-Resistivity and High-Carrier-Concentration Si-Doped $Al_{0.05}Ga_{0.95}N$," Appl. Phys. Express, **6**, 121002 (2013).

[162] F. A. Faria, J. Guo, P. Zhao, G. Li, P. K. Kandaswamy, M. Wistey, H. G. Xing and D. Jena, "Ultra-low resistance ohmic contacts to GaN with high Si doping concentrations grown by molecular beam epitaxy," Appl. Phys. Lett., **101**, 032109 (2012).

[163] P. R. Hageman, W. J. Schaff, J. Janinski and Z. Liliental-Weber, "n-type doping of wurtzite GaN with germanium grown with plasma-assisted molecular beam epitaxy," J. Cryst. Growth, **267**, 123 (2004).

[164] I. Gherasoiu, K. M. Yu, L. A. Reichertz and W. Walukiewicz, "InGaN doping for high carrier concentration in plasma-assisted molecular beam epitaxy," Phys. Status Solidi C, **11**, 381 (2014).

[165] S. G. Davis, D. F. Anthrop and A. W. Searcy, "Vapor Pressure of Silicon and the Dissociation Pressure of Silicon Carbide," J. Chem. Phys., **34**, 659 (1961).

[166] A. W. Searcy, "The vapor pressure of germanium," J. Am. Chem. Soc., **74**, 4789 (1952).

[167] W. Gotz, R. S. Kern, C. H. Chen, H. Liu, D. A. Steigerwald and R. M. Fletcher, "Hall-effect characterization of III–V nitride semiconductors for high efficiency light emitting diodes," Mater. Sci. Eng. B, **59**, 211 (1999).

[168] S. Fritze, A. Dadgar, H. Witte, M. Bugler, A. Rohrbeck, J. Blasing, A. Hoffmann and A. Krost, "High Si and Ge n-type doping of GaN doping - Limits and impact

on stress," Appl. Phys. Lett., **100**, 122104 (2012).

[169] B. Heying, X. H. Wu, S. Keller, Y. Li, D. Kapolnek, B. P. Keller, S. P. DenBaars and J. S. Speck, "Role of threading dislocation structure on the x-ray diffraction peak widths in epitaxial GaN films," Appl. Phys. Lett., **68**, 643 (1995).

[170] R. Chierchia, T. Böttcher, H. Heinke, S. Einfeldt, S. Figge and D. Hommel, "Microstructure of heteroepitaxial GaN revealed by x-ray diffraction," J. Appl. Phys., **93**, 8918 (2003).

[171] H. M. Ng, D. Doppalapudi, T. D. Moustakas, N. G. Weimann and L. F. Eastman, "The role of dislocation scattering in n-type GaN films," Appl. Phys. Lett., **73**, 821 (1998).

[172] D. C. Look and J. R. Sizelove, "Dislocation Scattering in GaN," Phys. Rev. Lett., **82**, 1237 (1999).

[173] N. G. Weimann, L. F. Eastman, D. Doppalapudi, H. M. Ng and T. D. Moustakas, "Scattering of electrons at threading dislocations in GaN," J. Appl. Phys., **83**, 3656 (1997).

[174] "Best Research-Cell Efficiencies," 2015, National Renewable Energy Lab, Accessed 26 Oct. 2015

[175] W. Kern and D. A. Puotinen, "Cleaning Solutions Based on Hydrogen Peroxide for Use in Silicon Semiconductor Technology," RCA Rev., **31**, 187 (1970).

[176] G. Koblmüller, S. Fernández-Garrido, E. Calleja and J. S. Speck, "In situ investigation of growth modes during plasma-assisted molecular beam epitaxy of (0001) GaN," Appl. Phys. Lett., **91**, 161904 (2007).

[177] C. S. Gallinat, G. Koblmuller, J. S. Brown and J. S. Speck, "A growth diagram for plasma-assisted molecular beam epitaxy of In-face InN," J. Appl. Phys., **102**, 064907 (2007).

[178] J. Hackley and C. Richardson, "The Epitaxial Growth of Aluminum on Si(111) and C-plane Sapphire", 29th North American Molecular Beam Epitaxy Conference, Atlanta, GA, October 14-17, 2012.

[179] W. A. Doolittle, Ph.D. thesis, Georgia Institute of Technology, 1996.

[180] Y.-Y. Wong, E. Y. Chang, Y.-H. Wu, M. K. Hudait, T.-H. Yang, J.-R. Chang, J.-T. Ku, W.-C. Chou, C.-Y. Chen, J.-S. Maa and Y.-C. Lin, "Dislocation reduction in GaN film using Ga-lean GaN buffer layer and migration enhanced epitaxy," Thin Solid FIlms, **519**, 6208 (2011).

[181] J. L. Murray and A. J. McAlister, "The Al-Si (Aluminum-Silicon) system," Bulletin of Alloy Phase Diagrams, **5**, 78 (1984).

[182] Y. Cordier, J.-C. Moreno, N. Baron, E. Frayssinet, J.-M. Chauveau, M. Nemoz, S. Chenot, B. Damilano and F. Semond, "Growth of GaN based structures on Si(1 1 0) by molecular beam epitaxy," J. Cryst. Growth, **312**, 2683 (2010).

[183] A. L. Louarn, S.Vezian, F.Semond and J.Massies, "AlN buffer layer growth for GaN epitaxy on (111) Si: Al or N first?," J. Cryst. Growth, **311**, 3278 (2009).

[184] F. Semond, B. Damilano, S. Vezian, N. Grandjean, M. Leroux and J. Massies, "GaN grown on Si(111) substrate: From two-dimensional growth to quantum well assessment," Appl. Phys. Lett., **75**, 82 (1999).

[185] Y. Lu, X. Liu, D.-C. Lu, H. Yuan, Z. Chen, T. Fan, Y. Li, P. Han, X. Wang, D. Wang and Z. Wang, "Investigation of GaN layer grown on Si(1 1 1) substrate using an ultrathin AlN wetting layer," J. Cryst. Growth, **236**, 77 (2002).

[186] J. Ma, X. Zhu, K. M. Wong, X. Zou and K. M. Lau, "Improved GaN-based LED grown on silicon (111) substrates using stress/dislocation-engineered interlayers," J. Cryst. Growth, **370**, 265 (2013).

[187] Z. Xu, L. Zhang, H. He, J. Wang and M. Xie, "Growth of GaN on Si(111): Surfaces and crystallinity of the epifilms and the transport behavior of GaN/Si heterojunctions," J. Appl. Phys., **110**, 093514 (2011).

[188] M. Kumar, B. Roul, T. N. Bhat, M. K. Rajpalke, P. Misra, L. M. Kukreja, N. Sinha, A. T. Kalghatgi and S. B. Krupanidhi, "Improved growth of GaN layers on ultra thin silicon nitride/Si (1 1 1) by RF-MBE," Mater. Res. Bull., **45**, 1581 (2010).

[189] M. Irie, N.Koide, Y.Honda, M.Yamaguchi and N.Sawaki, "MOVPE growth and properties of GaN on (111) Si using an AlInN intermediate layer," J. Cryst. Growth, **311**, 2891 (2009).

[190] J. W. Ager, L. A. Reichertz, K. M. YU, W. J. Schaff, T. L. Williamson, M. A. Hoffbauer, N. M. Haegel and W. Walukiewicz, "InGaN/Si heterojunction tandem solar cells " IEEE Phot. Spec. Conf., 1 (2008).

[191] A. M. Fischer, Y. O. Wei, F. A. Ponce, M. Moseley, B. Gunning and W. A. Doolittle, "Highly luminescent, high-indium-content InGaN film with uniform composition and full misfit-strain relaxation," Appl. Phys. Lett., **103**, 131101 (2013).

[192] J. Walling, O. Peterson, H. Jenssen, R. Morris and E. O'Dell, "Tunable alexandrite lasers," IEEE J. Quantum Elect., **16**, (1980).

[193] I. Yorulmaz, E. Beyatli, A. Kurt, A. Sennaroglu and U. Demirbas, "Efficient and low-threshold Alexandrite laser pumped by a single-mode diode," Opt. Mater. Express, **4**, 776 (2014).

[194] R. Scheps, B. M. Gately, J. F. Myers, J. S. Krasinski and D. F. Heller, "Alexandrite laser pumped by semiconductor lasers," Appl. Phys. Lett., **56**, (1990).

[195] S. K. Davidsson, J. F. Fälth, X. Y. Liu and T. G. Anderson, "Effect of AlN nucleation layer on the structural properties of bulk GaN grown on sapphire by molecular-beam epitaxy," J. Appl. Phys., **98**, 016109-1 (2005).

[196] J. F. Fälth, S. K. Davidsson, X. Y. Liu and T. G. Andersson, "Influence of Al/N flux ratio during nucleation layer growth on the structural properties of AlN grown on sapphire by molecular beam epitaxy," Appl. Phys. Lett., **87**, (2005).

VITA

Brendan Gunning was born in Baltimore, Maryland where he attended the Gilman School. He then attended the Georgia Institute of Technology where he received a Bachelor's degree in Electrical Engineering in 2010 and a Master's degree in Electrical and Computer Engineering in 2012. He plans to receive his Ph.D. in December of 2015 under the supervision of Prof. W. Alan Doolittle. His research interests include the growth, characterization, and fabrication of III-Nitride semiconductor materials and devices.

First-Author and Co-Author Publications

B. Gunning, E. Clinton, J. Merola, W. A. Doolittle, and R. Bresnahan, "Control of Ion Content and Nitrogen Species Using a Mixed Chemistry Plasma for GaN Grown at Extremely High Growth Rates >9μm/hour by Plasma-Assisted Molecular Beam Epitaxy," J. Appl. Phys., 118, 155302 (2015).

B. Gunning, C. Fabien, J. Merola, E. Clinton, W. A. Doolittle, S. Wang, A. Fischer, and F. Ponce, "Comprehensive study of the electronic and optical behavior of highly degenerate p-type Mg-doped GaN and AlGaN," J. Appl. Phys., 117, 045710 (2015).

B. Gunning, J. Lowder, M. Moseley, and W. A. Doolittle, "Negligible carrier freeze-out facilitated by impurity-band conduction in highly p-type GaN," Appl. Phys. Lett, 101, 082106 (2012).

C. Fabien, **B. Gunning**, W. A. Doolittle, A. Fischer, Y. Wei, H. Xie, and F. Ponce, "Low-temperature growth of InGaN films over the entire composition range by MBE," J. Cryst. Growth, 425, 115 (2015).

J. Greenlee, J. Shank, M. B. Tellekamp, **B. Gunning**, C. Fabien, and W. A. Doolittle, "Liquid Phase Electro-Epitaxy of Memristive LiNbO2 Crystals," Cryst. Growth Des., 4, 2218 (2014).

C. Fabien, M. Moseley, **B. Gunning**, W. A. Doolittle, A. M. Fischer, Y. O. Wei, and F. A. Ponce, "Simulations, practical limitations, and novel growth technology for InGaN-based solar cells," IEEE J. Photovoltaics, 4, 601 (2013).

A. M. Fischer, Y. O. Wei, F. A. Ponce, M. Moseley, **B. Gunning** and W. A. Doolittle, "Highly luminescent, high-indium-content InGaN film with uniform composition and full misfit-strain relaxation," Appl. Phys. Lett., 103, 131101 (2013).

M. Moseley, **B. Gunning**, J. Lowder, W. A. Doolittle and G. Namkoong, "Structural and electrical characterization of InN, InGaN, and p-InGaN grown by metal-modulated epitaxy," J. Vac. Sci. Technol. B, 31, 01C104-1 (2013).

M. Moseley, **B. Gunning**, J. Greenlee, J. Lowder, G. Namkoong, and W. A. Doolittle, "Observation and Control of the Surface Kinetics of InGaN for the Elimination of Phase Separation," J. Appl. Phys., 112, 014909 (2012).

Conference Presentations and Posters

B. Gunning, E. Clinton, J. Merola, C. Fabien, and W. A. Doolittle, "Dramatically Increased Growth Rates Exceeding 9 μm/Hour for GaN Grown by Plasma-Assisted MBE," 57th Electronic Materials Conference, Columbus, Ohio, USA, June 2015.

C. Fabien, **B. Gunning**, J. Merola, E. Clinton, and W. A. Doolittle, "Large-Area III-Nitride Double-Heterojunction Solar Cells with Record-High In-content InGaN Absorbing Layers," 42nd Photovoltaic Specialists Conference, New Orleans, Louisiana, USA, June 2015.

B. Gunning, C. Fabien, J. Merola, E. Clinton, W. A. Doolittle, A. Fischer, S. Wang, Y. Wei, and F. Ponce, "Electronic and Optical Behavior of Highly p-type GaN and AlGaN, and High Growth Rate GaN by MBE," Workshop on Compound Semiconductor Materials and Devices, Isle of Palms, South Carolina, USA, February 2015. ***Most Valuable Contribution Award.**

B. Gunning, C. Fabien, J. Merola, E. Clinton, and W. A. Doolittle, "III-Nitride Optoelectronic Devices Using Highly Mg-doped p-type Layers Grown by Metal-Modulated Epitaxy," 18th International Conference on Molecular Beam Epitaxy, Flagstaff, Arizona, USA, September 2014.

B. Gunning, C. Fabien, J. Merola, E. Clinton, W. A. Doolittle, A. Fischer, S. Wang, Y. Wei, and F. Ponce, "Highly Conductive P-type III-Nitrides Using Both Bulk and 2-Dimensional Heavily Mg-doped Layers," 18th International Conference on Molecular Beam Epitaxy, Flagstaff, Arizona, USA, September 2014.

C. Fabien, **B. Gunning**, M. Moseley, W. A. Doolittle, A. Fischer, Y. Wei, and F. Ponce, "Comparison of N-rich and MME-grown InGaN Throughout the Miscibility Gap," 18th International Conference on Molecular Beam Epitaxy, Flagstaff, Arizona, USA, September 2014.

W. A. Doolittle, **B. Gunning**, C. Fabien, A. Fischer, S. Wang, Y. Wei, and F. Ponce, "Extremely high hole concentrations in III-Nitrides," International Workshop on Nitride Semiconductors, Wroclaw, Poland, August 2014.

B. Gunning, C. Fabien, J. Merola, E. Clinton, and W. A. Doolittle, "Highly Conductive P-Type GaN and AIGaN Using Both Bulk and 2-Dimensional Heavily Mg-Doped Layers," 5th International Symposium on Growth of III- Nitrides, Atlanta, Georgia, USA, May 2014.

C. Fabien, **B. Gunning**, M. Moseley, W. A. Doolittle, A. Fischer, Y. Wei, and F. Ponce, "Prospects of InGaN-Based Solar Cells by Metal-Modulated Epitaxy," 5th International Symposium on Growth of III-Nitrides, Atlanta, Georgia, USA, May 2014.

B. Gunning, C. Fabien, and W. A. Doolittle, "Breaching the perceived upper bounds of p-type doping in GaN and InGaN," Workshop on Compound Semiconductor Materials and Devices, San Antonio, Texas, USA, February 2014.

W. A. Doolittle, **B. Gunning**, C. Fabien, A. Fischer, Y. Wei, and F. Ponce, "New advances in III-Nitride epitaxy," Workshop on Compound Semiconductor Materials and Devices, San Antonio, Texas, USA, February 2014.

W. A. Doolittle, **B. Gunning**, C. Fabien, M. Moseley, "MBE Growth Methodologies for Overcoming the Perceived Limitations of Phase Separation and P-type Doping in InGaN," 30th American Molecular Beam Epitaxy Conference, Banff, Alberta, Canada, October 2013.

B. Gunning, J. Lowder, M. Moseley, C. Fabien, G. Namkoong, W. A. Doolittle, "Optimization of Growth and Electrical Transport Properties of Highly p-type GaN and InGaN," 10th International Conference on Nitride Semiconductors, Washington, D.C., USA, August 2013.

A. Fischer, Y. O. Wei, F. A. Ponce, M. Moseley, **B. Gunning**, W. A. Doolittle, "High-Indium-Content InGaN Layers with Uniform Composition, Full Misfit-Strain Relaxation, and High Light- Emission Efficiency," 10th International Conference on Nitride Semiconductors, Washington, D.C., USA, August 2013.

C. Fabien, **B. Gunning**, M. Moseley, W. A. Doolittle, A. M. Fischer, Y. Wei, F. A. Ponce, "Advances in Nitride Growth Technology for InGaN-Based Solar Cells," 10th International Conference on Nitride Semiconductors, Washington, D.C., USA, August 2013.

C. Fabien, **B. Gunning**, M. Moseley, W. A. Doolittle, A. Fischer, Y. Wei, and F. Ponce, "Simulations, practical limitations and novel growth technology for InGaN-based solar cells," 39th IEEE Photovoltaic Specialists Conference, Tampa Bay, Florida, USA, June 2013.

B. Gunning, M. Moseley, and W. A. Doolittle, "Impurity Band Conduction in Highly p-type GaN and InGaN," 29th North American Molecular Beam Epitaxy Conference, Atlanta, Georgia, USA, October 2012.

M. Moseley, **B. Gunning**, J. Greenlee, J. Lowder, W. A. Doolittle, "Observation and Control of the Surface Kinetics of InGaN for the Elimination of Phase Separation," 29th North American Molecular Beam Epitaxy Conference, Atlanta, Georgia, USA, October 2012.

C. Fabien, M. Moseley, **B. Gunning**, W. A. Doolittle, "Characterization of MBE Grown, Threading Dislocation Free, High-Indium InGaN without Phase Separation," 29th North American Molecular Beam Epitaxy Conference, Atlanta, Georgia, USA, October 2012.

M. Moseley, J. Lowder, **B. Gunning**, M. E. Zvanut, J. Dashdorj, W. A. Doolittle, "Characterization of Mg Acceptors in GaN:Mg Grown by Metal Modulated Epitaxy and MOCVD," American Vacuum Society 58th International Symposium and Exhibition, Nashville, Tennessee, USA, October 2011.

M. Moseley, **B. Gunning**, J. Lowder, G. Namkoong, W. A. Doolittle, "Elimination of Indium Surface Segregation in InGaN Grown Throughout the Miscibility Gap," American Vacuum Society 58th International Symposium and Exhibition, Nashville, Tennessee, USA, October 2011.

B. Gunning, M. Moseley, J. Lowder, W. A. Doolittle, "Elimination of Indium Surface Segregation in InGaN Grown Throughout the Miscibility Gap," 9th International Conference on Nitride Semiconductors, Glasgow, Scotland, UK, July 2011.

M. Moseley, **B. Gunning**, J. Lowder, G. Namkoong, W. A. Doolittle, "InN and n and p-type InGaN Grown by Metal-Modulated Epitaxy," 9th International Conference on Nitride Semiconductors, Glasgow, Scotland, UK, July 2011.

B. Gunning, M. Moseley, J. Lowder, W. A. Doolittle, J. Wierer, S. Lee, D. Koleske, Q. Li, "InGaN/GaN p-i-n Solar Cells Grown by Metal-Modulated Epitaxy," 9th International Conference on Nitride Semiconductors, Glasgow, Scotland, UK, July 2011.

J. Lowder, M. Moseley, **B. Gunning**, W. A. Doolittle, M. E. Zvanut, J. Dashdorj, "Characterization of Mg Acceptors in GaN:Mg grown by Metal Modulated Epitaxy and MOCVD," 9th International Conference on Nitride Semiconductors, Glasgow, Scotland, UK, July 2011.

M. Moseley, J. Lowder, **B. Gunning**, D. Billingsley, G. Namkoong, W. A. Doolittle, "Observation and Elimination of Indium Surface Segregation," Electronic Materials Conference 2011, Santa Barbara, CA, USA, June 2011.

M. Moseley, J. Lowder, **B. Gunning**, E. Trybus, D. Billingsley, W. Henderson, G.

Namkoong, W. A. Doolittle, “Deeply Degenerate p-type Doping in III-Nitrides: Critical Milestones Achieved for High Power Electronics,” Air Force Office of Scientific Research Joint Electronics Program Review, Arlington, VA, USA, May 2011.